UNIVERSIDADE TÉCNICA DE LISBOA

INSTITUTO SUPERIOR TÉCNICO

Carbon dispersions in nanostructured metals

Daniela da Silva Nunes Gomes

Supervisor: Doctor Patrícia Almeida de Carvalho
Co-Supervisor: Doctor José Brito Correia

Thesis approved in public session to obtain the PhD Degree in Materials Science and Engineering

Jury final classification

Jury

Chairperson: Chairman of the IST Scientific Board

Member of the committee:
Doctor Rui Mário Correia da Silva Vilar, Cathedratic Professor, Instituto Superior Técnico
Doctor Bruno Miguel Quelhas de Sacadura Cabral Trindade, Associate Professor, Faculdade de Ciências e Tecnologia da Universidade de Coimbra
Doctor José Brito Correia, Principal Investigator, Laboratório Nacional de Energia e Geologia
Doctor Horácio Fernandes, Auxiliary Professor, Instituto Superior Técnico
Doctor Alberto Eduardo Morão Cabral Ferro, Auxiliary Professor, Instituto Superior Técnico
Doctor Patrícia Maria Cristovam Cipriano Almeida de Carvalho, Auxiliary Professor, Instituto Superior Técnico

FUNDING INSTUTITIONS: Fundação para a Ciência e Tecnologia

2012

UNIVERSIDADE TÉCNICA DE LISBOA

INSTITUTO SUPERIOR TÉCNICO

Carbon dispersions in nanostructured metals

Daniela da Silva Nunes Gomes

Supervisor: Doctor Patrícia Almeida de Carvalho
Co-Supervisor: Doctor José Brito Correia

Thesis approved in public session to obtain the PhD Degree in Materials Science and Engineering

Jury final classification

Jury

Chairperson: Chairman of the IST Scientific Board

Member of the committee:
Doctor Rui Mário Correia da Silva Vilar, Cathedratic Professor, Instituto Superior Técnico
Doctor Bruno Miguel Quelhas de Sacadura Cabral Trindade, Associate Professor, Faculdade de Ciências e Tecnologia da Universidade de Coimbra
Doctor José Brito Correia, Principal Investigator, Laboratório Nacional de Energia e Geologia
Doctor Horácio Fernandes, Auxiliary Professor, Instituto Superior Técnico
Doctor Alberto Eduardo Morão Cabral Ferro, Auxiliary Professor, Instituto Superior Técnico
Doctor Patrícia Maria Cristovam Cipriano Almeida de Carvalho, Auxiliary Professor, Instituto Superior Técnico

FUNDING INSTUTITIONS: Fundação para a Ciência e Tecnologia

2012

Resumo

Nanodiamante ou grafite sintética foram dispersados em cobre, níquel ou tungsténio por moagem de bolas com o intuito de produzir compósitos de metal-carbono. A seleção de condições de moagem adequadas proporcionou uma dispersão homogénea das fases de carbono e a obtenção de matrizes nanoestruturadas, além de minimizar a contaminação proveniente dos meios de moagem bem como a formação de carbonetos. As mudanças estruturais provocadas pela moagem e tratamentos térmicos foram escrutinadas por difração de raio-X, microscopia electrónica, espectroscopia de Raman e medidas de microdureza. A análise pormenorizada das fases de carbono foi possível após dissolução química das matrizes metálicas: o nanodiamante preservou a sua estrutura cristalina durante a moagem, enquanto a grafite demonstrou tendência para amorfizar. A estabilidade dos compósitos nanoestruturados foi avaliada por meio de tratamentos térmicos. A transformação de nanodiamante em estruturas de carbono em forma de cebola durante os tratamentos térmicos foi catalizada pela moagem prévia na presença de níquel, tendo-se demonstrado que ocorre *in situ* resultanto em compósitos de metal-nanocebolas. Mecanismos de endurecimento e estabilização térmica foram discutidos. Nanocompósitos densos de cobre-nanodiamante foram produzidos por extrusão a quente e por sinterização induzida por plasma.

Palavras chave: cobre, níquel, tungstênio, nanodiamante, grafite, transformação de fase, afinidade química, moagem de bolas, tratamento térmicos, efeitos de endurecimento.

Abstract

The present work reports the conditions for dispersing nano-sized carbon particles in metallic matrices by ball milling. Nanodiamond or synthetic graphite has been milled with copper, nickel or tungsten to produce nanostructured metal-carbon composites. Close monitoring of the milling conditions enabled to homogeneously disperse the carbon phases and obtain nanostructured matrices, as well as to minimize milling media contamination and carbide formation. The structural changes induced by milling and annealing have been scrutinized by X-ray diffraction, electron microscopy, Raman spectroscopy and microhardness measurements. The metallic matrices have been chemically dissolved to allow for a detailed analysis of the carbon phases: nanodiamond preserved its crystalline structure during milling while graphite tended to amorphize. Heat treatments have been performed to evaluate the nanocomposites thermal stability. Transformation of nanodiamond into onion-like carbon during annealing is catalyzed by previous milling in the presence of Ni and has been demonstrated to occur *in situ* resulting in metal-onion-like carbon composites. Strengthening and thermal stabilization mechanisms are discussed. Fully dense copper-nanodiamond nanocomposites have been produced by hot extrusion and spark plasma sintering.

Key-words: copper, nickel, tungsten, nanodiamond, graphite, phase transformation, chemical affinity, ball milling, heat treatments, strengthening effects.

Acknowledgments

First and foremost, I would like to thank Professor Patrícia Almeida Carvalho for the form that she guided my work, and for her friendship. Her support and suggestions always have been passed in the best way and had contributed for my personal development. I am grateful for the freedom that she gave to me on my work, her confidence on my skills, her interest, but above of all her incentive.

I am grateful to my co-supervisor Doctor José Brito Correia for his ideas and explanations coming always in the right time, for his guidance in the materials preparation, for his availability when I needed help, and for all the support during these four years.

I appreciate the help and support of Isabel Nogueira, Rodrigo Mateus, Vanessa Livramento and Filipe Neves. I wish to express my gratitude to Professor Marcia Vilarigues for the Raman measurements. I am also thankful to Professor Umesh Vinaica and Professor Manuel Francisco Pereira for DTA and XRD measurements, respectively.

I am deeply thankful to Instituto de Plasmas e Fusão Nuclear, especially to Professors Carlos Varandas, Horácio Fernandes and Carlos Silva for making me part of the institute, for all the conference financial supports and research supplies.

I thank to Fundação para a Ciência e a Tecnologia for financial support under the SFRH/BD/41932/2007 fellowship.

Finally a special thanks to my family, my parents that are the most important people in my life, and that thought me the base of everything, my sister that is my friend of life, my aunt Marluce that always cheers me up, my husband Pedro that has the biggest patience with me and waits for me when I am late without complaining, to my parents-in-law for all the help and the rest of family that is far, but close in mind.

Daniela.

Page

Contents

Chapter 1 – Introduction

1.1 Motivation 3

1.2 State of the art 4

1.2.1 Carbon phases 4

1.2.2 Metallic matrices 6

1.2.3 Strengthening and thermal stabilization mechanisms 9

1.2.4 Contamination by milling media 17

1.2.5 Consolidation 17

1.3 References 18

Chapter 2 – Experimental

2.1 Methods and working principals 26

2.1.1 Ball milling 26

2.1.1.1 Ball milling working principles and mechanisms 26

2.1.1.2 Ball milling processing variables 29

2.1.2 Consolidation 33

2.1.2.1 Spark Plasma Sintering 33

2.1.2.2 Hot extrusion 35

2.1.3 Materials characterization 36

2.1.3.1 X-Ray diffraction 36

2.1.3.1.1 Geometry of diffraction 36

2.1.3.1.2 Powder X-ray diffraction 40

2.1.3.1.3 X-Ray source 40

Page

2.1.3.1.4 Bragg-Brentano configuration 42

2.1.3.1.5 Phase identification 42

2.1.3.1.6 Crystallite size and strain determination 43

2.1.3.1.7 Scherrer equation (crystallite size) 44

2.1.3.1.8 Williamson-Hall method (crystallite size and strain) 46

2.1.3.1.9 Precise lattice parameter determination 47

2.1.3.2 Electron microscopy 49

2.1.3.2.1 Scanning electron microscopy 49

2.1.3.2.2 Transmission electron microscopy 51

2.1.3.3 Energy dispersive x-ray spectroscopy 56

2.1.3.4 Particle-induced X-ray emission spectrometry 58

2.1.3.5 Raman spectroscopy 59

2.1.3.6 Microhardness 61

2.1.3.7 Differential thermal analysis 63

2.2 Specific experimental details 64

2.2.1 Copper-carbon composite 66

2.2.2 Nickel-carbon composite 68

2.2.3 Tungsten-carbon composite 69

2.2.4 Transformation of nanodiamond into onion-like carbon 69

2.3 References 70

Chapter 3 – Copper-carbon composites

3.1 Introduction 78

3.2 Results and discussion 78

Page

3.3 Summary 110

3.4 References 110

Chapter 4 – Nickel-carbon composites

4.1 Introduction 116

4.2 Results and discussion 116

4.3 Summary 142

4.4 References 142

Chapter 5 – Tungsten-carbon composites

5.1 Introduction 147

5.2 Results and discussion 147

5.3 Summary 155

5.4 References 155

Chapter 6 – Transformation of nanodiamond into onion-like carbon

6.1 Introduction 159

6.2 Results and discussion 159

6.3 Summary 171

6.4 References 171

Chapter 7 – Concluding remarks 175

Page

Figure Index

Figure

1.1 – OLC particles formation [27]. 5

1.2 – Comparison of conventional Hall–Petch relationship and the model proposed by Zhao *et al.* [72] for (a) Cu and (b) Ni. 12

2.1 – Example of ball-powder collisions during milling [1]. 27

2.2 – Refinement of particle and grain sizes with milling time [1]. 28

2.3 – (a) Retsch planetary ball mill [14]. (b) Working principle of a planetary ball mill [15]. 30

2.4 – Spark plasma sintering diagram [30]. 34

2.5 – Hot (direct) extrusion diagram [33]. 35

2.6 – (a) Diffraction representation along the *x*-axis. The incident and diffracted beams are at α_0 and α_n to the row. The path difference between the diffracted beams is AB – CD [34]. 36

2.7 – The incident and diffracted beam directions and the path difference between the diffracted beams expressed in vector notation [34]. 37

2.8 – (a) Representation of the intersection of the two cones originating at a common apex [34]. (b) Diffraction cones from three non-coplanar rows of scattering atoms in common line [35]. 37

2.9 – Geometry behind Bragg's diffraction [36]. 39

2.10 – Ewald construction [34]. 40

2.11 – Transitions that give rise to the various X-ray lines [38]. 41

2.12 – Schematic representation of a sample mounted on a goniometer stage which can be rotated about one or more axis, and a detector which travels along the focusing circle in the Bragg-Brentano geometry. F is the X-ray source, DS is the divergence scatter slit, SS is the soller slit assembly (SS1 on "tube" side, SS2 on detector side). RS is the receiving slit, C is the monochromator crystal, rm is the radius of the monochromator circle on which RS, C and AS (the detector slit) lie, rf is the radius of the focusing circle. F, S and RS all fall on this circle. The angles are indicated [39]. 42

2.13 – Bragg reflection from a crystal of thickness D. The crystal is (a) at the exact Bragg angle θ and (b) at a small deviation from the exact Bragg angle i.e. angle 45

Page

(θ+$\Delta\theta$). The arrows represent the incident and reflected beams from successive planes 0,1,2,3… (m/2) (half-way down) and … m (the lowest plane) [34].

2.14 – (a) Broadened Bragg peak arising from a crystal of finite dimension. β is equal to $2\Delta\theta$. The angular 2θ scale is measured in relation to the direct and reflected beams. (b) The Ewald reflecting sphere construction for a broadened reflected beam, where β, which corresponds to an extension $1/D$ of the reciprocal lattice node [34]. 46

2.15 – Diffraction signal originating from below the focusing plane (sample surface) [45]. 48

2.16 – Diagram of a scanning electron microscope [48]. 50

2.17 – Interaction volume with indication of signal origin [49]. 51

2.18 – Diagram of a transmission electron microscope [50]. 52

2.19 – Optical system of TEM: (a) diffraction mode and (b) imaging mode [51]. 53

2.20 – Bright-field mode of imaging [52]. 54

2.21 – (a) Off-axis dark field mode (higher aberrations) and (b) On-axis dark field mode (minimization of lens aberrations) [52]. 54

2.22 – Ray diagram showing SAD pattern formation: the insertion of an aperture in the image plane results in the creation of a virtual aperture in the plane of the specimen (shown here slightly above the specimen plane). Only electrons falling inside the dimensions of the virtual aperture at the entrance surface of the specimen will be allowed through into the imaging system to contribute to the SAD pattern. All other electrons will hit the SAD diaphragm [51]. 55

2.23 – Diffracted and transmitted beam paths [53]. 56

2.24 – Energy dispersive X-ray spectrometer in an electron microscope [54]. 57

2.25 – PIXE set-up [58]. 59

2.26 – Energy level diagram representing the elastic Rayleigh scattering and the inelastic anti-Stokes and Stokes Raman scattering [62]. 61

2.27 – Slip-line field produced by a Vickers indenter [80]. 63

2.28 – Diagram of a DTA furnace [84]. 64

3.1 – Experimental X-ray diffractograms of milled/extracted nD (a), pristine nD (b), milled/extracted G (c), and pristine G powders (d). 79

3.2 – Bright–field TEM images of Cu–10nD (a) and Cu–10G (b) composites milled for 4 h. Cu–10nD composites milled for 4 h and heat-treated at 873 K (c) and 973 K (d). 81

Page

The arrows indicate low–Z contrast regions. The A in (d) indicates a large carbon-rich region.

3.3 – Bright–field TEM images of the Cu–0.1Cr–10nD composite milled for 4 h (a) and Cu–0.1Cr–10nD composite milled for 4 h and heat-treated at 873 K (b). The arrows indicate low–Z contrast regions. 82

3.4 – (a) Bright–field TEM image of the milled/extracted nD powder. (b) Ring diffraction pattern obtained from a large area similar to (a) with integrated radial profile (diamond simulation included with legend in nm^{-1}). (c) Bright–field TEM image of the milled/extracted G powder with EDS point analysis (the TEM grid contributed to the Cu peak). (d) Ring diffraction pattern obtained from a large area similar to (c) with integrated radial profile (graphite and α–Fe simulations included with legend in nm^{-1}). 84

3.5 – Bright–field TEM images of milled/annealed/extracted materials nD: (a) 773 K, (b) 873 K (b), (c) 973 K (c) and (d) 1073 K. (e) Pristine nD powder annealed at 1073 K, and (f) ring diffraction pattern obtained from a large area similar to (e) with integrated radial profile (diamond simulation included with legend in nm^{-1}). 85

3.6 – Raman spectra of milled/extracted and pristine nD (a) and milled/extracted and pristine G (b). Milled/annealed/extracted nD (c) and milled/annealed/extracted G (d) at several annealing temperatures. 86

3.7 – (a) BSE SEM image and (b) bright–field TEM image of the Cu–10nD material milled for 4 h and subsequently consolidated by hot extrusion at 873 K. (c) BSE SEM image and (d) bright–field TEM image of the Cu–0.1Cr–10nD material milled for 4 h and subsequently consolidated by spark plasma sintering at 1073 K1073 K. The arrows in (c) indicate the prior powder boundaries, while in (b) and (d) indicate the low–Z contrast regions. 88

3.8 – (a) Cu grain diameter evolution with milling time in both Cu–10nD and Cu–10G composites (XRD data – Scherrer equation). (b) Cu grain diameter in Cu–10nD composites milled for 4 h (TEM measurements and XRD data – Scherrer equation) and in Cu–10G composites milled for 4 h (XRD data – Scherrer equation) against temperature (1 h annealing). (c) nD particle diameter in Cu–10nD composites milled for 4 h (TEM) against temperature (1 h annealing). The number of grains/particles measured from TEM micrographs (n) is indicated above each point with error bars. 90

3.9 – Histograms of carbon particle size (diameter) measured from TEM micrographs. The total number of particles measured (n) and the average diameter (d) are indicated in the legend for each condition. 92

Page

3.10 – Cu grain diameter (XRD (Scherrer equation) and TEM) against carbon particle average radius (TEM). The Zener model prediction is also shown. 82

3.11 – Relation between hardness and Cu grain size (XRD – Scherrer equation) for the Cu–10nD, Cu–0.1Cr–10nD, and Cu–10G composites. Curves commonly accepted for pure nanostructured Cu is shown for comparison [31,32]. 95

3.12 – (a) Experimental lattice parameter evolution (a_{Cu}) with milling time (the pristine Cu lattice parameter is also presented). (b) Lattice parameter evolution with annealing treatments for the materials milled for 4 h. An estimated error of 0.0005 nm in lattice parameter was associated to the measurements [40,41]. 97

3.13 – Orowan-Ashby model for perfect and partial dislocations. The nanocomposite distinction reflects the different volume fraction (5 % for nD and 7 % for G). The inset shows carbon clusters with sizes ≤ 5 nm dispersed within Cu grains of the milled (4 h) and annealed (773K/1h) Cu-10nD composite. 100

3.14 – (a) Iron concentration versus milling time determined from 10 EDS point analyses. (b) BSE image of Cu-10nD as-milled powders after 4 h of milling with corresponding X-ray maps: Fe in (c) and Cr in (d). A Fe,Cr-rich inclusion is evidenced by the squares. 101

3.15 – Relation between Cu grain size and hardness calculated with the cumulative model. Experimental hardness values show reasonable agreement with the model for (a) Cu-10nD and (b) Cu-10G nanocomposites. Error bars are presented and fall within the respective point. 108

3.16 – Contribution of each strengthening mechanism for milling times of 2, 4 and 6 h. (a) Cu-10nD and (b) Cu-10G composites. 109

4.1 – (a) BSE SEM images of Ni–10nD composites milled at 200 rpm for 1h and (b) milled for 4 h. 117

4.2 – Experimental X–ray diffractograms of the as-milled nanocomposites. (a) 4 h Ni–10nD (200 rpm, (b) 4 h Ni–20nD (200rpm), (c) 4 h Ni–10nD (400 rpm), and (d) 4 h Ni–20nD (400 rpm). (e) 4 h Ni–10G (200 rpm), (f) 4 h Ni–20G (200 rpm), (g) 4 h Ni–10G (400 rpm), and (h) 4 h Ni–20G (400 rpm). 118

4.3 – Bright–field TEM images of 10 at.% C nanocomposites milled for 4 h at 200 rpm. (a) Ni–10nD. (b) Diffraction pattern obtained from a large area similar to (a) with integrated radial profile (Ni and NiO simulations included with legend in nm^{-1}). (c) Ni–10G. (d) Diffraction pattern obtained from a large area similar to (c) with integrated 120

radial profile (Ni simulation included with legend in nm^{-1}). (e) Ni-10nD composite milled for 4 h and heat-treated at 1073 K. The region A in (e) corresponds to a large carbon-rich particle. Carbon–rich regions within a Ni grain are shown in the magnified inset of (e). The arrows indicate low–Z contrast regions.

4.4 – (a) Bright–field TEM image of carbon extracted from a Ni–10nD composite. (b) Diffraction pattern obtained from a large area similar to (a) with integrated radial profile (diamond simulation included with legend in nm^{-1}). (c) Bright–field TEM image of carbon extracted from a Ni–10G composite. (d) Diffraction pattern obtained from a large area similar to (c) with integrated radial profile (graphite simulation included with legend in nm^{-1}). 122

4.5 – (a) Bright–field TEM image of the carbon phases extracted from the Ni–10nD milled composite annealed at 1073 K. (b) Diffraction pattern obtained from a large area similar to (a) with integrated radial profile (graphite simulation included with legend in nm^{-1}). (c) Bright–field TEM image of the carbon phases extracted from the Ni–10G milled composite and annealed at 1073 K. (d) Diffraction pattern obtained from a large area similar to (c) with integrated radial profile (graphite simulation included with legend in nm^{-1}). 123

4.6 – Raman spectra of pristine nD, milled/extracted, milled/annealed/extracted nD and annealed pristine nD powders (a). Raman spectra of pristine G, milled/extracted and milled/annealed/extracted G powders (b). 125

4.7 – Relation between hardness and Ni grain size (XRD – Scherrer equation) for the Ni–10nD and Ni–10G composites. A curve commonly accepted for pure nanostructured Ni is shown for comparison. 128

4.8 – (a) Experimental lattice parameter evolution with milling time (the pristine Ni lattice parameter is also presented). (b) Lattice parameter evolution with annealing treatments for the materials milled for 4 h. An estimated error of 0.0005 nm in lattice parameter was associated to measurements [27,28]. 129

4.9 – (a) Measured iron concentration (left-hand axis) for milling times of 4, 6 and 8 h, and expansion of Ni lattice parameter (right-hand axis) determined through the Fe-Ni Vergard's law [29,30]. (b) Lattice parameter expansion induced by C in solution (left-hand axis) determined from the measured lattice parameter by subtracting the effect of Fe, and C solute (right-hand axis) determined from the C-Ni Vergard's law [31]. Relative effect of Fe and C on the Ni lattice parameter expansion against milling time for Ni-10nD (c) and Ni-10G (d). 131

Page

4.10 – Orowan-Ashby model for perfect and partial dislocations. The nanocomposite distinction reflects the different volume fraction (5 % for nD and 8 % for G). 133

4.11 – Hardness calculated with the carbon solid solution term versus carbon concentration. 138

4.12 – Relation between Ni grain size and hardness calculated with the cumulative model. Experimental hardness values show reasonable agreement with the model for (a) Ni-10nD and (b) Ni-10G nanocomposites. Error bars frequently fall within the respective data point symbol. 139

4.12 – Contribution of each strengthening mechanism for milling times of 4, 6, and 8 h. (a) Ni-10nD and (b) Ni-10G nanocomposites. 141

5.1 – Experimental X-ray diffractograms of pure W (a), W–G (10 and 20 at.%) (respectively, (b) and (c)), and W–nD (10, 20 and 40 at.%) (respectively, (d), (e) and (f)) after milling at 200 rpm for 4 h. 149

5.2 – Experimental X-ray diffractograms of W-40nD milled for 2 h at 200 rpm (a), 4 h at 200 rpm (b), 2 h at 300 rpm (c) and 2 h at 400 rpm (d). 149

5.3 – BSE SEM images of the W-20nD milled at 200 rpm for (a) 2 h or (b) 4 h. W-20G milled at 200 rpm for 4 h (c). The arrows indicate the W carbide inclusions. 150

5.4 – (a) Bright-field TEM image of the W–20nD material milled for 4 h at 200 rpm. (b) Diffraction pattern obtained from a large area similar to (a) with integrated radial profile (W simulation included with legend in nm^{-1}). The arrows indicate low–atomic number regions. Bright-field TEM images of the particles extracted from the milled W–20nD composite showing both nD (c) and W_2C particles (e). (d) Ring diffraction pattern obtained from a large area similar to (c) with integrated radial profile (diamond simulation included with legend in nm^{-1}). (f) Ring diffraction pattern obtained from a large area similar to (e) with integrated radial profile (W_2C simulation included with legend in nm^{-1}). 152

5.5 – BSE SEM image of the W-40nD material milled at 200 rpm for 4 h and subsequently consolidated by spark plasma sintering. 153

5.6 – DTA heating curve of the W–20nD material milled at 200 rpm for 4 h. 155

Page

6.1 – DTA measurements of the materials milled at 200 rpm for 4 h and pristine nD used as control. (a) Pristine nD, (b) nD(Cu), (c) nD(Ni) and (d) nD(W) materials. DTA curves appear as gray lines and the derivative curves as dark lines. Insets are included for identification of the carbon phase transitions. 161

6.2 – Experimental X-ray diffractograms of the materials milled at 200 rpm for 4 h and subsequently heated: (a) nD(Cu), (b) nD(Cu) after DTA up to 1323 K, (c) nD(Ni), (d) nD(W), and (e) nD(W) heated up to 1173 K and (f) at 1323 K. The intense matrix reflections, and the corresponding background level, obscured the carbon phase peaks. 162

6.3 – Bright-field TEM images of the carbon phases. (a) Pristine nD and as-milled (b) nD(Cu), (c) nD(Ni) and (d) nD(W) (d) showing particles with sizes in the 5-20 nm range. (d) Typical diffraction pattern of the nD particles with an integrated radial profile (diamond simulation included with legend in nm^{-1}). 163

6.4 – Bright-field TEM images of the heated-exposed materials. (a) Pristine nD powder heated up to 1723 K, (b) nD(Cu) up to 1723 K, (c) nD(W) up to 1673 K, (d) nD(Ni) up to 1423 K, (e) nD(Ni) up to 1573 K, (f) nD(Ni) up to 1673 K, and (g) characteristic diffraction pattern of the OLC particles with an integrated radial profile (graphite simulation included with legend in nm^{-1}). 164

6.5 – Raman spectra evolution with heat exposure for the (a) pristine nD, (b) nD(Cu), (c) nD(Ni) and (d) nD(W) materials. 165

6.6 – (a) and (b) Bright-field TEM images of the extracted Ni-10nD composite milled heated at 1673 K. (c) Ring diffraction pattern with integrated radial profile (graphite simulation included with legend in nm^{-1}). 170

Table Index

Table

3.1 – Milling media contamination of as–milled materials evaluated by PIXE and EDS. 82

3.2 – Vickers microhardness and Cu grain diameter obtained with TEM, Scherrer equation and Williamson-Hall method (WH) for the milled and heat-treated Cu–10nD, Cu–0.1Cr–10nD, and Cu–10G composites. The microhardness of the consolidated materials is also presented. 96

Page

3.3 – Parameters used in the analysis of the Orowan-Ashby mechanism effect (Equation 1.16). 99

3.4 – Initial carbon volume fraction, lattice parameter, Cu grain diameter obtained with Scherrer equation, iron concentration and Vickers microhardness for the 2, 4 and 6 h milling times conditions. 103

3.5 – Theoretical parameters used in the cumulative model. 106

3.6 – Parameters determined from fitting the cumulative model. 106

3.7 – Volume fraction of C and stainless steel clusters with 5 nm in diameter dispersed in the matrix. 107

3.8 – Experimental hardness and calculated hardness values. The relative error is also presented. 107

4.1 – Contamination from milling media for different milling energy (rotation speed) for 4 h of milling time (average of 10 EDS point analyses). 117

4.2 – Vickers microhardness and Ni grain diameter obtained with Scherrer equation and Williamson-Hall method (WH) for the milled and heat–treated Ni–10nD and Ni–10G composites. 127

4.3 – Parameters used in the analysis of the Orowan-Ashby mechanism (Equation1.16). 133

4.4 – Ni lattice parameter, Ni grain size obtained with Scherrer equation, carbon and iron in solution, volume fraction of reinforcing particles and Vickers hardness for the 4, 6 and 8 h milling time conditions. 136

4.5 – Theoretical parameters used in the cumulative model. 137

4.6 – Parameters determined from fitting the cumulative model. 138

4.7 – Experimental hardness and calculated hardness values. The relative error is also presented. 140

5.1 – Microhardness values of pure W and W–G and W–nD materials milled at 200 rpm. Pure W, W–20nD and W–20G exposed to continuous heating up to 873 K at 20 $K.min^{-1}$ are also presented. 154

6.1 – Milling media contamination for 4h of milling time and 200 rpm (average of 10 EDS point analyses). 160

Acronyms

BF – Bright field

BSE – Backscattered electrons

CCD – Charged-coupled device

DF – Dark field

DC – Direct current

DTA – Differential Thermal Analysis

EDS – Energy dispersive spectroscopy

HE – Hot extrusion

HIP – Hot isostatic pressing

HP – Hot press sintering

PXRD – Powder X-ray diffraction

PIXE – Particle-induced X-ray emission spectrometry

SAD – Selected-area diffraction

SE – Secondary electrons

SEM – Scanning electron microscopy

SPS – Spark plasma sintering

TEM – Transmission electron microscopy

XRD – X-ray diffraction

Symbols

AB – path between A and B points

A – indentation contact area

a – lattice parameter and interatomic distance

$\boldsymbol{a}$ – translation vector from one lattice site to the next along x-axis

$\boldsymbol{a}^*$ – translation vector from one lattice site to the next along x-axis in reciprocal lattice

at.% – atomic percentage

α – molecular polarizability

α – constant

$\boldsymbol{\alpha}$ – dislocation character

α_n – angle between the diffracted beam and x-axis

α_0 – angle between the incident beam and x-axis; zero order semi-apex angle

b – lattice parameter and interatomic distance

$\boldsymbol{b}$ – displacement of the matrix atoms

$\boldsymbol{b}$ – translation vector from one lattice site to the next along y-axis

$\boldsymbol{b}^*$ – translation vector from one lattice site to the next along y-axis in reciprocal lattice

b – Burgers vector

β – peak width at half the maximum intensity

β_m – peak width at half the maximum intensity measured

β_i – instrumental broadening

β_n – angle between the diffracted beam and y-axis

β_0 – angle between the incident beam and y-axis

CD – path between C and D points

C_rO – equal to incident wave vector $\mathbf{S_0}$

C_rP – equal to diffracted wave vector **S**

c – lattice parameter and interatomic distance

c – translation vector from one lattice site to the next along *z*-axis

c* – translation vector from one lattice site to the next along *z*-axis in reciprocal lattice

C – concentration

C_s – solute concentration

C_{st} – standard concentration

C_i – concentration of an *i* element

c_p – specific heat of the powders

D – grain size

D – peak of graphite

D' – peak of graphite

d – Arithmetic mean of the Vickers indentation diagonal lengths

d –inner diameter of a container

d_{hkl} – interplanar distance

δ – load transfer parameter

E – line energy of the dislocation

E – Elastic moduli

E – external electric field

$E(\theta)$ – line energy

$E(x)$ – solute-interface interaction energy

eV – electron Volt

ε_G – constant related to strain caused by difference in modulus

ε_b – constant related to strain caused by difference in size

ε – lattice strain

ξ – outer cut-off radius of the dislocation

F – applied load

F – interaction force with a solute atom

F_0 – activation energy needed at zero applied stress

f – single interaction i.e. proportional to the energy barrier associated to with a single solute atom

f – volume fraction of dispersed particles

ϕ – dissipated energy flux

ϕ – half the cusp angle formed by the dislocation at an obstacle just at the point of break-through

G – peak of graphite

G – Shear modulus

ΔG – activation energy

g – gravitational acceleration

g – reciprocal lattice vector

γ – energy of the pinned grain boundary

γ – stacking fault energy

γ_n – angle between the diffracted beam and z-axis

γ_0 – angle between the incident beam and z-axis

H – hardness

H_{Comp} – composite hardness

H_0 – temperature dependent material constant representing the resistance of the lattice to dislocation motion that includes solute strengthening effects after applying Tabor relationship

H_0^Z – temperature independent term that represents the resistance of the lattice to dislocation motion after applying Tabor relationship

HV – Vickers hardness number

H_R – reinforcement hardness

$\mathcal{H}_m$ – bulk melting enthalpy

h – Miller indice

h – atomic or molecular diameter

ℎ – height of the diffraction signal from bellow the focusing plane

ℏ – specimen shift

I_{st} – peak intensity for the *i* element in the standard sample

I_i – measured peak intensity

$\mathcal{K}$ – correction factor

K – Scherrer factor

K – diffraction vector

$\mathcal{K}$ – solid solution parameters

K_α – transition from the L to the K shells

K_β – transition from the M to the K shells

k – thermal expansion coefficient

k – Miller index

k – critical value of maximum shear stress

k – Kocks constant

k_0 – thermal conductivity of the particles

k_{σ}^{D} – constant dependent on the resistance of grain boundaries to dislocation movement

k_{H}^{D} – constant dependent on the resistance of grain boundaries to dislocation movement after applying Tabor relationship

k_{σ}^{Z} – constant and the exponential factor represents the effect of grain size effect on melting temperature

k_{H}^{Z} – constant and the exponential factor represents the effect of grain size effect on melting temperature after applying Tabor relationship

L - camera length

l – Miller index

λ – wavelength

λ – half width of the interface

λ – particle or solute atom spacing in the slip plane

M – Taylor factor

m – exponent that depends on how the average spacing λ is defined

m – number of planes

$\mathbf{M}(t)$ – dragged grain boundary mobility in function of time

$\mathbf{M}_{\mathrm{Pure}}$ – intrinsic grain boundary mobility

N_c – critical rotation speed

n – exponent that varies on the assumptions concerning the nature of the obstacles

ν – relative velocity of the ball before impact

ν – Poisson ratio

OP – reciprocal lattice **g** or distance between the origin of the reciprocal lattice and point P

O – parameter that contributed to fit the cumulative model associated to the 5 nm clusters dispersed in the nanostructured matrix

P – pressure normal to the surface of the indenter

P – point where the diffracted beam intercepts the Ewald's sphere

P – pressure

P – electric dipole moment

$\boldsymbol{P}$ – solute drag force

p – exponent that depends on the nature of the solute

q – exponent that depends on the nature of the solute

ρ_p – density of the powder particles

R – radius of the goniometer circle

R – distance between the transmitted beam and a diffraction spot

$\mathcal{R}$ – ideal gas constant

$\boldsymbol{R}$ – lattice atomic radius

r – radius of balls

$\boldsymbol{r}$ – nearest interaction distance

r – particle radius

r_{p} – planar radius

r_0 – inner cut-off radius of the dislocation

rpm – rotation per minute

S – unit vector along the direction of the diffracted beam; diffracted wave vector

$\mathbf{S_0}$ – unit vector along the direction of the incident beam; incident wave vector

$\boldsymbol{\sigma}$ – normal stress due to a head-on collision

σ – yield (normal) stress

σ_0 – temperature dependent material constant representing the resistance of the lattice to dislocation motion that includes solute strengthening effects

σ_0^Z – temperature independent term that represents the resistance of the lattice to dislocation motion

T – temperature

$\mathcal{T}$ – line tension

t – time

τ – critical resolved shear stress

τ_T – critical resolved shear stress at some temperature

τ_0 – critical resolved shear stress at 0 K

θ – scattering or diffracting angle

vol.% - volume percentage

V_m – velocity of the migrating interface

υ_m – molecules vibration frequency

υ_0 – laser light frequency

x – direction

$\mathcal{X}$ – distance between the solute and the dislocation along the slip plane

wt.% – weight percentage

y – direction

Z – atomic number

z – direction

Δt – stress state life

ΔV – Raman shift

N.B.:

Chemical element symbols have not been listed nor as SI units.

List of publications related to this thesis:

D. Nunes, V. Livramento, U.V. Mardolcar, J.B. Correia, P.A. Carvalho, Tungsten-nanodiamond composite powders produced by ball milling, Journal of Nuclear Materials 426 (2012) 115–119.

D. Nunes, M. Vilarigues, J.B. Correia, P.A. Carvalho Nickel-carbon nanocomposites: Synthesis, structural changes and strengthening mechanisms, Acta Materialia 60 (2012) 737–747.

D. Nunes, V. Livramento, N. Shohoji, H. Fernandes, C. Silva, J.B. Correia, P.A. Carvalho, Copper-μDiamond Nanostructured Composites, Physica Scripta T145 (2011) 014069.

D. Nunes, V. Livramento, R. Mateus, J.B. Correia, L.C Alves, M. Vilarigues, P.A. Carvalho, Processing copper-carbon nanocomposites by mechanical synthesis: Structural changes and thermal stabilization, Materials Science and Engineering A 528 (2011) 8610–8620.

D. Nunes, J.B. Correia, P.A. Carvalho, N. Shohoji, H. Fernandes, C. Silva, L.C. Alves, K. Hanada, E. Ōsawa, Production of Cu/Diamond composites for first-wall heat sinks, Fusion Engineering and Design 86 (2011) 2589–2592.

V. Livramento, D. Nunes, J.B. Correia, P.A. Carvalho, U. Mardolcar, R. Mateus, K. Hanada, N. Shohoji, H. Fernandes, C. Silva, E. Alves, Tungsten-micro diamond composites for plasma facing components, Journal of Nuclear materials 416 (2011) 45–48.

D. Nunes, V. Livramento, J.B. Correia, K. Hanada, P.A. Carvalho, R. Mateus, N. Shohoji, H. Fernandes, C. Silva, E. Alves, E. Osawa, Consolidation of Cu-nDiamond nanocomposites; hot extrusion vs spark plasma sintering, Materials Science Forum 636-637 (2010) 682–687.

D. Nunes, V. Livramento, J.B. Correia, R. Mateus, P.A. Carvalho, N. Shohoji, H. Fernandes, C. Silva, E. Alves, K. Hanada, E.Osawa, W-nDiamond/Cu-nDiamond nanostructured composites for fusion devices. Proceedings of MRS Symposium R on Materials for Future Fusion and Fisson Technologies, MRS Symposium Proceedings Series, Materials Research Society 1125 (2009) 59–64.

V. Livramento, J.B. Correia, D. Nunes, P.A. Carvalho, H. Fernandes, Novel Approach to Plasma Facing Materials in Nuclear Fusion Reactors. Plasma and Fusion Science: 17th IAEA Technical Meeting on Research Using Small Fusion Devices. AIP Conference Proceedings 996 (2008) 166–171.

D. Nunes, V. Livramento, H. Fernandes, C. Silva, N. Shohoji, J.B. Correia, P.A. Carvalho, Multiscale Copper-μDiamond Nanostructured Composites, Proceedings of Materiais 2011 on Materials Science Forum 730–732 (2013) 925-930.

D. Nunes, M. Vilarigues, U.V. Mardolcar, M.F. Montemor, J.B. Correia, P.A. Carvalho, Catalytic effect of metals on the formation of onion-like carbon, Carbon (in preparation).

D. Nunes, A. Moita de Deus, M.F. Pereira, J.B. Correia, P.A. Carvalho, Cumulative strengthening mechanisms on metal-carbon nanostructured composites, Acta Materialia (in preparation).

Chapter 1

Chapter 1 – Introduction

1.1 Motivation

A microstructure refined to the nanometer scale improves mechanical strength [1]. However ultra-fine grain metals exhibit low thermal stability even at moderate temperatures [2,3], requiring the presence of particle dispersions to delay coarsening by grain boundary (GB) pinning [4]. The concept of a composite is also applicable to nanostructured materials, allowing tailoring functional properties [5]. In the case of carbon dispersions in metals, thermal stabilization and reinforcing effects can be combined with specific properties of the carbon phases, such as high thermal conductivity for diamond [6] and self-lubricating properties for graphite [7]. Nevertheless, the primary challenge lies in dispersing the carbon phase in the metallic matrices.

High-energy ball milling is a powder metallurgy process that has been extensively used to produce nanostructured materials [8], as well as fine particle dispersions in metallic matrices [5,9-11]. High-energy milling has also been employed to process carbon nanostructures such as nano-sized ribbons, closed-shell nanoparticles [12,13], and carbon nanotubes (CNT) with subsequent annealing treatment [14]. Nevertheless, continued milling is known to induce amorphization of graphite [15-17], and to some extent the same can be expected for other carbon allotropes. Alternatively, compounds such as carbides can form during ball milling through solid-state reaction with metals [8]. In fact, while some metallic matrices exhibit extremely reduced affinity towards carbon phases, potentially compromising the composite interfaces, others are strong carbide formers where dispersing carbon phases represent a challenge. Close monitoring of the processing parameters is therefore required to establish suitable processing windows.

1.2 State of the art

1.2.1 Carbon phases

Nanodiamond (nD), onion-like carbon (OLC), CNT, synthetic graphite (G) and amorphous carbon (aC) are candidate phases for the carbon-based dispersions. However, CNT and their bundles are poorly wetted by metals [18] and are easily destroyed by high-energy milling [19]. On the other hand, aC and OLC can be produced from G and nD by high-energy milling or heat treatment, respectively [17,20]. Indeed, while carbon transformations induced by high-energy milling have been exhaustively studied over the years, the occurrence of phase transitions in dispersed carbon has not yet been investigated, representing an opportunity to tailor nanostructured metal-carbon composites. Graphite and nanodiamond have hence been selected for direct or precursor dispersion in the metallic matrices.

(i) Diamond

Diamond has the highest thermal conductivity, 2000 W/mK at 20°C, whereas copper (possessing one of the highest thermal conductivities among metals) presents a mere 400 W/mK [6]. Moreover, the hardness of diamond renders nD dispersions excellent reinforcing candidates [5]. On the other hand, it presents a lower thermal expansion coefficient ($k_{diamond} = 1 \times 10^{-6}$ K^{-1} at 273 K [21]) then metals (e.g. $k_{copper} = 16 \times 10^{-6}$ K^{-1} at 273 K [22]), which is a severe drawback for direct application, either in bulk or film form, in thermal management applications.

Collateral damage of milling media tends to occur in the presence of hard phases [8] such as micro-sized diamond, which however may be mitigated by the reported self-lubricating properties of nano-sized diamond [23]. Nevertheless, the question remains whether at the nanoscale the diamond structure can resist to high-energy milling without substantial amorphization.

(ii) Onion-like carbon

Upon annealing bulk diamond graphitizes into planar graphite, whereas nD transforms into onion-like carbon [20]. OLC produced by annealing of nD has been extensively studied [20,24-26] mainly due to its potential application in electromagnetic devices, field emission and solid lubricants [24]. The OLC formation process from nD particles involves: (i) formation of graphite fragments, (ii) connection and curvature of graphite sheets at the edges of diamond {111} planes, and ensuing closure of the graphite layers. Diamond nanoparticles have dangling sp^3 bonds at the surface, and its elimination through closure of graphite sheets with in plane sp^2-hybridized bonds results in a decrease of the surface energy, which has been hypothesized as the driving force to continuously form closed graphite shells (see Figure 1.1) [20,27]. This transformation requires heating the nD particles at temperatures above 1400 K due to the high energy required to keep on breaking C–C bonds in inner diamond [20]. Nevertheless, only limited information is currently available on OLC properties.

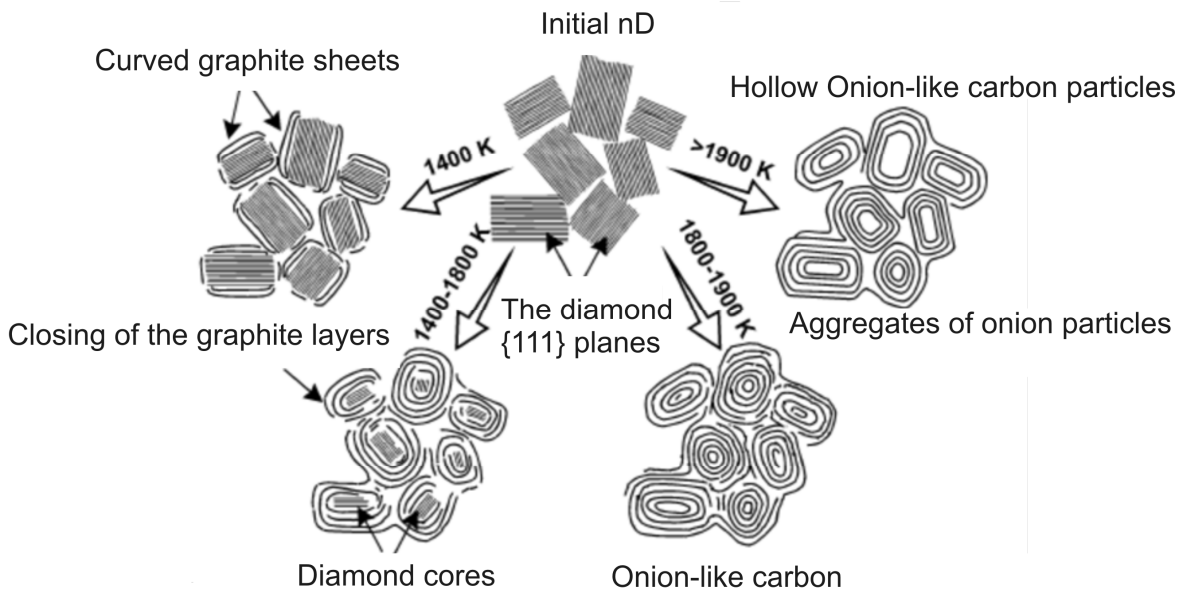

Figure 1.1. OLC particles formation [27].

(iii) Graphite

Graphite, although relatively weak, presents self-lubricating properties [7]. At the microscale, the incorporation of graphite particles improves the wear behavior of the matrix under dry conditions without important negative effects on thermal and electric conductivities [28,29]. Several studies have been carried out to characterize the structure and properties of milled graphite [12,13,17,30].

(iv) Amorphous carbon

The aC phase is kinetically obtained during milling if the amorphization reaction is faster than that of recrystallization [31]. Amorphization has been proposed to result from a grain size reduction below a critical value [32]. In the case of graphite, for a grain size of 2 nm, the grain boundary energy is sufficient to induce a crystalline to amorphous transition [33].

Amorphous carbon exhibits a mixture of sp^2 and sp^3 bonds, however as its semiconductor behavior shows, the properties of aC are not monotonically ranged between diamond and graphite [34]. Other significant properties are its irradiation tolerance, chemical inertness, hardness and wear resistance [35].

1.2.2 Metallic matrices

The matrix selection is aimed at responding to two fundamental challenges: some metals, such as copper, exhibit an intrinsically difficult bonding with carbon phases, which result in weak interfacial boundaries; while on the other end of the spectrum strong carbide forming metals, such as tungsten, tend to consume the dispersed carbon phases. Nickel, as mild carbide former [36,37], can be used as a metallic matrix with intermediate affinity characteristics.

Although graphite amorphization by high-energy milling is facilitated by metal doping [30], the effect of metals during nD milling is unknown. For carbide forming metals reaction milling is typically used to induce carbide formation [8,38] and limited literature reports exist on the dispersion of carbon phases [39,40].

Nevertheless, in these conditions carbide interlayers are expected to assist structural cohesion and, moreover, the systems may bear self-healing potential in case of decohesion induced by thermal fatigue.

(i) Copper matrix

Due to superior electrical and thermal conductivity, suitable corrosion resistance and relatively high melting point, copper-based alloys and composites have widespread use in static and sliding electrical contacts [41], as well as in thermal management applications ranging from electronic packaging [42] to heat sinks for nuclear reactor technology [43]. Yet, relatively low strength and limited thermal stability are restricting further use of these materials.

An alternative approach can be employed to overcome the intrinsically difficult bonding of copper with carbon phases [42]: incorporation of chromium in the copper matrix. This solute has the potential of enhancing the adhesion between the phases as it tends to segregate to the carbon/metal interfaces, forming a stable carbide interlayer that leads to improved heat and load transfer [44]. Indeed, thermal conductivities as high as 50% above that of pure copper, have been achieved for Cu-carbide-microdiamond composites, where carbide interlayers are assumed to aid the electron–phonon coupling necessary for heat transfer [44].

(ii) Tungsten matrix

Approximately half of the commercially available tungsten is consumed in the production of hard materials (WC) with the remaining being used for the fabrication of

alloys and steels [45]. Due to the high melting point, high resistance to plasma erosion and moderate tritium retention [46], refractory metals such as tungsten are currently under intense investigation for plasma-facing applications in nuclear fusion reactors [47]. Nevertheless, the demand for operation temperatures above the range proposed for ITER first wall (that will operate below 873 K) is still challenging, especially on what thermal conductivity and microstructural stability are concerned [47]. A microstructure refined to the nanometer scale lessens radiation embrittlement due to an increased number of defect recombination sites [48] and diamond dispersoids offer reinforcement potential to nanostructured W, in combination with thermal conductivity enhancement, especially with micro diamond, and microstructural stability. W-nD composites are envisaged for parts where thermal management is a major issue, such as divertor components in fusion reactors.

Critical issues regarding the use of diamond in fusion reactors are (i) *in situ* transmutation and phase transformations owing to high-energy neutrons [49] and the fact that (ii) tungsten reacts with the several carbon allotropes at elevated temperatures to form carbides [45]), which tends to limit the operation temperature. Whilst these stability aspects demand further research, the primary challenge lies in dispersing the carbon phase in the strong carbide former matrix by room temperature high-energy milling [50], while keeping the carbide reaction at a minimum through close monitoring of the processing parameters [51].

(iii) Nickel matrix

Nickel alloys and composites present high electrical and thermal conductivity, high strength, ductility and wear resistance, good magnetostrictive properties, and corrosion-resistance at room temperature due to a slow oxidation rate [52]. These materials are used in a variety of applications ranging from catalysts for hydrogenation reactions [53] to protection of friction parts [54] and advanced turbine jet engines [55-57].

The interest in the interactions of Ni with carbon has increased as this metal was

found to be an efficient catalyst for the production of carbon nanotubes and fibers at elevated temperatures [58,59]. The transition of amorphous carbon into graphite at high temperature is also catalysed by the presence of Ni [58,60], and a similar effect is expected to decrease the temperature of nD conversion into OLC.

1.2.3 Strengthening and thermal stabilization mechanisms

Metal strengthening relies fundamentally on hindering dislocation mobility, which is affected by factors such as: solid solution, grain size and forced bowing around obstacles caused, for instance, by dispersed particles (Orowan mechanism). Effective load transfer to hard particles can also strengthen the matrix through reinforcement, and the strengthening mechanisms are generally considered cumulative [61-63]. Thermal stabilization of strength can be achieved by retarding GB motion through solute drag or by particle dispersion (Zener pinning).

(i) Solid solution strengthening

Interstitial or substitutional solutes cause local lattice strain, which interacts with the dislocation strain fields delaying their motion. Moreover, solute atoms tend to diffuse to the dislocation cores in search for sites more suited to their radii. This reduces the overall strain energy through partial cancelling of the dislocation strain field but pins down the dislocation. In general, solid solution strengthening depends on the size and concentration of the solute atoms, symmetry of the solute stress field and shear modulus of the solute atoms [64].

A classical model for describing the increase in yield stress from atoms in solid solution was presented by Fleischer [65]. In his theory, the strengthening is due to a combined effect arising from the differences in size and shear modulus between solutes and matrix atoms. The interaction force between a single solute and a dislocation was derived taking into consideration the dislocation type and the nature of the interaction

(size and/or modulus effect). For a dislocation of generic character the interaction force with a solute atom is given by:

$$F = \mathsf{G}\, \mathrm{b}^2 \boldsymbol{x} \boldsymbol{R}^3 \, |\varepsilon_{G-} \boldsymbol{\alpha} \varepsilon_b| \frac{1}{3\pi \boldsymbol{r}^4} \tag{1.1}$$

where G denotes the lattice shear modulus, b the Burgers vector of the dislocation, $\boldsymbol{x}$ the distance between the solute and the dislocation along the slip plane, $\boldsymbol{R}$ the lattice atomic radius and $\boldsymbol{r}$ the nearest interaction distance. The constants, ε_G and ε_b represent strains caused by the differences in modulus and size, respectively, and $\boldsymbol{\alpha}$ pertains to the dislocation character [66]. Kocks *et al.* [67] have proposed an expression to generalize discrete-obstacle models. The activation energy, ΔG, to overcome a discrete interaction is given by:

$$\Delta G = F_0 \left\{ 1 - \left(\frac{\tau_T}{\tau_0} \right)^p \right\}^q \tag{1.2}$$

where p and q depend on the nature of the solute. The critically resolved shear stress needed to overcome the interaction at some temperature T or at 0 K is represented by τ_T and τ_0 respectively. F_0 is the activation energy required at zero applied stress (τ = 0). Using the expression for the interaction force given by Fleischer (Eq. 1.1), and applying Friedel-statistics [67] the maximum stress at 0 K, can be expressed as:

$$\tau_0 = \frac{2T}{\mathrm{b}\lambda} f^{3/2} \tag{1.3}$$

where T is the line tension ($\approx \mathsf{G}\mathrm{b}^2/2$), λ is the average inter-solute spacing, and f is proportional to a single interaction i.e. proportional to the energy barrier associated to with a single solute atom. It should be mentioned that f may also be interpreted as a measure of the dislocation bow-out angle [67] at the obstacle, $f = \cos(\phi)$, and ϕ is half the cusp angle formed by the dislocation at an obstacle just at the point of break-through. In the limit of low concentrations and assuming a partially flexible dislocation line, λ is inversely proportional to the square root of the concentration c, expressed as atomic fraction. The exponent n varies on the assumptions concerning the nature of the obstacles [64], while m depends on how the average spacing λ is defined. Using the above

assumptions, the concentration dependence of the critical resolved shear stress can be written as [64,67]:

$$\Delta\tau = \mathrm{G}\, f^{\mathrm{n}}\, \mathrm{c}^{\mathrm{m}} \tag{1.4}$$

(ii) Grain size strengthening

The finer the grains, the larger the area of grain boundaries that impedes dislocation motion, thus grain size has a direct influence on the materials strength. The strengthening due to grain boundaries has been experimentally established ever since Hall [68] and Petch [69] proposed their relation between the grain size and the yield stress. The original explanation for the effect was that dislocations are assumed to pile-up against a grain boundary, thereby causing a stress concentration. When the stress concentration equals a critical stress, assumed to activate new dislocation sources, yielding starts in the next grain. The uniaxial yield strength variation with the average grain size D is then given by [68,69]:

$$\sigma = \sigma_0 + k_\sigma^D\, D^{-1/2} \tag{1.5}$$

where σ_0 is a temperature dependent material constant representing the resistance of the lattice to dislocation motion that includes solute strengthening effects and k_σ^D is a positive constant dependent on the resistance of grain boundaries to dislocation movement. Tabor [70] determined that a materials hardness can be related to the yield stress through: $H = 3\sigma$. Thus, a relation analogous to the Hall-Petch can be used to describe the hardness dependence on grain size [71]:

$$H = H_0 + k_H^D\, D^{-1/2} \tag{1.6}$$

where H, H_0, and k_H^D are related to the terms in equation 1.5 applying Tabor relationship. For grain sizes in the 10 μm to 100 nm range, the model predicted by equations 1.5 or 1.6 achieves reasonable agreement with experimental results [72]. However, for grain sizes < 100 nm, the temperature independent Hall-Petch model is no longer appropriate to

predict experimental results [72-76]. As the melting temperature of crystals is size-dependent at low scales, the materials assume high temperature behavior at relatively low temperatures where a contribution of grain boundary movement on plastic deformation is present [72] (see Figure 1.2). Zhao *et al.* proposed a temperature dependent model [72] that can be used to describe the behavior of nanostructured materials:

$$\sigma = \sigma_0^Z + \left[k_\sigma^Z + k_\sigma^D D^{-1/2}\right] exp\left[\frac{1}{T}\frac{\mathcal{H}_m/(3\mathcal{R})}{D/(6\mathrm{h})-1}\right] \tag{1.7}$$

or:

$$H = H_0^Z + \left[k_H^Z + k_H^D D^{-1/2}\right] exp\left[\frac{1}{T}\frac{\mathcal{H}_m/(3\mathcal{R})}{D/(6\mathrm{h})-1}\right] \tag{1.8}$$

where σ, k_σ^D and D have been defined for equation 1.5, σ_0^Z is a temperature independent term that represents the resistance of the lattice to dislocation motion, k_σ^Z is a constant and the exponential factor represents the effect of grain size on melting temperature, $\mathcal{H}_m$ is the bulk melting enthalpy, T is temperature, $\mathcal{R}$ is the ideal gas constant and h denotes atomic or molecular diameter. The terms in equation 1.8 are related to the correspondent terms in equation 1.7 through the Tabor relationship. When $D \rightarrow \infty$ then $\sigma_0^Z + k_\sigma^Z = \sigma_o$, the Hall-Petch relation (Eq. 1.5).

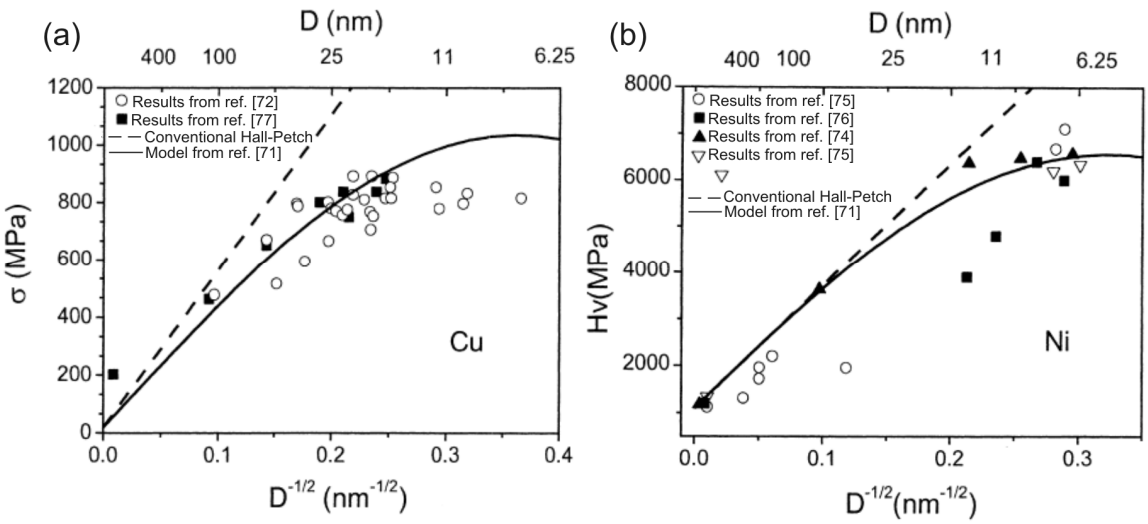

Figure 1.2. Comparison of conventional Hall–Petch relationship and the model proposed by Zhao *et al.* [72] for (a) Cu and (b) Ni.

(iii) Orowan strengthening

A possible strengthening mechanism at the finer scales is the one first proposed by Orowan [79], which comprises dislocation bowing out and bypassing undeformable particles, leaving a dislocation loop around them. The local stress shear stress, τ, is roughly equal to the stress required to bend a dislocation to a semi-circle of radius $\lambda/2$, where λ is the particle spacing in the slip plane and is:

$$\tau = \frac{2\,T}{\mathrm{b}\lambda} \tag{1.9}$$

where b is the magnitude of the Burgers vector and T is the line tension, assumed as the line energy of the dislocation (E):

$$E_{screw} = \frac{\mathrm{Gb}^2}{4\pi}\ln\frac{\xi}{r_0} \tag{1.10}$$

$$E_{edge} = \frac{\mathrm{Gb}^2}{4\pi(1-\nu)}\ln\frac{\xi}{r_0} \tag{1.11}$$

where G is the shear modulus, ν is the Poisson ratio, and ξ and r_0 are, respectively, the outer and inner cut-off radius of the dislocation. However, Ashby pointed out that when a screw dislocation is bowed out into a semicircle it acquires edge segments whose energy per unit length is greater than that of screw segments. It is thus more difficult to bend a screw than an edge dislocation between pinning points and equations 1.9 to 1.11 incorrectly predict that the reverse is true. Furthermore, the shape of the dislocation in its critical bowed-out state reflects this: in general the shape is not a semicircle [80,81]. The critical shape and stress are given by a line integral along the dislocation, taking the line tension as [82]:

$$T(\theta) = E(\theta) + \frac{\partial^2 E(\theta)}{\partial\theta^2} \tag{1.12}$$

where $E(\theta)$, the line energy, is a function θ. The "semicircle of radius $\lambda/2$" criterion for calculating the bypassing stress must therefore be substituted and can be taken as the stress at which the line slopes, at the points where the dislocation touches the two

particles between which it bows, become equal [80]. The result is that equations 1.9 to 1.11 should be replaced by [80,81]:

$$\tau_{edge} = \frac{\mathrm{Gb}}{2\pi\boldsymbol{\lambda}} \ln\left(\frac{\xi}{r_0}\right) \tag{1.13}$$

$$\tau_{screw} = \frac{\mathrm{Gb}}{2\pi(1-\boldsymbol{\nu})\boldsymbol{\lambda}} \ln\left(\frac{\xi}{r_0}\right) \tag{1.14}$$

The model was further modified by Ashby to incorporate the attractive interaction between the dislocation dipoles on either side of the particle, which tend to make bypassing easier. The energy of a dipole is given by equations 1.10 or 1.11 with the outer cutoff radius replaced by the dipole width, which in the case of the Orowan mechanism is 2*r*, the particle diameter. In its revised form, the strengthening due to the Orowan mechanism is described by the Orowan-Ashby equation (screw dislocation) [80,81]:

$$\Delta\tau = \frac{\mathrm{Gb}}{2\pi(1-\boldsymbol{\nu})\boldsymbol{\lambda}} \ln\left(\frac{r}{\mathrm{b}}\right) \tag{1.15}$$

where $\Delta\tau$ is the critical resolved shear stress (CRSS) increment above the matrix value due to the Orowan mechanism and *2*b is assumed as the inner cutoff radius of the dislocation. The yield stress increment of the equivalent polycrystalline material $\Delta\sigma$ can be related to $\Delta\tau$ through *M,* the Taylor factor [83] and k, the Kocks constant [80]:

$$\Delta\sigma = \mathrm{k}M\left(\frac{\mathrm{Gb}}{2\pi(1-\boldsymbol{\nu})^{1/2}\boldsymbol{\lambda}}\right) \ln\left(\frac{r}{\mathrm{b}}\right) \tag{1.16}$$

The Taylor factor accounts for an average grain orientation with σ = 3.06 τ [83]. The Kocks constant relates the applied stress to the average passing stress, i.e. it accounts for the fact that every spacing between a pair of particles has its own passing stress and that the average segment can move on indefinitely as long as 1/3 of the spacings between the particles allow bypassing [80]. The geometric mean $(1-\boldsymbol{\nu})^{1/2}$ in Equation 1.16 averages the screw and edge characters [84]. The particle spacing $\boldsymbol{\lambda}$ can be determined from the volume fraction of the dispersed particles *f,* by considering that the average particle radius *r* and its average planar radius r_p are related by the expression [85]:

$$r_p = \frac{\pi r}{4} \tag{1.17}$$

and that [85]:

$$\boldsymbol{\lambda} = \left(\frac{2\pi}{3f}\right)^{1/2} r - 2r_p \tag{1.18}$$

where the $2r_p$ subtraction accounts for the particles finite size.

(iv) Load transfer between the matrix and reinforcing phase

The concept of load distribution between the matrix and the reinforcing phase is central to understand the mechanical behavior of a composite. An external load applied to a composite is partly borne by the matrix and partly by the reinforcement. The reinforcement may be regarded as acting efficiently if it carries a relatively high proportion of the applied load. This can result in higher strength, as well as greater stiffness, since the reinforcement is usually stronger, as well as stiffer, than the matrix. Strengthening mechanisms involving dispersions demand hence strong particle/matrix interfaces.

The rule of mixtures represents the upper limit for strengthening by reinforcing particles [86], i.e., the largest effect that can be obtained when the matrix and reinforcement experience the same strain:

$$H_{Comp} = H_R\, f + H\,(1 - f) \tag{1.19}$$

where H_R and H are the reinforcement and matrix hardness, respectively and f is the volume fraction of dispersed particles. Correia *et al.* proposed to incorporate the reinforcement effect with the grain size dependence by replacing H with the Hall-Petch relation (Eq. 1.6) and introducing a load transfer parameter δ, that takes into account the difference in stiffness between the matrix and the reinforcing phase, the misfit of the reinforcing particles, the chemical affinity and the difference in the expansion coefficients [86]:

$$H_{Comp} = \delta\, H_R\, f + (H_0 + k_H^D\, D^{-1/2})\,(1 - f) \tag{1.20}$$

(v) Solute drag effect

Grain growth tends to occur in polycrystalline materials in order to reduce the system free energy associated with grain boundaries, especially at high temperature service conditions when grain boundary mobility is high. On the other hand, solute atoms segregated to grain boundaries, or other interfaces, decrease the overall free energy of the system. As a result, when interfaces move the solute atoms tend to lag behind exerting a dragging force [87]. Even at low solute concentrations, this dragging force may interfere with the material grain growth during heat exposure causing a coarsening retardation effect known as solute drag. Solute elements reduce GB mobility in a non-linear manner depending on the velocity and the effect has been treated extensively by Cahn [88] and simplified by Zurob *et al*. [89], who proposed that:

$$\mathbf{M}(t)=\left(\frac{1}{\mathbf{M}_{\mathrm{Pure}}}+\alpha\, c_s\right)^{-1} \tag{1.21}$$

where $\mathbf{M}(t)$ is the dragged grain boundary mobility in function of time, $\mathbf{M}_{\mathrm{Pure}}$ is the intrinsic grain boundary mobility, α is a constant and c_s is the solute concentration.

(vi) Zener pinning

Small particles dispersed in a material can exert a pinning force on moving grain boundaries [90], representing another important mechanism for controlling grain growth. In the classical treatment proposed by Zener, the solid particles exert a retarding force or pressure [91] that can be expressed as [92]:

$$P_{zener} = \frac{3\gamma f}{2r} \tag{1.22}$$

where f is the volume fraction of dispersed particles, r is the particle radius, and γ is the energy of the pinned grain boundary. GB motion ceases when an equilibrium matrix grain size is reached [91]:

$$D = \frac{4r}{3f} \tag{1.23}$$

Although this model has been derived assuming the second-phase particles as spherical, of equal size and of random distribution (i.e., located both at boundaries and within grains [93]), the pinning pressure is a complex function of the interface type and of the shape, size, interspacing and volume fraction of the dispersed particles [93,94].

1.2.4 Contamination by milling media

One drawback of high-energy milling for composite production is that the material tends to become contaminated by milling media debris, especially when hard phases, such as diamond, are involved. The impurity level increases with milling energy and time. Managing contamination requires establishing the best trade-off parameters for minimization of milling media wear and simultaneously obtain suitable grain refinement, composition/structure homogenization and particle dispersion. Other independent processing variables are able to influence contamination [8]; for instance it is desirable to employ milling media of composition similar to that of the milled materials and to select proper milling atmospheres to prevent oxidation. Stainless steel is the most common milling media material, although for very hard charges cemented carbides are preferred. Nevertheless it should be borne in mind that elements such as iron or nickel tend to catalyze chemical reactions and phase transformations [15], and may interfere with the milling outcome. In any case, contamination must be carefully monitored by energy dispersive spectroscopy (EDS) or higher sensitivity techniques such as particle induced X-ray emission (PIXE) spectroscopy.

1.2.5 Consolidation

Consolidation of mechanically synthesized materials is usually carried out by hot isostatic pressing (HIP) or by hot deformation [8,95]. However, these techniques tend to induce microstructural coarsening with a concomitant decrease in strength. A previous study involving Cu and G composites produced by conventional sintering resulted in poor

consolidation due to reduced wetting of graphite by copper [96]. Hot extrusion, on the other hand, demonstrated to be effective in producing fully dense materials [10,11,97,98] with the advantage of reinforcement alignment, which can convey thermal, electric and mechanical anisotropy to the consolidated materials.

The more recently developed spark plasma sintering (SPS) [99] has proven to be capable of minimizing coarsening and chemical reactions, moreover the technique is particularly useful to prevent carbide formation in the case of W, Mo, Ta and Hf. Promising results showed that grain growth is preserved with the SPS technique [10,11], although microstructural heterogeneity was detected, in contrast to the homogeneous microstructures obtained with hot extrusion [11,100].

Recovery phenomena and partial recrystallization occurring during thermomechanical consolidation and annealing treatments are likely to increase the thermal conductivity of the matrix. However, since strength tends to decrease with increasing grain size, fine tuning of thermomechanical and annealing treatments is usually required.

1.3 References

[1] T.S. Srivatsan, B.G. Ravi, A.S. Naruka, M. Petraroli, R. Kalyanaraman, T.S. Sudarshan, Mater. Design 23 (2002) 291–296.

[2] B.F. Decker, D. Harker, Trans. AIME 188 (1950) 887–890.

[3] M. Thuvander, M. Abraham, A. Cerezo, G.D.W. Smith, Mater. Sci. Tech. 17 (2001) 961–70.

[4] D.G. Morris, M. A. Morris, Acta Metall. Mater. 39 (1991) 1763–1770.

[5] V. Livramento, J.B. Correia, N. Shohoji, E. Ōsawa, Diamond Relat. Mater. 16 (2007) 202–204.

[6] K. Yoshida, H. Morigami Microelect. Reliab. 44 (2004) 303–308.

[7] T. Nickchi, M. Ghorbani, A. Alfantazi, Z. Farhat, Mater. Des. 32 (2011) 3548-3553.

[8] C. Suryanarayana, Prog. Mater. Sci. 46 (2001) 1–184.

[9] J.B. Correia, V. Livramento, N. Shohoji, E. Tresso, K. Yamamoto, T. Taguchi, K. Hanada, E. Ōsawa, Mater. Sci. Forum 587 (2008) 443–447.

[10] D. Nunes, J.B. Correia, P.A. Carvalho, N. Shohoji, H. Fernandes, C. Silva, L.C. Alves, K. Hanada, E. Ōsawa, Fusion Eng. Des. 86 (2011) 2589–2592.

[11] D. Nunes, V. Livramento, J.B. Correia, K. Hanada, P.A. Carvalho, R. Mateus, N. Shohoji, H. Fernandes, C. Silva, E. Alves, E. Ōsawa, Mater. Sci. Forum 636 (2010) 682–687.

[12] J.Y. Huang, H. Yasuda, H. Mori, Chem. Phys. Lett. 303 (1999) 130–134.

[13] X.H. Chen, H.S. Yang, G.T. Wu, M. Wang, F.M. Deng, X.B. Zhang, J.C. Peng, W.Z. Li, J. Crystal Growth 218 (2000) 57–61.

[14] Y. Chen, M.J. Conway, J.D. Fitz Gerald, J.S. Williams, L.T. Chadderton, Carbon 42 (2004) 1543–1548.

[15] K. Niwase, T. Tanaka, Y. Kakimoto, K.N. Ishihara, P.H. Shingu, Mater. Trans., Japan Inst. Metals 36 (1995) 282-288.

[16] J.Y. Huang, Acta Mater. 47 (1999) 1801–1808.

[17] T.D. Shen, W.Q. Ge, K.Y. Wang, M.X. Quan, J.T. Wang, W.D. Wei, C.C. Koch, Nanostructured Mater. 7 (1996) 393–399.

[18] K.P. So, H. Lee, D.L. Duong, T.H. Kim, S.C. Lim, K.H. An, Y.H. Lee, Acta Mater. 59 (2011) 3313–3320.

[19] Y.B. Li, B.Q. Wei, J. Liang, Q. Yu, D.H. Wu, Carbon 37 (1999) 493–497.

[20] Z. Qiao, J. Li, N. Zhao, C. Shi, P. Nash, Scripta Mater. 54 (2006) 225–229.

[21] C.H. Xu, C.Z. Wang, C.T. Chan, K.M. Ho, Phys. Rev. B43 (1991) 5024–5027.

[22] F.C. Nix, D. MacNair, Phys. Rev. 60 (1941) 597–605.

[23] A.V. Gubarevich, S. Usuba, Y. Kakudate, A. Tanaka, O. Odawara, Diamond Relat. Mater. 14 (2005) 1549–1555.

[24] V.L. Kuznetsov, I.L. Zilberberg, Y.V. Butenko, A.L. Chuvilin, B. Segall, J. Appl. Phys. 86 (1999) 863–870.

[25] E.D. Obraztsova, M. Fujii, S. Hayashi, V.L. Kuznetsov, Y.V. Butenko, A.L. Chuvilin, Carbon 36 (1998) 821–826.

[26] S. Tomita, A. Burian, J.C. Dore, D. LeBolloch, M. Fujii, S. Hayashi, Carbon 40 (2002) 1469–1474.

[27] V.L. Kuznetsov, Y.V. Butenko, Synthesis, Properties and Applications of Ultrananocrystalline Diamond NATO Science Series 192 (2005) 199–216.

[28] S. Das, S.V. Prasad, Wear 133 (1989) 173–187.

[29] F.F.O. Orumwense, B.A. Okorie, E.O. Okeakpu , E.N. Obiora , L.I.Onyeji, Powder Metall. 44 (2001) 62–66.

[30] K. Niwase, T. Tanaka, Y. Kakimoto, K.N. Ishihara, P.H. Shingu, Mater. Trans., Japan Inst. Metals 36 (1995) 282–288.

[31] B. Movahedi, M.H. Enayati, C.C. Wong, Mater. Sci. Eng. B 172 (2010) 50–54.

[32] H. Huang, P.G. McCormick, J. Alloys Compd. 256 (1997) 258–262.

[33] J.S.C. Jang, C.C. Koch. J. Mater. Res. 5 (1990) 498–510.

[34] S. Bhattacharyya, S.J. Henley, E. Mendoza, L.G. Rojas, J. Allam, S.R.P. Silva, Nature Mater. 5 (2006) 19–22.

[35] S.R.P. Silva, Properties of Amorphous Carbon, INSPEC Publication IEE, London, 2003.

[36] J.R. Davis, ASM International Handbook Committee, Nickel, cobalt, and their alloys, ASM International, 2000.

[37] B. Ghosh, H. Dutta, S.K. Pradhan, J. Alloys Compd. 479 (2009) 193–200.

[38] G.L. Caër, E.B. Grosse, A. Pianelli, E. Bouzy, P. Matteazzi, J. Mater. Sci. 25 (1990) 4726–4731.

[39] F.A. Khalid, O. Beffort, U.E. Klotz, B.A. Keller, P. Gasser, Diamond Relat. Mater. 13 (2004) 393–400.

[40] L. Wang, Y. Gao, H. Liu, Q. Xue, T. Xu, Surf. Coatings Techn. 191 (2005) 1–6.

[41] A. Kumar, M. Kaur, R. Kumar, P.R. Sengupta, V. Raman, G. Bhatia, K.N. Sood, J. Mater. Sci. 45 (2010) 1393–1400.

[42] Th. Schubert, B. Trindade, T. Weißgärber, B. Kieback, Mater. Sci. Eng. A 475 (2008) 39–44.

[43] P. Appendino, M. Ferraris, V. Casalegno, M. Salvo, M. Merola, M. Grattarola, J. Nuclear Mater. 348 (2006) 102–107.

[44] T. Schubert, Ł. Ciupinski, W. Zielinski, A. Michalski, T. Weißgärber and B. Kieback, Scripta Mater. 58 (2008) 263–266.

[45] E. Lassner, W.D. Schubert, Tungsten: properties, chemistry, technology of the element alloys and chemical compounds, Springer, 1999.

[46] M. Übeyli, S. Yalçin, J. Fusion Energy 25 (2006) 197–205.

[47] R. Andreani, M. Gasparotto, Fusion Eng. Des. 61–62 (2002) 27–36.

[48] H. Kurishita, S. Kobayashi, K. Nakai, T. Ogawa, A. Hasegawa, K. Abe, H. Arakawa, S. Matsuo, T. Takida, K. Takebe, M. Kawai, N. Yoshida, J. Nuclear Mater. 377 (2008) 34–40.

[49] M.R. Gilbert, J-Ch. Sublet, Nucl. Fusion 51 (2011) 043005/1–13

[50] G. Wang, S.J. Campbell, A. Calka, W.A. Kaczmarek, J. Mater. Sci. 32 (1997) 1461–1467.

[51] V. Livramento, D. Nunes, J.B. Correia, P.A. Carvalho, U. Mardolcar, R. Mateus, K. Hanada, N. Shohoji, H. Fernandes, C. Silva, E. Alves, J. Nuclear Mater. 416 (2011) 45–48.

[52] F.C. Campbell, Elements of metallurgy and engineering alloys, ASM International, 2008.

[53] R.V. Malyala, C.V. Rode, M. Arai, S.G. Hegde, R.V. Chaudhari, Appl. Catal. A: Gen. 193 (2000) 71–86.

[54] L. Benea, P. L. Bonora, A. Borello, S. Martelli, Wear 249 (2001) 995–1003.

[55] G.W. Meetham, The development of gas turbine materials, Applied Science Publishers Ltd, London, 1981.

[56] R. Vilar, E.C. Santos, P.N. Ferreira, N. Franco, R.C. da Silva, Acta Mater. 57 (2009) 5292–5302.

[57] D. Furrer, H. Fecht, JOM Journal of the Minerals, Metals and Materials Society 1 (1999) 14–17.

[58] R. Anton, Carbon 46 (2008) 656–662.

[59] Y. Chen, J.F. Gerald, L.T. Chadderton, L. Chaffron, Appl. Phys. Lett. 74 (1999) 2782–2784.

[60] B. Bokhonov, M. Korchagin, J. Alloys Compd. 333 (2002) 308–320.

[61] J. B. Correia, H.A. Davies, C.M. Sellars, Acta mater. 45 (1997) 177–190.
[62] M. Mabuchi, K. Higashi, Acta Mater. 44 (1996) 4611–4618.
[63] W.J. Kim, I.B. Park, S.H. Han, Scripta Mater. 66 (2012) 590–593
[64] D. Chandrasekaran, Grain Size and Solid Solution Strengthening in Metals, dissertation of Royal Institute of Technology, 2003.
[65] R.L. Fleischer, Acta Metall. 11 (1963) 203–209.
[66] R.L. Fleischer, W.R. Hibbard Jr., Proceedings of the Conference on Relation of Structure to Mechanical Properties of Metals, National Physical Laboratory, Her Majesty's Stationery Office, Teddington, Middlesex, UK, London, 1963.
[67] U.F. Kocks, A.S. Argon, M.F. Ashby, Thermodynamics and Kinetics of Slip. Progress in Materials Science, Vol. 19, Pergamon Press, Oxford, 1975.
[68] E.O. Hall, Proc. Phys. Soc. B64 (1951) 747–753.
[69] N.J. Petch, J. Iron Steel Inst. 174 (1953) 25–28.
[70] D. Tabor, The Hardness of Metals, Oxford University Press, New York, 1951.
[71] E.O. Hall, Nature 173 (1954) 948–949.
[72] M. Zhao, J.C. Li, Q. Jiang, J. Alloys Compd. 361 (2003) 160–164.
[73] P.G. Sanders, J.A. Eastman, J.R. Weertman, Acta Mater. 45 (1997) 4019–4025.
[74] M.A. Meyers, A. Mishra, D.J. Benson, Progress in Mater. Sci. 51 (2006) 427–556.
[75] A. M. El-Sherik, U. Erb, G. Palumbo, K.T. Aust, Scripta Metall. Mater. 27 (1992) 1185–1188.
[76] H.S. Kim, Scripta Mater. 39 (1998) 1057–1061.
[77] C.A. Schuh, T.G. Nieh, T. Yamasaki, Scripta Mater. 46 (2002) 735–740.
[78] H.H. Fu, D.J. Benson, M.A. Meyers, Acta Mater. 49 (2001) 2567–2582.
[79] E. Orowan, Symposium on Internal Stresses in Metals and Alloys, Institute of Metals, London, 1948, p. 451.
[80] M.F. Ashby, Proc. Second Bolton Landing Conference on Oxide Dispersion Strengthening, Gordon and Breach, New York, 1968, p. 143.
[81] M.F. Ashby, Acta Metall. Mater. 14 (1966) 679–681.
[82] A.J.E. Foreman, Acta Metall. 3 (1955) 322–330.
[83] N. Hansen, Metall. Trans. A 16 (1985) 2167–2190.

[84] S. Queyreau, G.Monnet, B. Devincre, Acta Mater. 58 (2010) 5586–5595.
[85] A.J. Ardell, Metall. Trans. A 16 (1985) 2131–2165.
[86] J.B. Correia, M.T. Marques, P.A. Carvalho, R. Vilar, J. Alloys Compd. 434–435 (2007) 301–303.
[87] N. Maruyama, G.D.W. Smith, Nippon Steel Technical Report 91 (2005) 34–37.
[88] J.W. Cahn, Acta metall. 10 (1962) 789–798.
[89] H.S. Zurob, Y. Brechet, G. Purdy, Acta mater. 49 (2001) 4183–4190.
[90] E. Rabkin, Scripta Mater. 39 (1998) 1631–1637.
[91] C. Zener, communicated by C.S. Smith, Trans. AIME 175 (1948) 15–51.
[92] E. Nes, N. Ryum, O. Hunderi, Acta Metall. 33 (1985) 11–22.
[93] Y. Xu, A. Zangvil, A. Kerberb, J. European Ceram. Soc. 17 (1997) 921–928.
[94] B.N. Kim, T. Kishi, Acta Mater. 47 (1999) 2293–2301.
[95] I.S. Polkin, A.B. Borzov, Adv. Perf. Mater. 2 (1995) 99–109.
[96] A. Yeoh, C. Persard, Z. Eliezer, Scripta Mater. 37 (1997) 271–277.
[97] K. Hanada, K. Yamamoto, T. Taguchi, E. Ōsawa, M. Inakuma, V. Livramento, J.B. Correia, N. Shohoji, Diamond Relat. Mater. 16 (2007) 2054–2057.
[98] J.B. Correia, M.T. Marques, M.M. Oliveira, P. Matteazzi, Mater. Sci. Forum 360 (2001) 241–246.
[99] M. Omori, Mater. Sci. Eng. A 287 (2000) 183–188.
[100] J.B. Correia,V. Livramento, N. Shohoji, E. Tresso, K.Yamamoto, T.Taguchi, K.Hanada, E.Ōsawa, Materi. Sci. Forum 587-588 (2008) 443–447.

Chapter 2

Chapter 2 – Experimental

2.1 Methods and working principals

2.1.1 Ball milling

Ball milling is a powder metallurgy technique that allows producing a variety of materials, such as metal alloys and composites, starting from elemental or compound powders [1]. The technique was developed by John Benjamin and his colleagues at the Paul D. Merica Research Laboratory of the International Nickel Company (INCO) around 1966 [2,3]. It resulted from long research on the production of a nickel-base superalloy for gas turbine applications. The process, as developed by Benjamin, involved the use of hard balls in a rotating container and was referred to as 'Milling/Mixing'. Yet Ewan C. MacQueen, a patent attorney for INCO, coined the terms mechanical alloying to describe the process in the first patent application, which have come to stay in the literature regarding alloy production by ball milling.

Subsequently, the formation of amorphous phases by milling an Y-Co intermetallic compound or blended Ni-Nb powder mixtures attested for its potential as a non-equilibrium processing technique [4,5]. Additionally, it has been recognized that powder mixtures can be mechanically activated to induce chemical reactions at temperatures much lower than normally required. The terms 'mechanical synthesis' is preferably employed in the latter case, while 'ball milling' continues to be used as a generic designation. During the past three decades much research has been carried out in order to improve the technique and understand its fundamentals [1,6-10].

2.1.1.1 Ball milling working principles and mechanisms

During ball milling the powder particles in the container are repeatedly deformed, cold-welded, fractured and re-welded. Nevertheless, the energy imparted is mostly lost in the form of heat and only a minor amount is spent in the elastic and plastic deformation of the powder particles [1].

Whenever two balls collide, a number of powder particles are trapped between them [1] (Figure 2.1). At early stages the milled powders have a characteristic layered structure consisting of various combinations of the initial elements/compounds. New surfaces are created and any soft particles present tend to weld together, originating a broad range of particle sizes, in some cases three times larger than the original ones [1]. Upon continued deformation, the tendency to fracture predominates over cold welding; the particles become work hardened and tend to fracture by a fatigue mechanism and/or by fragmentation of fragile flakes. Fragments generated by these mechanisms may continue to reduce in size in the absence of strong agglomerating forces.

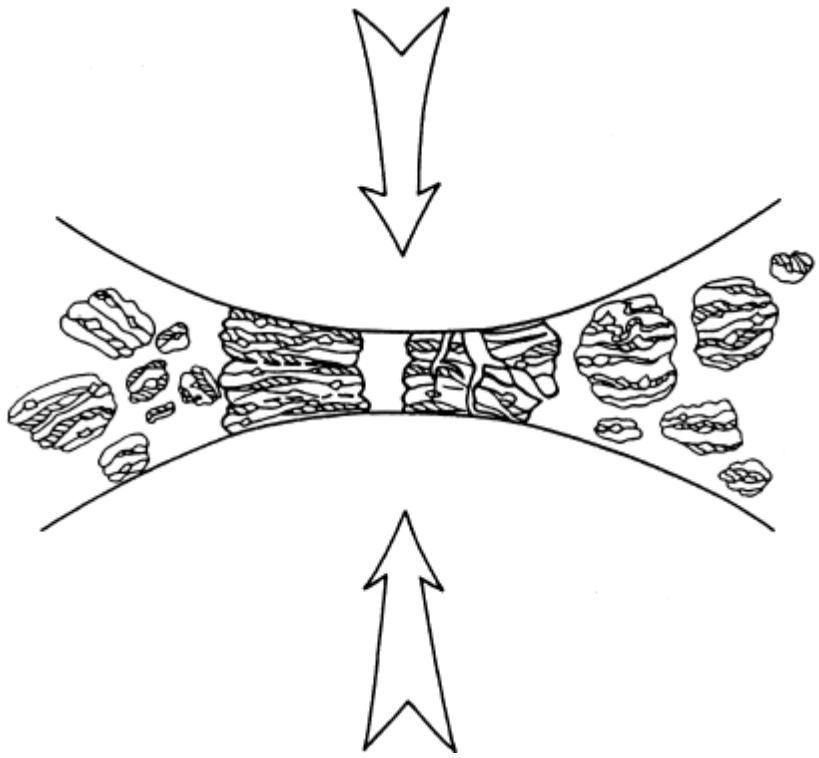

Figure 2.1. Example of ball-powder collisions during milling [1].

For longer milling times, due to the continued impact of the milling balls, the particle internal structure is steadily refined, although the powder particle size remains essentially constant. A steady state is eventually reached with a balance between the rates of welding and fracture. At this stage each particle presents the initial elemental/compound proportion and the particle size distribution is narrow, as larger particles than the average are reduced in size at the same rate that smaller fragments grow through agglomeration. The heavy deformation introduced into the particles

saturates hardness. This is manifested by the presence of a variety of crystal defects such as dislocations, vacancies, stacking faults, and an increased number of grain boundaries. The defective and refined microstructure enhances diffusivity, which in turn assists alloy formation.

The milling time required to develop a given microstructure is a function of the characteristics of the pristine materials, and of the equipment and parameters employed. Nevertheless, in most cases, the rate of refinement of the internal structure varies roughly with the logarithm of the milling time and the grain size of the initial particles is relatively irrelevant as in a few minutes to an hour, the crystallite (or grain) size is refined to the nanometer scale (Figure 2.2).

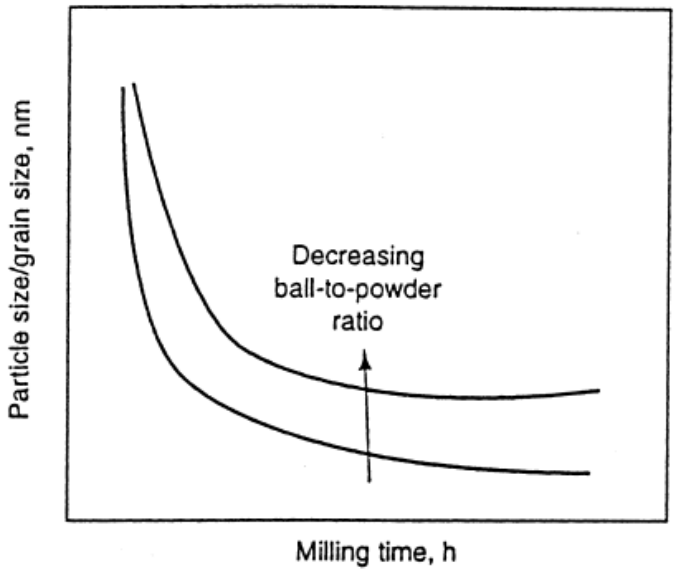

Figure 2.2. Refinement of particle and grain sizes with milling time [1].

Benjamin [11] suggested that it is necessary to have at least 15 vol.% of a ductile component to achieve alloying, since cold welding is difficult with brittle particles. In fact, ductile-ductile system are considered ideal, however, alloying has been reported in brittle-brittle component systems such as Si-Ge [12]. Indeed brittle components are continuously fragmented during milling and, at very small scales, tend to behave in a ductile fashion. In ductile-brittle systems, the ductile particles are flattened by the ball-powder-ball collisions early during milling, while the brittle particles get fragmented/comminuted. These fragmented brittle particles, if insoluble, tend to become occluded by the ductile constituents and uniformly dispersed in the ductile matrix with

continued milling. On the other hand, if the brittle phase is soluble, alloying occurs and chemical homogeneity may be reached [1].

2.1.1.2 Ball milling processing variables

Ball milling is a complex process, involving a number of variables whose effects are not completely independent, namely:

- milling device;
- milling media (container and balls);
- contamination;
- milling energy;
- milling temperature;
- milling time;

Milling device

Diverse types of mills can be used with main differences in rotation pattern, capacity, milling efficiency and additional arrangements for cooling or heating.

In the present study ball milling has been performed with a planetary mill (Figure 2.3 (a)) in which a few hundred grams of powder could be milled at a time. The planetary mill owes its name to the planet-like movement of its milling containers, which are arranged on a rotating support disk with a special drive mechanism that rotates them around their own axes. The centrifugal forces produced by the containers rotating around their own axes and by the rotating support disk, act on the material being processed and on the milling balls. Since the two rotational movements occur in opposite directions, their superimposition gives rise to the so-called Coriolis forces: the combined centrifugal forces lift off the milling balls across the inner chamber of the container and make them collide against the opposing inner wall of the container (Figure 2.3 (b)). The ball trajectory depends on the relative value of the ball speed *vs* container rotation and on the relative size of the support disk *vs* container [13],

rendering the collision either tangential (frictional) or normal (impact) to the container internal wall. The fine interplay between frictional and impact forces in planetary mills can result in a high degree of microstructural refinement.

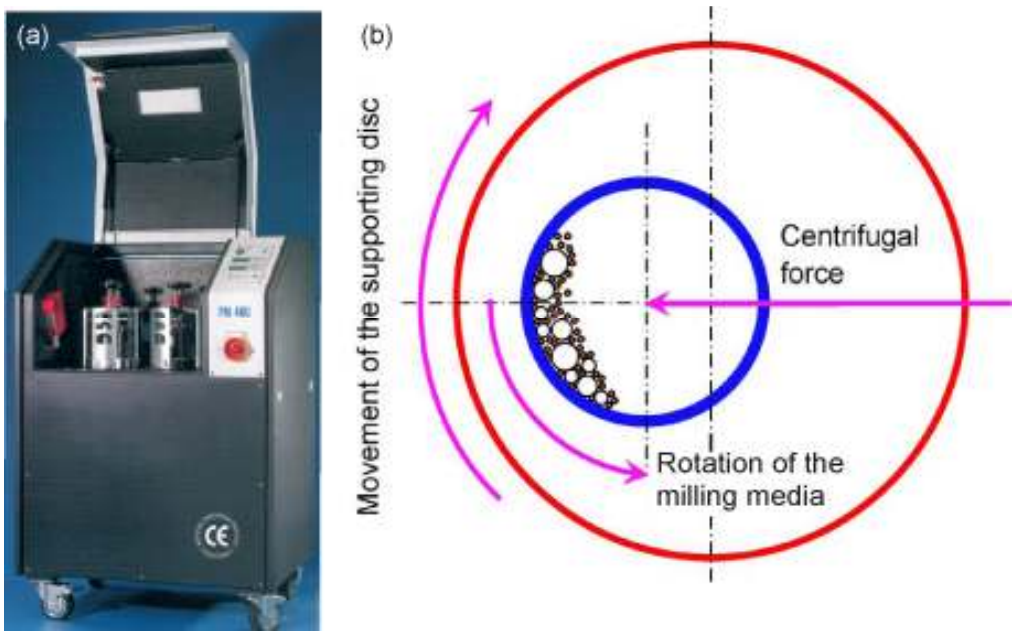

Figure2.3. (a) Retsch planetary ball mill [14]. (b) Working principle of a planetary ball mill [15].

Milling media

The material used for the milling container must be suitably selected due to the high-energy impact of the milling balls on its inner walls. In effect, a significant part of the milling media material is normally dislodged and incorporated in the milled material, modifying its chemistry. In order to minimize contamination by milling media, it is desirable to have the container and balls made of the same material as the processing powder. Hardened steel, tool steel, hardened chromium steel, tempered steel, stainless steel, bearing steel, WC-Co and ceramic materials are the most common types of materials used for the milling container. Except for the ceramics, the same type of materials is used for the milling balls.

The size and density of the balls influence the milling efficiency through the impact force generated. In fact, a sole variation in ball size has been shown to result in either a solid solution or a mixture of two phases [1]. The weight ratio between the balls

and the powder must also be considered: higher ball weight proportions increase the number of collisions per unit time and, consequently, the energy transferred to the powder particles, reducing the processing time. Furthermore, the extent to which the container is filled must also be taken into account, and since balls and powder should be allowed to move freely about 50% of container space is usually left empty [1].

Contamination

The nature and amount of impurities that contaminate the milled powder are a chief concern. The small size of the powder particles, the availability of large specific areas, and the formation of new surfaces during milling, all potentiate the incorporation of extraneous material, and contamination of the powders is an inherent drawback of the technique.

Contamination can be mainly traced to (i) chemical impurities in the starting powders; (ii) milling atmosphere; and (iii) incorporation of milling media debris. Contamination originating from the starting powders can be either substitutional or interstitial, while contamination from milling atmosphere tends to be interstitial and contamination from milling media is essentially substitutional.

The presence of interstitial impurities, such as oxygen and nitrogen, is deleterious to reactive metals and can be minimized if the containers are either evacuated or filled with an inert gas, such as high-purity argon. Nonetheless, the absorbed inert gas is an important contamination source [1,16].

Milling media debris can originate inclusions in the milled powder [1,17]. As previously mentioned, the powder particles get trapped between the balls, undergo severe plastic deformation and new surfaces are created due to fracture of the powder particles. Additionally, collisions occur between the balls and the container, and also amongst the milling balls. All these effects cause wear and tear of the milling media and result in the incorporation of impurities in the powder. The magnitude of contamination originating from the milling media depends on milling time, milling energy, and on the difference in hardness between the powder and the milling media. Whenever possible containers and milling balls should be harder/stronger than the processing powder [1]. In what concerns the present work, nanoscale diamond has been reported to possess self-lubrication properties [18]. As a result, in spite of the extreme hardness of diamond,

minor contamination is expected with nD particles, contrarily to the case of micro-sized diamond.

Milling energy

The faster the mill rotates the higher is the energy transferred to the milled powder. However, above a critical speed, the balls become immobilized against the inner walls of the container, hindering impaction. The operating speed should hence be just below this critical value for maximum collision energy. For a rotation tumbler mill Rose and Sullivan [19] showed that the critical rotation speed N_c, is given by:

$$N_c = \frac{1}{2\pi}\sqrt{\frac{2g}{\mathrm{d}-\mathrm{r}}} \tag{2.1}$$

where g is the gravitational acceleration, d is the inner diameter of the container and r is the radius of balls. Milling energy is directly responsible for reaction progress and phase transformations [20], moreover a minimum milling energy threshold is required for amorphization and carbide formation [20,21].

Milling temperature

Two major phenomena can contribute to increase the temperature during milling: friction during collision and localized plastic deformation. Schwarz and Kochi [22] proposed a model in which the temperature rise due to localized deformation is given by:

$$\Delta\mathrm{T} = \frac{\phi}{2}\sqrt{\frac{\Delta t}{\pi k_0 \rho_p c_p}} \tag{2.2}$$

where ΔT is the increase in milling temperature, ϕ is the dissipated energy flux given as $\sigma\nu$, where σ is the normal stress due to a head-on collision and ν is relative velocity of the ball before impact, Δt is the stress state life, ρ_p is the density of the powder particles, k_0 is the thermal conductivity of the particles and c_p is the specific heat of the powders.

At high milling energy, temperatures of ~400 K can be reached locally [1]. Nevertheless, the global temperature is relatively low since heat can be rapidly dissipated through the large mass of the container, balls and powder particles [23]. Higher temperatures are advantageous when diffusion is required to promote homogenization and/or alloying in the powders, but not when the goal is to prevent the reaction between components as in composites where no in-situ reactions are desired..

Milling time

Steady state is eventually reached for long milling times, where a balance between fracturing and cold welding processes occurs with a concomitant saturation of the milled material properties. However, long milling times increase the level of contamination by milling media resulting in the presence of undesirable phases [1]. The milling time required to homogenize the structure while minimizing contamination varies with the type of mill, milling energy, ball-to-powder weight ratio and temperature of milling, and is usually established through systematic post-processing investigation.

2.1.2 Consolidation

2.1.2.1 Spark Plasma Sintering

SPS is a recently developed technique that makes possible sintering and sinter-bonding at low temperatures during short periods. The process relies on charging the gaps between the powder particles and applying, locally and momentarily, spark plasma. The applications range from general sintering of metals and ceramics [24,25], including consolidation of composites [17,26,27], to consolidation with prevention of crystal growth [28] and chemical reactions [27].

The SPS instrument comprehends the following components: vertical single-axis pressurization system, water-cooled chamber, atmosphere controls, vacuum exhaust unit, DC pulse generator and controller (Figure 2.4). The powder materials are stacked between the die and punch on the sintering stage and held between the electrodes. The

repeated application of an ON-OFF DC pulse results in spark discharges between the powder particles and in Joule effect heating, producing efficient sintering with low power consumption [29]. Through pulse application the local temperature instantly rises to 1500~3000 K [29] and under pressure the process finishes within a few minutes.

The high temperature at the gaps causes melting and vaporization at the surfaces, and constricted shapes or "necks" form between the particles. The necks progress during sintering and can result in 99% dense sintered material. Since the temperature increase is concentrated at the particles surface, the internal structure and grain growth can be preserved/controlled [29].

SPS offer many advantages over hot press sintering, hot isostatic pressing or pressureless sintering, that include concentration of the sintering energy at the intergranular regions and easy control of the sintering energy, as well as well high sintering speed, reproducibility, safety and reliability [29]. The main drawback of the technique is that the sintered body will have a heterogeneous structure owing to the very different thermal cycles experience by the powder surface and its interior.

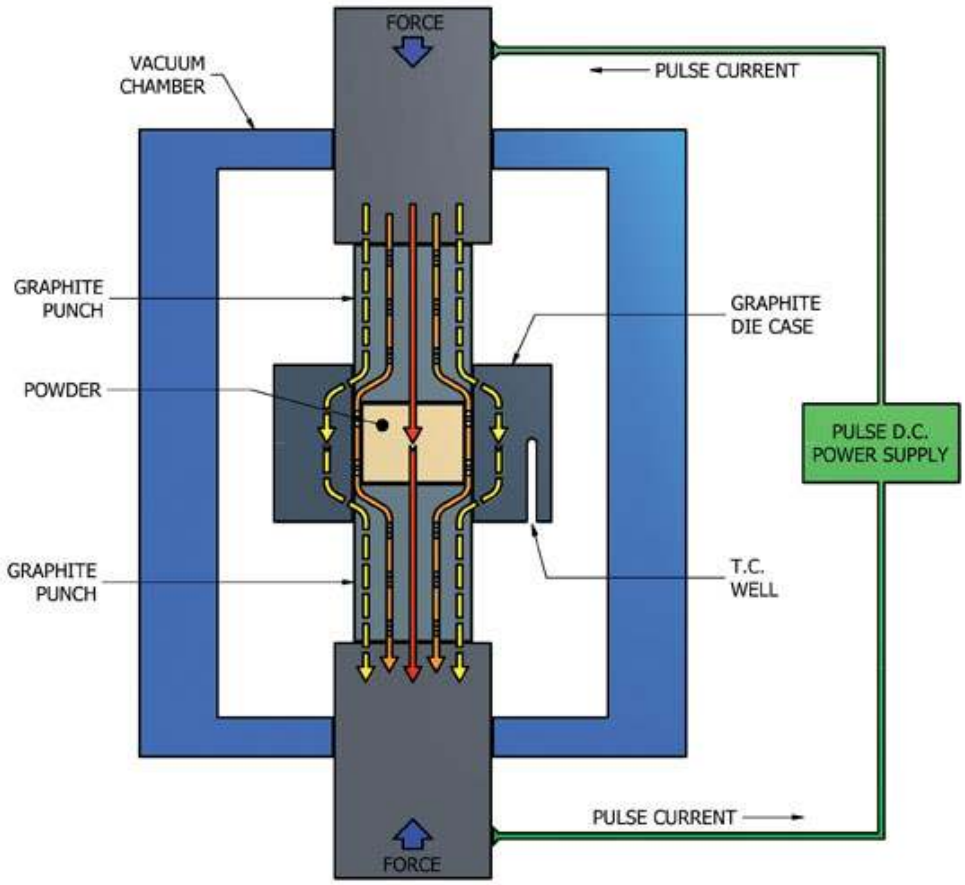

Figure 2.4. Spark plasma sintering diagram [30].

2.1.2.2 Hot extrusion

Extrusion is defined as the operation of producing rods, tubes or various complex sections by forcing with a ram a billet of metal through a suitable die (Figure 2.5). In hot extrusion, the billet is heated to reduce the yield strength of the metal [31].

A rapid rise in pressure occurs during the initial ram travel due to the compressive stress required by the billet to fill the extrusion container. The metal begins to flow through the die at the maximum pressure, the breakthrough pressure. As the billet extrudes through the die, the pressure required to maintain flow is progressively reduced due to the lower energy required to overcome the static friction with the decreasing length of the billet. The chief parameters of hot extrusion are: extrusion ratio, working temperature, pressure, rate of deformation and frictional/lubrication conditions.

The extrusion ratio, the ratio of the initial to the final cross-sectional areas, is limited by the available pressure and temperature of the extrusion process. Hot extrusion is performed at fairly high temperatures, approximately 50 to 75 % of the melting temperature of the metal to be processed. The pressures employed can range from 35 to 700 MPa [32]. The ram speed determines the rate of deformation and depends on the pressure and temperature. Since the process has a detrimental effect on the die life, as well as on other components of the extruder, proper lubrication is required. Lubricants must exhibit low shear strength and stability at high temperature: oil, graphite and MoS_2 are employed at moderate temperatures, while glass powder is used at high temperatures.

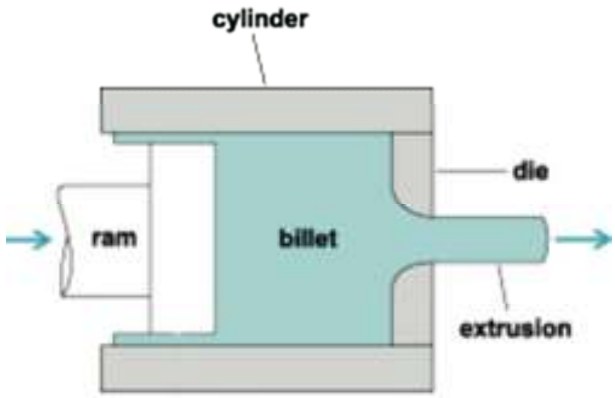

Figure 2.5. Hot (direct) extrusion diagram [33].31

2.1.3 Materials characterization

2.1.3.1 X-ray diffraction

2.1.3.1.1 Geometry of diffraction

Max von Laue showed that X-rays have wavelengths similar to the interatomic distances in crystals, which may be considered built up of scattering centres acting as 3-D diffraction gratings. If radiation of wavelength λ is incident at an angle α_o on a row of atoms separated by *a* along the *x*-axis, the path difference of rays scattering from points A and D is just AB-CD (see Figure 2.6).

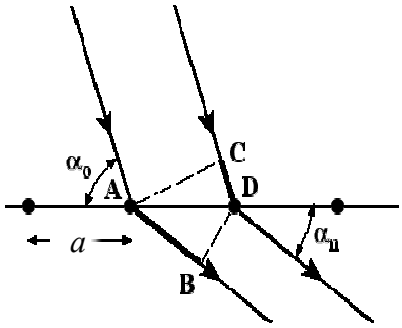

Figure 2.6. (a) Diffraction along the *x*-axis. The incident and diffracted beams are at α_0 and α_n to the row of atoms. The path difference between the diffracted beams is AB – CD [34].

If the incoming rays are in phase, the path difference must be some integer multiple of the wavelength for constructive interference to occur, leading to the first Laue equation.

$$(AB - CD) = (cos\alpha_n - cos\alpha_0).a = h\lambda \qquad (2.3)$$

where α_n and α_o are the angles between, respectively, the diffracted and incident beams and the *x*-axis and *h* is an integer. This result is valid for any scattered ray that makes an angle α_n to the *x*-axis and thus the Laue condition is consistent with a cone of scattered rays centered on the *x*-axis. Since $\boldsymbol{a}.\mathbf{S} = a.(cos\alpha_n)$ and $\boldsymbol{a}.\mathbf{S_0} = a.(cos\alpha_0)$, Equation 2.3 can be represented in vector notation as:

$$\boldsymbol{a}.(\mathbf{S}-\mathbf{S_0}) = h\,\lambda \qquad (2.4)$$

where the distance a becomes a unit cell vector $\boldsymbol{a}$, the unit vector parallel to the incoming ray is $\mathbf{S_0}$, and the unit vector parallel to the scattered ray is $\mathbf{S}$ (see Figure 2.6):

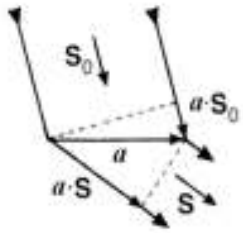

Figure 2.7. The incident and diffracted beam directions and the path difference between the diffracted beams expressed in vector notation [34].

The second Laue equation is written considering another row of scattering centers along an y-axis at a given angle to the x-axis with a repeat distance b (Eq. 2.5). The incident rays will make angle β_0 to this row and the scattered rays β_n. This equation must result in a k integer multiple of the wavelength for constructive interference to occur:

$$(AB - CD) = (cos\beta_n - cos\beta_0).b = k\lambda \qquad (2.5)$$

The solution to this second equation also forms a cone except this time about y. The notable idea of Laue was that this equation must have a simultaneous solution with the equation written for the x-axis. The simultaneous solution to these two equations can be viewed as the intersection of the two cones originating at a common apex (which intersect along two lines, see Figure 2.8 (a)).

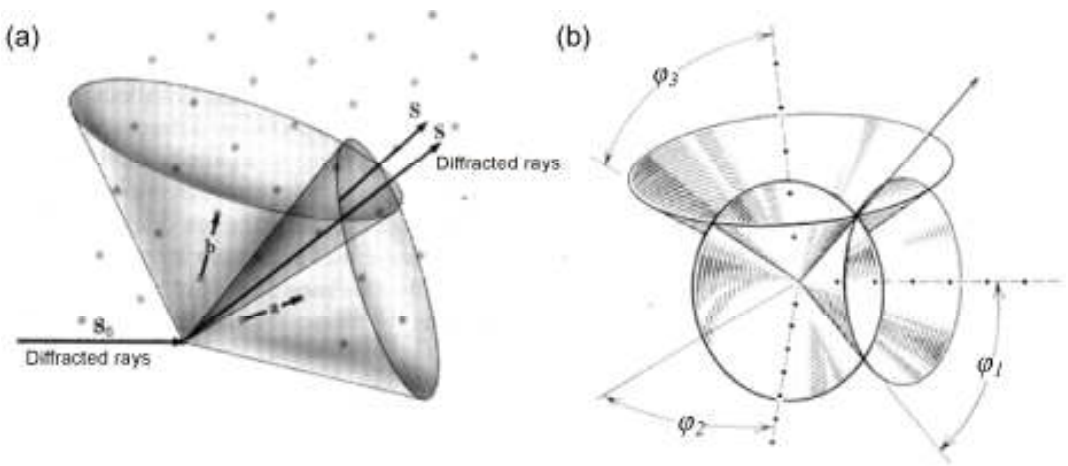

Figure 2.8. (a) Representation of the intersection of the two cones originating at a common apex [34]. (b) Diffraction cones from three non-coplanar rows of scattering atoms in common line [35].

Adding scattering centers along a z-axis, to form a 3-dimensional lattice, gives by analogy the third Laue equation:

$$(AB - CD) = (cos\gamma_n - cos\gamma_0).c = l\lambda \qquad (2.6)$$

where γ_n and γ_0 are the angles, c is the interatomic distance and l is the integer. This results in a set of equations with one simultaneous solution, i.e., the 3-dimensional solution will be a single vector lying at the intersection of three cones sharing a common apex (Figure 2.8 (b)). Considering a diffraction vector defined as $\mathbf{K} = (\mathbf{S} - \mathbf{S_0})/\lambda$, diffraction occurs when simultaneously:

$$\mathbf{K}.\boldsymbol{a} = h \qquad (2.7)$$

$$\mathbf{K}.\boldsymbol{b} = k \qquad (2.8)$$

$$\mathbf{K}.\boldsymbol{c} = l \qquad (2.9)$$

The solution to these equations is:

$$\mathbf{K}=h.\boldsymbol{a}^*+ k.\boldsymbol{b}^*+ l\,.\,\boldsymbol{c}^* \qquad (2.10)$$

where h, k and l are the Miller indices of an (hkl) plane in real space and $\boldsymbol{a}^*$, $\boldsymbol{b}^*$ and $\boldsymbol{c}^*$ are a new set of vectors which are related to $\boldsymbol{a}$, $\boldsymbol{b}$ and $\boldsymbol{c}$ according to:

$$\boldsymbol{a}^*.\boldsymbol{a} = 1 \quad \boldsymbol{a}^*.\boldsymbol{b} = 0 \quad \boldsymbol{a}^*.\boldsymbol{c} = 0$$

$$\boldsymbol{b}^*.\boldsymbol{a} = 0 \quad \boldsymbol{b}^*.\boldsymbol{b} = 1 \quad \boldsymbol{b}^*.\boldsymbol{c} = 0$$

$$\boldsymbol{c}^*.\boldsymbol{a} = 0 \quad \boldsymbol{c}^*.\boldsymbol{b} = 0 \quad \boldsymbol{c}^*.\boldsymbol{c} = 1$$

Constructive interference occurs then when $\mathbf{K} = \mathbf{g}$, which defines a point in reciprocal lattice.

Bragg confirmed that Laue's photographs resulted from diffraction, but interpreted the phenomenon by envisaging diffraction in terms of reflection from crystal planes (Figure 2.9) and by considering that constructive interference required that the path difference between waves, $2d_{hkl}\,sin\theta$, must equal a whole number of wavelengths:

$$n\lambda = 2d_{hkl}\,sin\theta \qquad (2.11)$$

Bragg's law provides then the condition for a plane wave to be diffracted by a family of lattice planes, where n is an integer designated as order of diffraction, λ is the

wavelength of incident wave, d_{hkl} is the spacing between the planes in the atomic lattice, and θ is the angle between the incident ray and the scattering planes. The idea of specular reflection is not physically correct, as the atoms in a real crystal act as individual scatterers. Nevertheless, Bragg's construction turns is geometrically valid and results in a simple relationship for the diffraction condition.

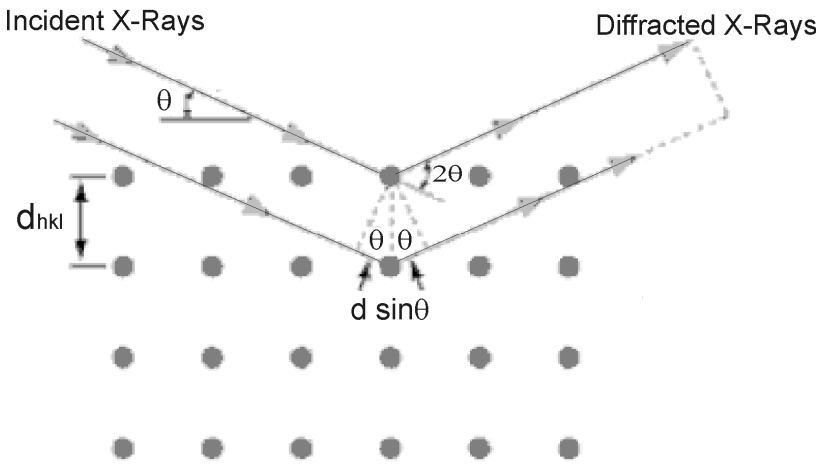

Figure 2.9. Geometry behind Bragg's diffraction [36].

Ewald proposed a geometrical construction for Bragg's equation which has been used ever since for interpreting diffraction patterns. The crystal is placed at the center of a reflection sphere with a radius of 1/λ (Figure 2.10), the origin of the reciprocal lattice is situated at **O**, the incident wave vector $\mathbf{S_0}$ is $\mathbf{C_rO}$, the diffracted wave vector **S** is $\mathbf{C_rP}$ and the angle between them is 2θ. **OP** is a reciprocal lattice vector **g** and has thus magnitude $1/d_{hkl}$. Since the incident and diffracted wave vectors have magnitude 1/λ, the condition **OP** = **g** corresponds to $2\sin\theta/\lambda = 1/d_{hkl}$, which is equivalent to Bragg's law for a first order diffraction (n=1). This means that the diffracted wave vector **S**, will satisfy the diffraction condition if $\mathbf{OP} = \mathbf{C_rP} - \mathbf{C_rO} = (\mathbf{S} - \mathbf{S_0})/\lambda$ is a reciprocal lattice vector **g**, that is if:

$$\mathbf{g} = (\mathrm{S} - \mathbf{S_0}) / \lambda = \mathbf{K} \qquad (2.12)$$

which is equivalent to Laue equations.

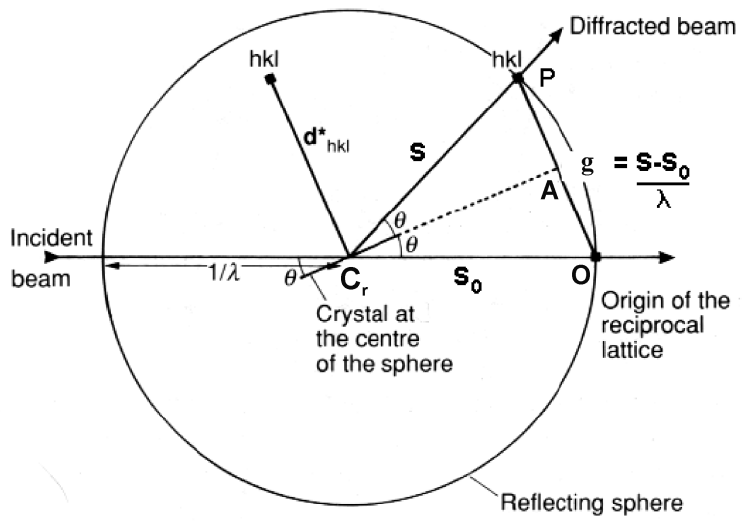

Figure 2.10. Ewald construction [34].

2.1.3.1.2 Powder X-ray diffraction

Powder X-ray diffraction is commonly employed in several types of research lines, namely identification of phases, determination of crystallite size and residual strains, precise lattice parameter determination and atomic structure refinement.

The series of reflections detected as a function of the 2θ angle are a unique fingerprint for any given crystalline structure. The *d*-spacing corresponding to each reflection can be then obtained by solving Bragg's law for the appropriate values of λ and θ, identifying the phases present. The reflection width is in turn related with the crystallite size and residual strains, and reflection shifts result from the presence of solutes.

A powder X-ray diffractometer comprises a source of X-rays, controls for the alignment of the beam, as well as the position and orientation of both the specimen and the X-ray detector, together with X-ray data collection and analysis systems.

2.1.3.1.3 X-ray source

The X-rays are generated in a cathode tube where through a thermoionic effect a tungsten filament (cathode) emits electrons that are accelerated toward a target (anode) by a potential difference. The high-energy electrons eject ground-state electrons from the atoms of the target material and refilling of these ground states induces X-ray

emission. When an electron from a K-shell is displaced, it leaves a vacancy, which destabilises the atom, and an electron from a higher-energy level will tend to occupy the vacancy. If the electron is provided by the L-shell, the transfer corresponds to the emission of a K_α photon with energy equal to the difference between the K and L shells. Such a transfer results also in a vacancy being created in the L-shell which in turn can be filled by an M-shell electron, with emission of a L_α photon. If the electron vacancy on the K shell would be filled by an M-shell electron, a K_β photon would be generated. Furthermore, since within each shells there are multiple levels of energy, a further designation, α_1, α_2 etc, is required (Figure 2.11). Emission of this radiation allows the atom to return to a more stable energy-state. The specific energy of the emitted radiation is *characteristic* of the atoms present in the target material (usually Cu, Fe, Mo and Cr). Photons generated by decelerating collisions are also produced, and result in a continuous distribution of energies and wavelengths in the spectrum emitted from the target, known as bremsstrahlung (deceleration) radiation. The X-rays emitted by the target atoms leave the cathode tube through thin windows, normally made of beryllium, and are subsequently filtered so that only K_α photons remain, and are directed toward the sample [37].

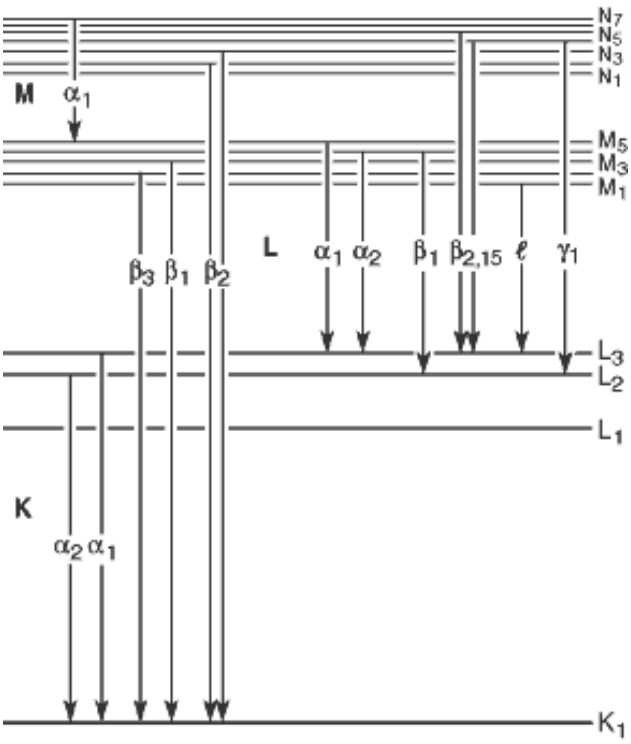

Figure 2.11. Transitions that give rise to the various X-ray lines [38].

2.1.3.1.4 Bragg-Brentano configuration

In a powder or polycrystalline diffractometer a divergent X-ray beam exits the source and hits the fine powder sample with random crystallographic orientation at different points on its surface (see Figure 2.12). After the diffraction process, the rays are refocused at the detector slit. The slits move on a circle centred on the sample. The angle between the incident and Bragg diffracted beams is equal to 2θ, whereas the sample is at θ to the incident X-ray beam. This is called the Bragg-Bretano geometry. The diffracted radiation is recorded by an X-ray detector mounted on the diffractometer goniometer stage and rotated about the sample.

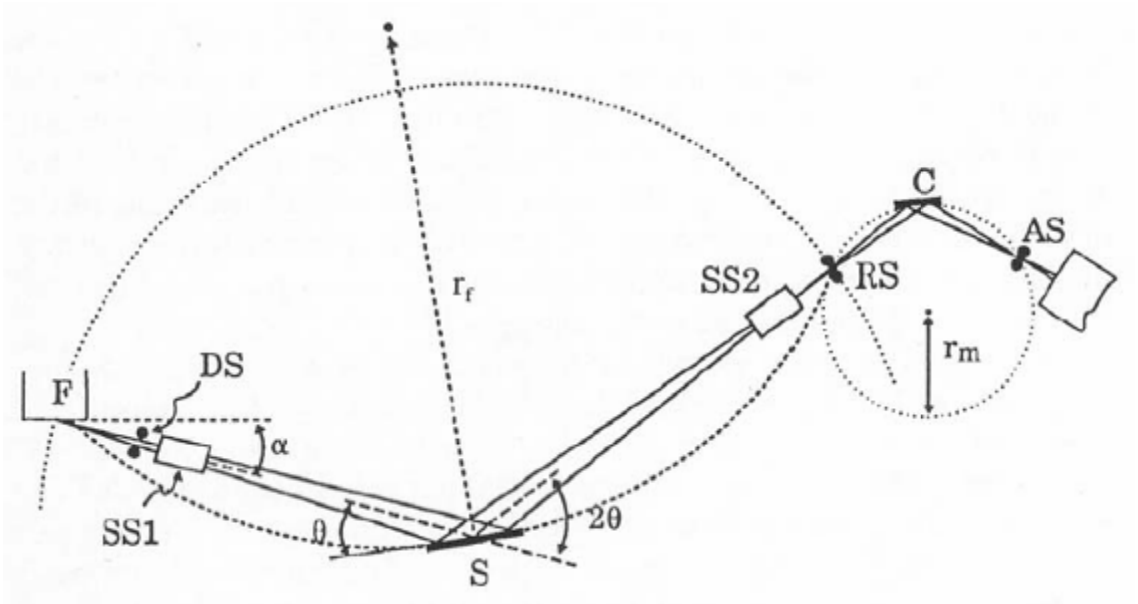

Figure 2.12. The Bragg-Brentano geometry where F is the X-ray source, DS is the divergence scatter slit, SS is the soller slit assembly (SS1 on "tube" side, SS2 on detector side). RS is the receiving slit, C is the monochromator crystal, r_m is the radius of the monochromator circle on which RS, C and AS (the detector slit) lie, r_f is the radius of the focusing circle. F, S and RS all fall on this circle. The angles are indicated [39].

2.1.3.1.5 Phase identification

X-ray diffraction is one of the most powerful tools for crystalline phase identification, performed by comparing the positions and intensities of the diffraction peaks against a library of phase information. Coexisting phases can be identified with a detection limit of ~1 wt.% for similar diffracting powers [40] and quantified from the relative integrated intensity of the peaks. Nevertheless, phases in considerable amounts

may be undetectable when expressive differences in atomic number obscure the peaks of lower average Z crystals. Furthermore, fine particles tend to have lower detection limits; for instance, it has been shown that while 2 wt.% Ti can be easily detected in Al-20wt%Ti mixtures when the particle size is in the 26-38 μm range, about 25 wt.% Ti is required if the particle size lies in 0.05-1.0 μm range [1].

In the current study the method has been employed to detect the presence of carbides and oxides in the metal-carbon nanocomposites produced by ball milling.

2.1.3.1.6. Crystallite size and strain determination

X-ray diffraction peaks are broadened due to (i) instrumental effects, (ii) reduced particle size, and (iii) lattice strain in the material. This means that crystallite size and lattice strain can be determined using peak broadening analysis through separation of their effects. In this analysis the crystallites are assumed to correspond to coherently diffracting domains, which and are not necessarily the same as grains [41].

In practice broadening (β) is assessed through the peak width at half the maximum intensity determined (β_m) by taking into account the calibrated instrumental broadening (β_i):

$$\beta=\beta_m-\beta_i \tag{2.13}$$

Crystallite refinement caused by ball milling leads to effective broadening of X-ray diffraction peaks. However, since the process introduces also considerable strain in the processed material the contribution of residual lattice elastic deformation to peak broadening may not be negligible. Scherrer equation and the Williamson-Hall method have been used to access the two contributions to the peak broadening observed in the X-ray diffractograms of the metal-carbon nanocomposites.

2.1.3.1.7. Scherrer equation (crystallite size)

Due to the less than infinite size of the crystal, the destructive interference conditions for angular deviations around Bragg's angle are more hardly met, with incoherent radiation contributing to the peak intensity. This broadening effect resulting from crystallite size is quantified by Scherrer equation.

Broadening of the diffracted beam from a crystal of finite extent can be derived considering a crystal with thickness D perpendicular to planes with a d_{hkl} interplanar distance (Figure 2.13 (a)) [34]. If there are m planes then $md_{hkl}=D$. Considering a beam incident on the whole crystal at the exact Bragg angle for the first order reflection, the path difference for the first two planes, labeled 0 and 1, is $\lambda=2d_{hkl}\sin\theta$; while for planes 0 and 2 the path difference is $2\lambda=4d_{hkl}\sin\theta$, and so on – so that constructive interference between all the planes occurs right through the crystal. If the beam is deviated a small angle $\Delta\theta$ from the exact Bragg angle (Figure 2.13 (b)), for planes 0 and 1 the path difference will be very be close to λ and there will still be constructive interference. However, for planes 0 and 2, 0 and 3, and following, the extra path difference will deviate increasingly from 2λ, 3λ, etc, with destructive interference occurring when the path difference is $\lambda/2$.

At the exact Bragg angle θ, the condition for destructive interference for the whole crystal is obtained similarly by pairing reflections from planes 0 and $(m/2)$, so that $(m/2)\lambda = (m/2)\, 2d_{hkl}\sin\theta$. The condition for destructive interference at angle $(\theta+\Delta\theta)$ is given by $(m/2)\lambda + \lambda/2 = (m/2)\, 2d_{hkl}\sin(\theta+\Delta\theta)$. This is also the condition for destructive interference between the next pair of planes 1 and $(m/2)+1$, and so on through the crystal. This equation represents hence the condition for destructive interference for the whole crystal and for the angular range $\Delta\theta$ (each side of the exact Bragg angle) of the reflected beam. Expanding the sine term and making the approximation $\cos\Delta\theta=1$ and $\sin\Delta\theta\sim\Delta\theta$ results in:

$$(m/2)\,\lambda + \lambda/2 = (m/2)\, 2d_{hkl}\sin\theta + (m/2)\, 2d_{hkl}\cos\theta\,\Delta\theta \qquad (2.14)$$

Cancelling the $(m/2)\,\lambda$ and $(m/2)\, 2d_{hkl}\sin\theta$ and replacing md_{hkl} by D, originates Scherrer equation:

$$2\Delta\theta = \frac{\lambda}{D\cos\theta} \text{ or } D = \frac{\lambda K}{\beta\cos\theta} \qquad (2.15)$$

where D is the crystallite size, λ is the wavelength of the X-radiation used, θ is the Bragg angle and K or Scherrer factor is a dimensionless constant that accounts for particle shapes and may range from 0.89 to 1.39. For a perfect two-dimensional lattice, where every point on the lattice emits a spherical wave, numerical calculations yield the lower bound of 0.89 for K [42], which has been used in this work. β is approximately equal to $2\Delta\theta$. Figure 2.14 (a) shows a diffracted beam (angle 2θ to the direct beam) which is broadened over an angular range $2\beta \sim 4\Delta\theta$.

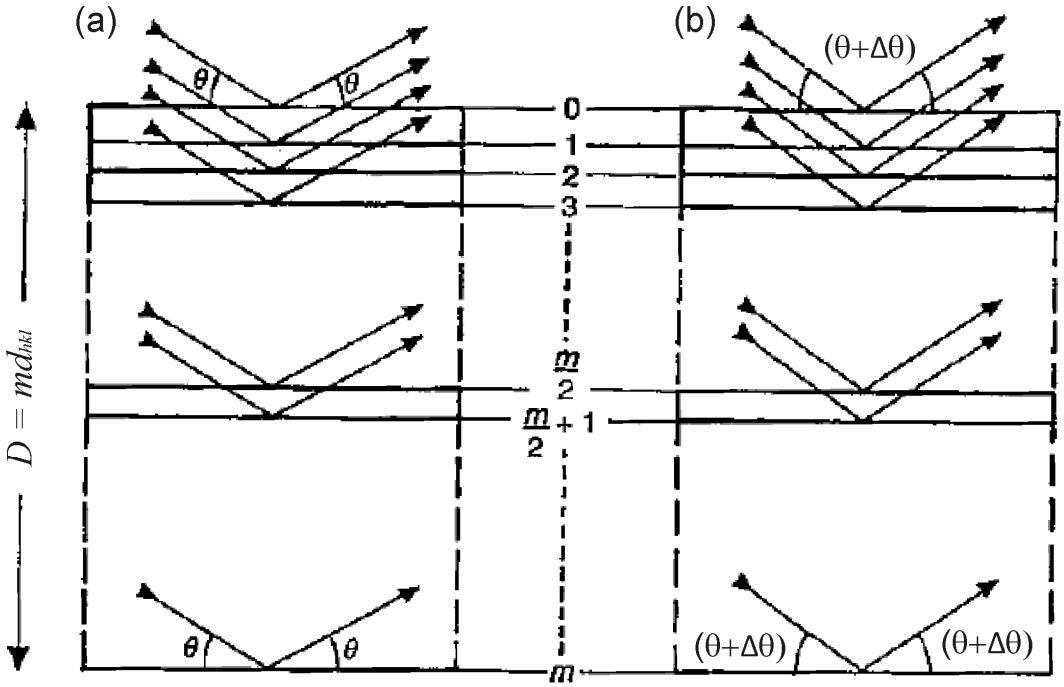

Figure 2.13. Bragg reflection from a crystal of thickness D. The crystal is (a) at the exact Bragg angle θ and (b) at a small deviation from the exact Bragg angle i.e. angle ($\theta+\Delta\theta$). The arrows represent the incident and reflected beams from successive planes 0,1,2,3… (m/2) (half-way down) and … m (the lowest plane) [34].

Broadening can be represented in the Ewald sphere as the extension of the reciprocal lattice point to a node of finite size which, as the crystal rotates, intersects the reflecting sphere over this angular range (Figure 2.14 (b)). This effect is usually accessed from the highest intensity peak to maximize accuracy. For particle size less than 100 nm appreciable broadening in X-ray diffraction lines will occur and Scherrer equation yields precise results. For larger crystals, the method is rather insensitive and should not be used [1,43].

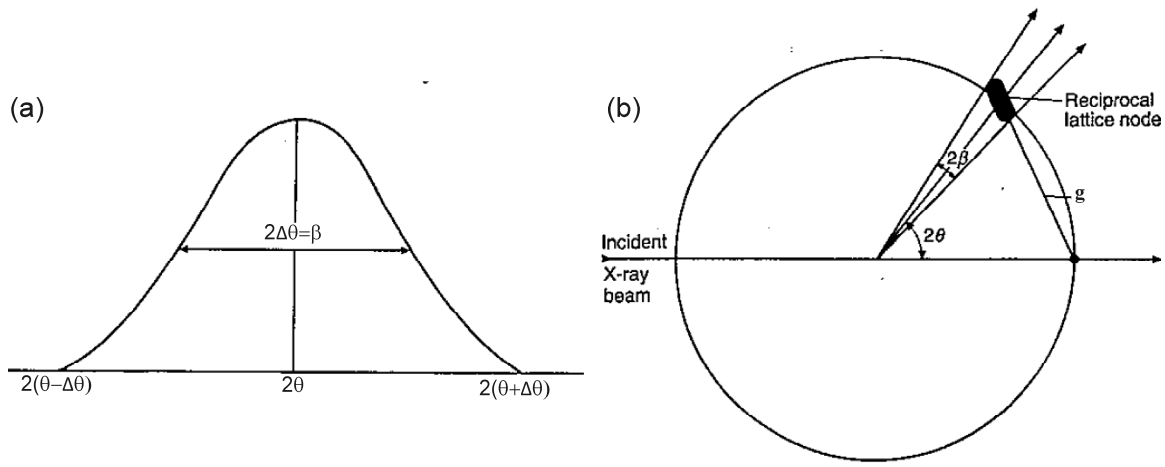

Figure 2.14. (a) Broadened Bragg peak arising from a crystal of finite dimension. β is equal to $2\Delta\theta$. The angular 2θ scale is measured in relation to the direct and reflected beams. (b) The Ewald reflecting sphere construction for a broadened reflected beam, where β corresponds to an extension proportional to $1/D$ of the reciprocal lattice node [34].

2.1.3.1.8 Williamson-Hall method (crystallite size and strain)

Scherrer equation attributes peak broadening exclusively to crystal size, not taking into account microstrain. The Williamson-Hall approach [44] enables to separate the two effects:

$$\beta=\beta_{size}+\beta_{strain}=\beta_m-\beta_i \tag{2.16}$$

where β_m and β_i have been defined in Equation 2.13. Broadening resulting from crystallite finite size depends on $1/cos\theta$ (Eq. 2.15), while broadening resulting from strain (ε), which is the variation in plane spacing ($\Delta d/d$), can be determined by differentiating Bragg's law [37,45]:

$$\frac{\Delta d}{d}=-\frac{cos\theta\Delta\theta}{sin\theta}=-\frac{cot\theta\,\beta}{2} \tag{2.17}$$

Hence the total broadening is:

$$\beta=\frac{\lambda K}{Dcos\theta}-\frac{2\Delta dsin\theta}{dcos\theta}, \text{ i.e., } \beta\,cos\theta=\frac{\lambda K}{D}+2\,|\varepsilon|\,sin\,\theta \tag{2.18}$$

where D, λ, β, K and θ have been defined for Equation 2.15. In the Williamson-Hall method, $(\beta_m - \beta_i)\cos\theta$ is plotted against $2\sin\theta$. Thus from a linear extrapolation the intercept yields the particle size and the slope reflects strain [39]. In order to increase accuracy, the largest number of peaks is generally employed in the fitting.

2.1.3.1.9 Precise lattice parameter determination

Lattice parameters can be determined from PXRD data through the central position of each diffraction peak. However, in order to obtain correct values the geometry of diffraction requires the specimen to lie at the center of the focusing circle (see Figure 2.12), and the detector to remain in the focal circle so that the spread of the diffracted beam is minimized. Incorrect alignment of the diffractometer and/or misplacement of the specimen on the diffractometer goniometer are common errors that influence the determination of d and hence the lattice parameter value. Moreover, even with perfect alignment the diffraction signal originates from a region beneath the specimen surface, and not from the surface itself, which results in an error in the apparent diffraction angle.

An apparent shift at the detector of $\hbar\cos\theta$ corresponds to an $\Delta\theta$ error in diffraction angle (Figure 2.15) [46]:

$$\Delta\theta = \frac{\hbar\cos\theta}{\mathrm{R}} \tag{2.19}$$

where R is the radius of the goniometer circle and $\hbar$ is the specimen shift. Bragg's law differentiation (Eq. 2.17) suggests that when θ is brought as much as possible close to 90º, the fractional error in d as denoted by $\Delta d/d$, equivalent to resolution, approaches zero, so that the use of diffraction peaks as close to the value of 2θ =180º results in highest precision of lattice parameter determination [47]. Thus, substituting Equation 2.19 into Equation 2.17, the shift effect in lattice parameter is given by:

$$\frac{\Delta d}{d} = \frac{\hbar}{\mathrm{R}}\frac{\cos^2\theta}{\sin\theta} \tag{2.20}$$

Measuring at 2θ =180º is physically impossible and extrapolation methods are usually employed, based on the systematic trend of the lattice parameter values obtained from a series of different Bragg peaks. In the cubic system the lattice parameter (a) is

determined from each peak with $a = \frac{\sqrt{h^2+k^2+l^2}}{2sin\theta}$ [46]. In the simplest extrapolation method the a values are plotted against $cos^2\theta/sin\theta$ (see Eq. 2.20). A straight line is assumed, and for the a value at the y-intercept (θ=90º) the specimen shift and X-ray penetration depth effects are eliminated [46]. The Cohen extrapolation method utilizes $cos2\theta$ instead of the function defined in Equation 2.20. The method of Nelson–Riley uses the relationship given by $\frac{\Delta a}{a} \propto \frac{1}{2}\left\{\frac{cos^2\theta}{sin\theta} + \frac{cos^2\theta}{\theta}\right\}$, which in practice results in straighter lines for cubic systems [46].

In addition, a standard substance of known lattice parameter can be mixed with the sample of interest, acting as an internal calibration. High-purity silicon powder is widely used as "internal standard" to eliminate systematic errors [47]

The lattice parameter of a material is sensitive to its chemical composition, being reasonably linearly-dependent on the atom fraction of solute for metallic alloys with close-packed structures (Vergard's law) [46].

The Nelson–Riley extrapolation method and Si powder as an internal standard have been employed in the current study for precise lattice parameter determination, which has been used to establish the extent of carbon dissolution in the metallic matrix through Vergard's law.

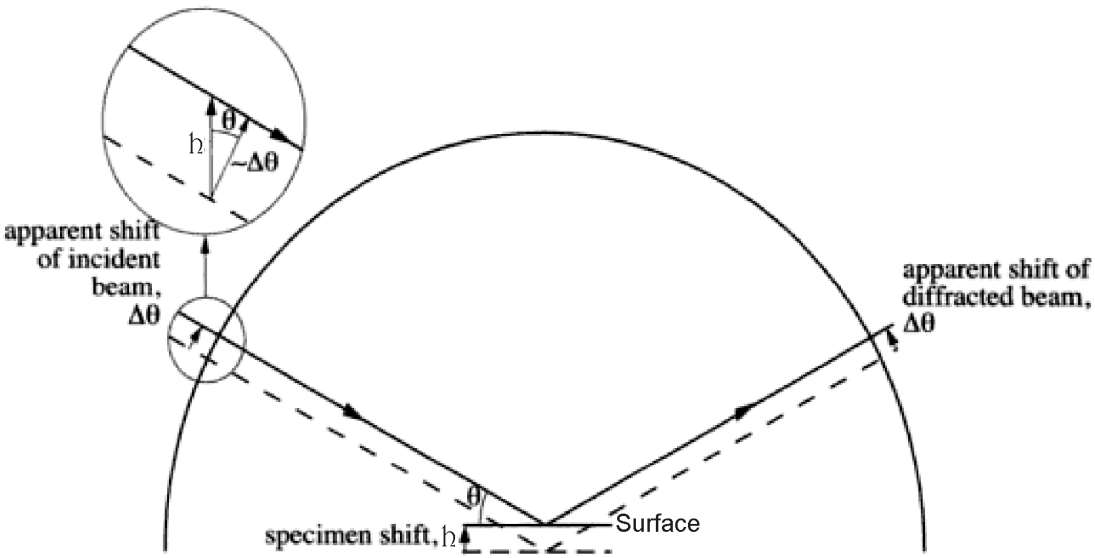

Figure 2.15. Diffraction signal originating from below the focusing plane (sample surface) [46].

2.1.3.2 Electron microscopy

When electrons are accelerated up to high energy levels (few tens to hundreds keV) and focused on a material, they can scatter or backscatter elastically or inelastically, and produce various interactions, source of other signals types such as secondary electrons, transmitted electrons, X-rays, Auger electrons and visible light. The several signal types generated can be detected to produce images, diffraction patterns and electromagnetic spectra in electron microscopy.

In the present work, general microstructural characterization and local crystallographic and elemental analyses of the metal-carbon materials have been carried through scanning and transmission electron microscopy and the associated energy dispersive spectroscopy. The working principles of these techniques will be briefly described in the following sections.

2.1.3.2.1 Scanning electron microscopy

Scanning electron microscopy is a powerful technique capable of producing images with resolution around 1 nm. The scanning electron microscope includes a source of high-energy electrons (thermoionically emitted from a tungsten or lanthanum hexaboride cathode or, alternatively, generated via field emission) which are accelerated towards an anode; and a condenser system, composed by electromagnetic lenses to focus the electron beam into a fine probe (sized 1 nm to 5 nm) that impinges on the specimen. The so-called “objective” lens, the ultimate electromagnetic probe lens, determines the resolution attainable by the microscope. Nevertheless, the probe lens is placed above the specimen, and has no part in collecting the image signal. The beam passes through pairs of scanning coils, which deflect the beam horizontally and vertically (see Figure 2.16) so that it scans in a raster fashion over a rectangular area of the sample surface.

In the case of bulk samples, when the primary electron beam is focused on the material, the electrons lose energy by recurrent scattering and absorption within a teardrop-shaped volume of the specimen known as the interaction volume, which extends from less than 100 nm to around 5 μm into the sample. The size of the interaction volume (see Figure 2.17) depends on the beam accelerating voltage, the atomic number of the specimen and its density. Secondary electrons (SE) are defined as

electrons emitted from the specimen with energy less than 50 eV, and are generally produced as a result of interactions between energetic primary electrons and weakly bound conduction electrons in the sample. An important characteristic of secondary electrons is their shallow sampling depth (see Figure 2.17), a direct consequence of the low kinetic energy with which they are formed [49]. SE are detected by an Everhart-Thornley detector which is a type of scintillator-photomultiplier device, and the resulting signal is rendered into a two-dimensional intensity distribution that can be viewed and saved as a digital image. The brightness of the SE signal depends on the number of electrons reaching the detector. If the beam enters the sample perpendicularly to the surface, then the activated region is uniform about the axis of the beam and a certain number of secondary electrons "escape" from within the sample. As the angle of incidence increases, the "escape" distance of one side of the beam will decrease, and more secondary electrons will be emitted. Thus steep surfaces and edges tend to be brighter than flat surfaces resulting in topographical images with well-defined, three-dimensional appearance. The SE signal allows spatial resolutions of less than 1 nm.

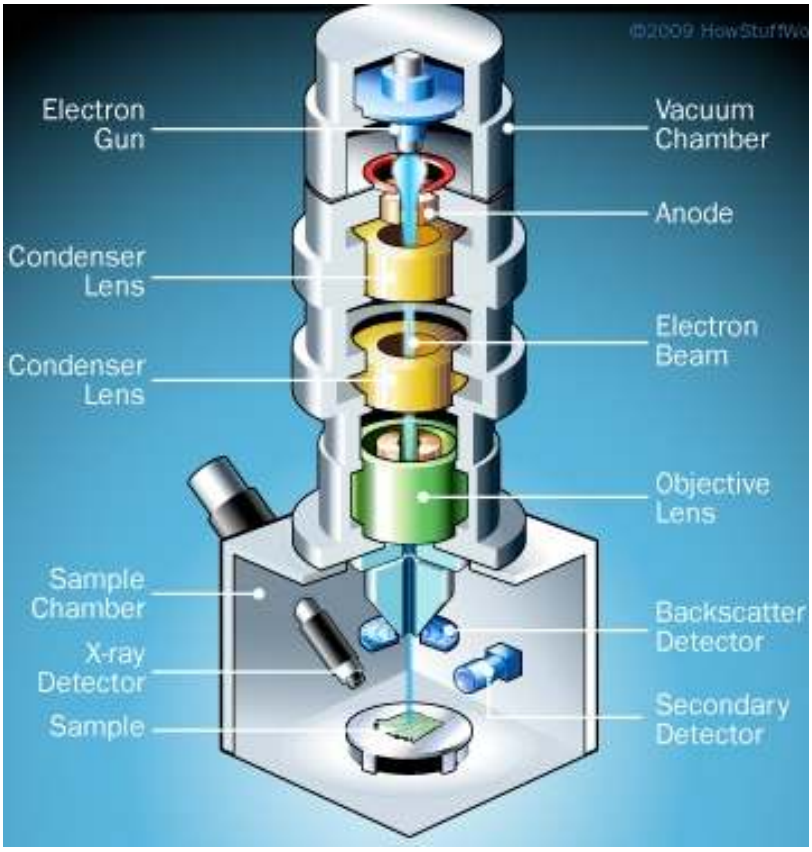

Figure 2.16. Diagram of a scanning electron microscope [48].

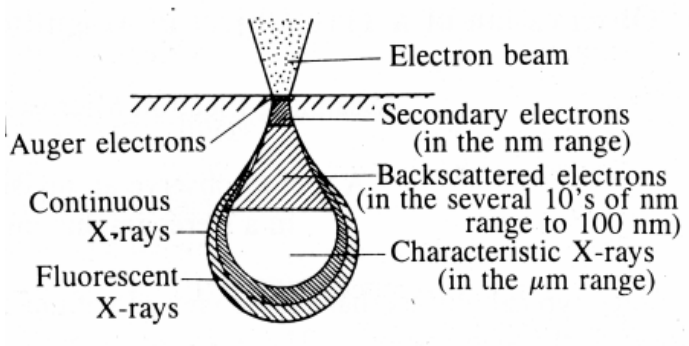

Figure 2.17. Interaction volume with indication of signal origin [49].

Backscattered electrons (BSE) are high-energy electrons and can escape from a much larger volume than SE (see Figure 2.17). The signal intensity will depend on the average atomic number of the specimen but is almost independent of topography. BSE images have lower spatial resolution than SE images due to their larger volume of origin, but show contrast between areas with different chemical composition, since the signal intensity increases with the local atomic number of the sample. The average energy of the backscattered electrons is of the same order of magnitude. The number of BSE leaving the sample surface upward might be significantly lower than those that follow trajectories toward the sides. Additionally, in contrast with the case of secondary electrons, the collection efficiency of backscattered electrons cannot be significantly improved by a positive bias (common on Everhart-Thornley detectors) due to their high kinetic energy. As a result, a detector positioned on one side of the sample has low detection efficiency for BSE due to the limited solid angle. The use of a dedicated backscattered electron detector above the sample in a "doughnut" type arrangement, with the electron beam passing through the hole of the doughnut, greatly increases BSE collection.

2.1.3.2.2 Transmission electron microscopy

In transmission electron microscopy a beam of electrons, focused by multiple electromagnetic lenses, is transmitted through a specimen. The lens system is designed to eliminate stray electrons as well as to control and focus the electron beam. The electrons that have passed through the sample can be collected either by means of a fluorescent screen/photographic film or a charge coupled device (CCD) camera. The technique is able of achieving resolutions of less than 0.1 nm.

A transmission electron microscope consists of two or three condenser lenses that focus the electron beam on the sample; an objective lens to form the diffraction pattern in the back focal plane and the image of the sample in the image plane; and some intermediate and projection lenses to magnify the image or the diffraction pattern on the screen, film or CCD (Figure 2.18). The optical system of a TEM is shown in Figure 2.19.

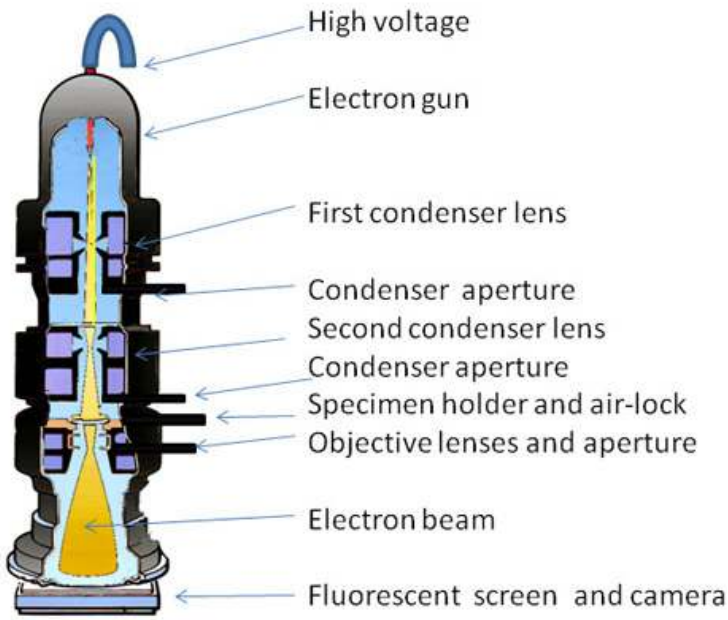

Figure 2.18. Diagram of a transmission electron microscope [50].

The objective lens generates simultaneously the diffraction pattern and the first intermediate image. Figure 2.19 shows that the ray paths are identical until the intermediate lens, where the field strength is changed, depending on the desired operation mode. Higher field strength (shorter focal length) is used for imaging, whereas weaker field strength (longer focal length) is used for diffraction. A crystalline material interacts with the electron beam mostly by diffraction rather than absorption. The intensity of diffraction depends on the orientation of the planes of atoms in the crystal relative to the electron beam; at certain angles the electron beam is strongly diffracted, while at other angles the beam is largely transmitted. This is the most common contrast generation mechanism in imaging of crystalline materials and the microscope is often equipped with a specimen holder that allows the user to tilt the specimen to a range of angles in order to obtain specific diffraction conditions. An aperture placed below the specimen (objective aperture in Figure 2.19) allows the user to select specific diffracted beams to form the specimen images.

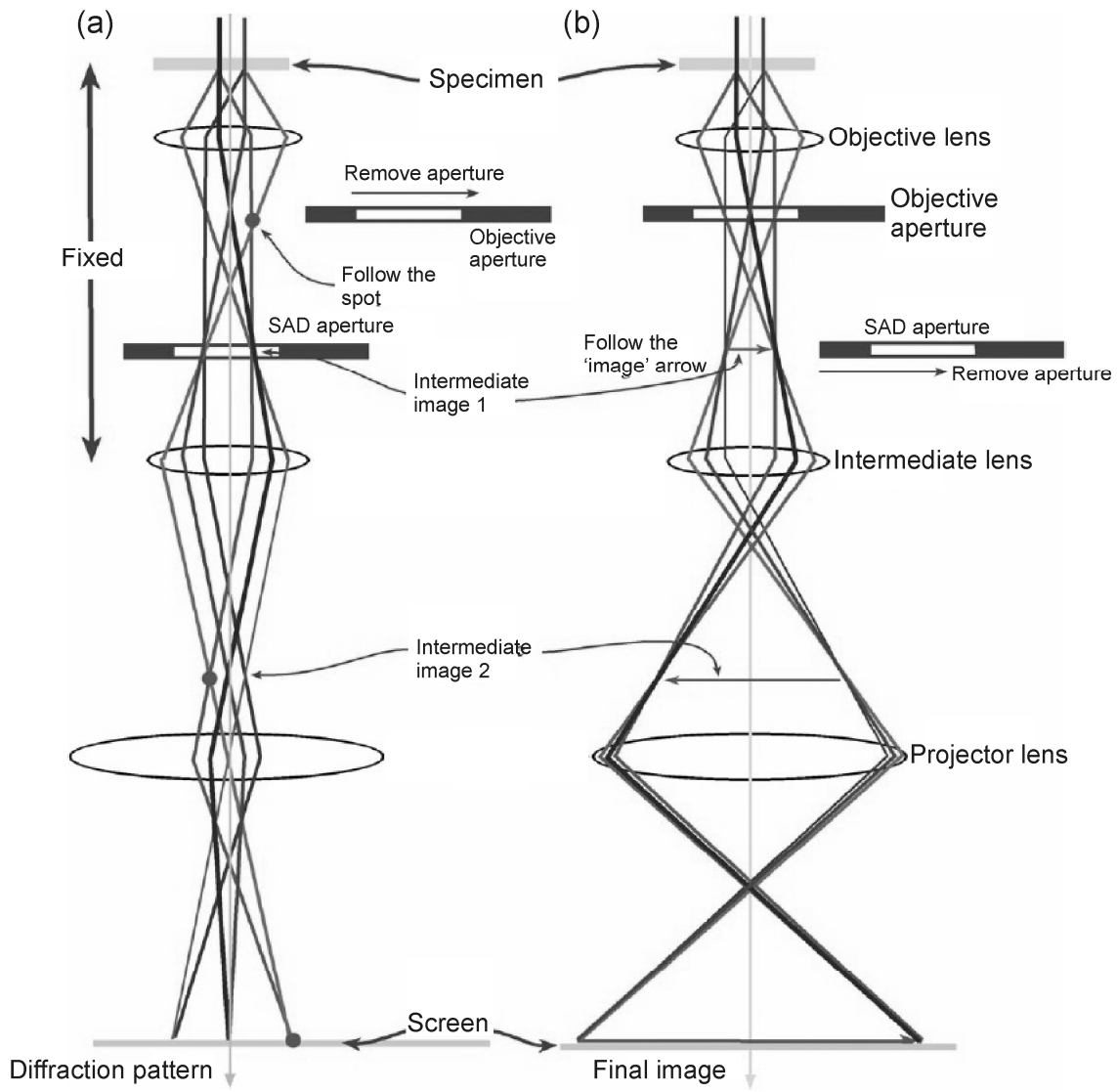

Figure 2.19. Optical system of TEM: (a) diffraction mode and (b) imaging mode [51].

Bright-field mode (BF) (Figures 2.20 and 2.19 (b)) is commonly used to obtain contrasted images in most observations. Under this mode, an objective aperture is inserted into the back focal plane of the objective lens, the same plane at which the diffraction pattern is formed, just below the sample. The aperture only allows transmitted electrons to contribute for the bright-field image, where intensively diffracting regions present thus dark contrast. Off-axis dark-field images are obtained by positioning the objective aperture around a specific diffracted beam, so that only this beam is allowed to form the image (Figure 2.21(a)). In this case, the intensively diffracting regions appear bright in a dark background. In order to minimize lens aberrations under dark-field, the incident beam is usually deflected along the optic axis, so that the diffracted beam is aligned along the optical axis of the instrument resulting in on-axis dark-field imaging (Figure 2.21(b)).

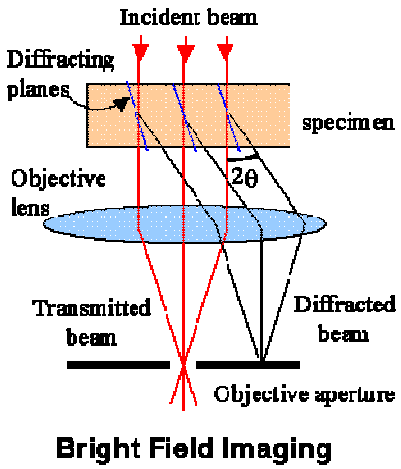

Figure 2.20. Bright-field mode of imaging [52].

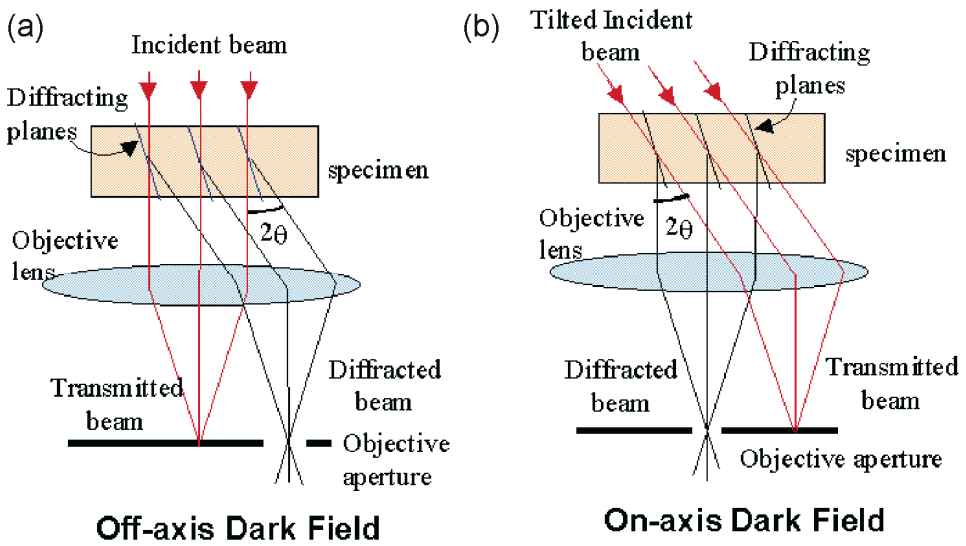

Figure 2.21. (a) Off-axis dark field mode (higher aberrations) and (b) On-axis dark field mode (minimization of lens aberrations) [52].

Crystallographic information from a defined region can be accessed through selected area diffraction (SAD), which reduces both the area and the intensity of the beam contributing to the diffraction pattern by the insertion of an aperture (selected area diaphragm) into the image plane of the objective lens (Figures 2.19 (a) and 2.22). This produces a virtual diaphragm in the plane of the specimen and results in a sharp diffraction pattern.

Alternatively, diffraction patterns can be obtained by focusing the electron beam with the condenser lenses to obtain a small spot size on the object (2-10 nm). Under this diffraction mode, called microdiffraction, diffraction spots become disks whose radii

depend on the condenser diaphragm size. In this case crystallographic information can be obtained from nanometric regions.

SAD and microdiffraction patterns enable to determine the symmetry of crystalline lattices and therefore to identify specific phases in the microstructure.

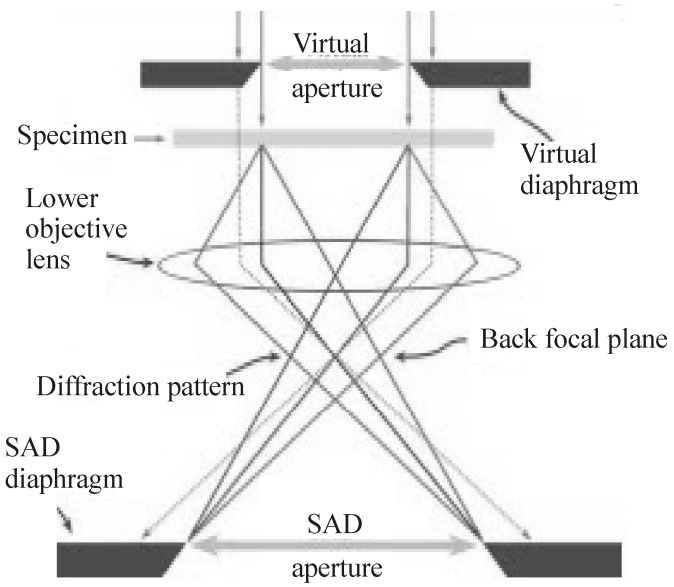

Figure 2.22. Ray diagram showing SAD pattern formation: the insertion of an aperture in the image plane results in the creation of a virtual aperture in the plane of the specimen (shown here slightly above the specimen plane). Only electrons falling inside the dimensions of the virtual aperture at the entrance surface of the specimen will be allowed through into the imaging system to contribute to the SAD pattern. All other electrons will hit the SAD diaphragm [51].

Spot patterns are generated when electrons are diffracted in a single crystal region, with the central spot corresponding to the transmitted beam and the other to diffracted beams. The spots are indexed with a combination of Bragg's law and the geometric relationship in reciprocal space represented in Figure 2.23:

$$tan2\theta = \frac{R}{L} \tag{2.21}$$

In TEM the diffraction angles are small and $\theta \sim sin\theta \sim tan\theta$, and substituting Equation 2.21 into Bragg's law (Eq. 2.11):

$$Rd = \lambda L \tag{2.22}$$

where d and λ have been defined in Equation 2.11, R is the distance between the transmitted beam and a specific diffraction spot and L, known as the camera length,

defines the diffraction pattern magnification, and represents the distance between the sample and the photographic film or CCD camera.

Ring patterns are created when electron diffraction occurs simultaneously from many grains with different orientations relative to the incident electron beam. The radii and spacing of the rings are also governed by Equation 2.22 where in this case R represents each ring radius.

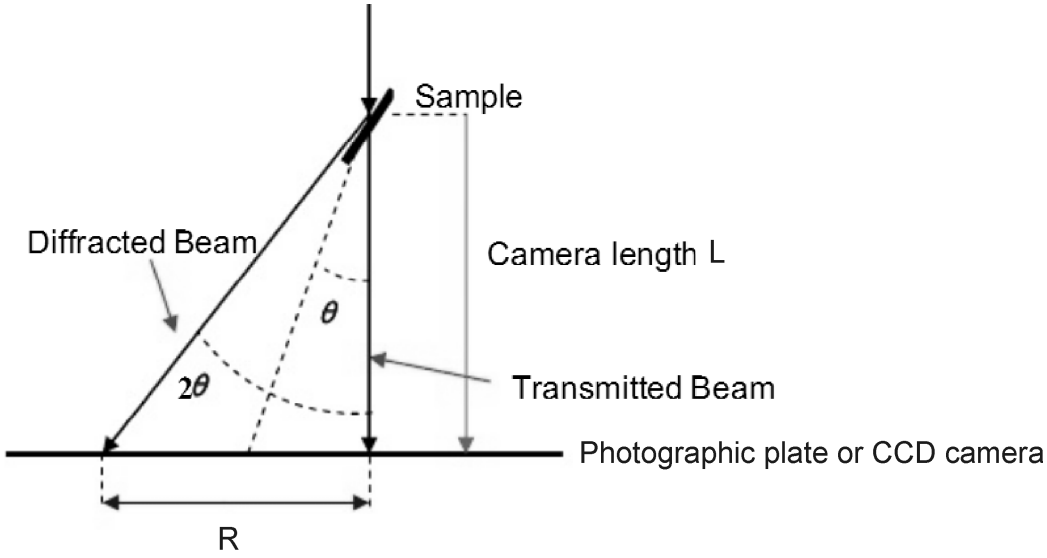

Figure 2.23. Diffracted and transmitted beam paths [53].

.

2.1.3.3 Energy dispersive X-ray spectroscopy

EDS is an analytical technique that uses X-rays emitted from the specimen when bombarded by energetic electrons to identify its elemental composition. The convenience of EDS spectrometers association with electron microscopes is widely acknowledged: these instruments are intrinsically equipped with a cathode and magnetic lenses to create and focus a beam of high-energy electrons. An EDS spectrum is constituted by a continuous background and peaks characteristic of the elements present in the material. The X-ray generative principle was previously described in 2.1.3.1.3.

The energy dispersive X-ray spectrometer comprehends the following components: beam source, X-ray detector, pulse processor and analyzer (Figure 2.24). A Si(Li) detector converts the energy of each X-ray photon into a voltage signal of proportional size, this information is sent to a processor to produce an electrical pulse of

specific amplitude and width, which is passed onto an analyzer that sorts the emitted X-rays in function of their energy for data display and analysis.

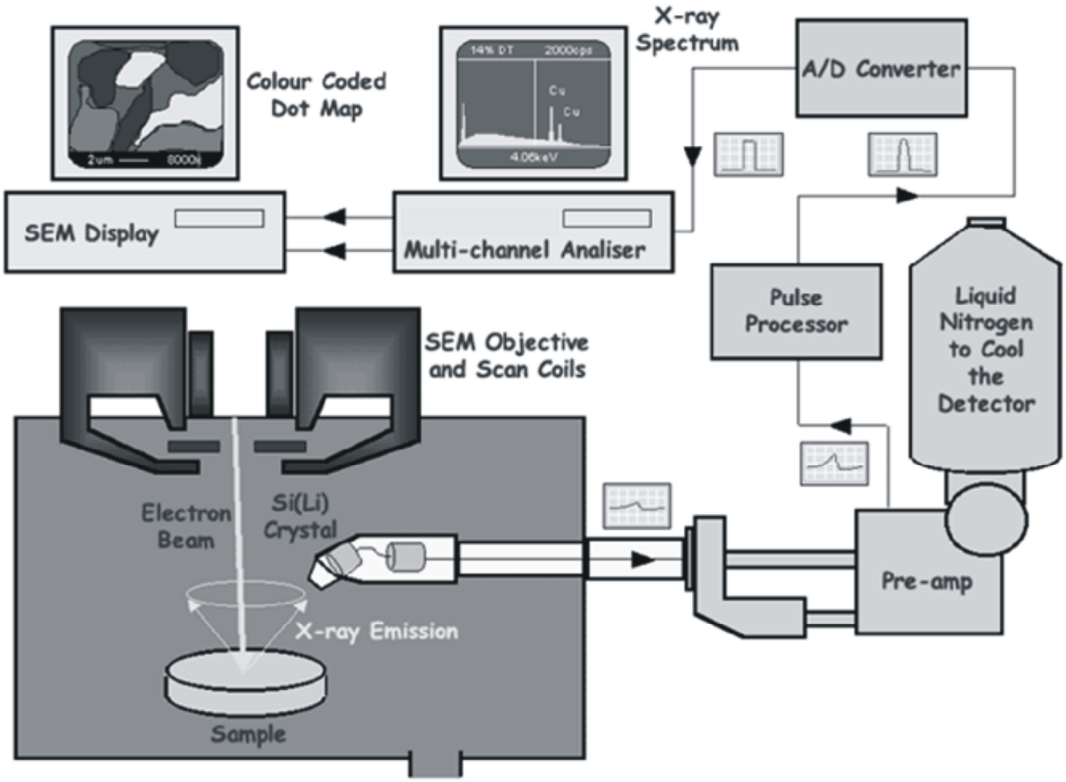

Figure 2.24. Energy dispersive X-ray spectrometer in an electron microscope [54].

The analysis of EDS spectra is based on the link between the elemental fractions present in the sample and the generated intensity of the characteristics peaks. It requires therefore background removal and peak deconvolution before determination of integrated intensities. In standardless or semi-quantitative analysis, the dependence of the ionization cross section on the atomic number is theoretically considered, as well as other matrix effects, such as absorption and fluorescence. Alternatively, standards with known composition c_{st} are used and the concentration c_i of an *i* element can be inferred from the peak intensity ratio I_i / I_{st} :

$$c_i / c_{st} = \mathcal{K}\, I_i / I_{st} \qquad (2.23)$$

where I_i is the peak intensity measured in the sample and the I_{st} is the peak intensity for the *i* element in the standard. $\mathcal{K}$ is the correction factor that includes the three matrix effects [55].

The relative errors associated with the ZAF corrections in standardless analysis are about 10%, while when standards are used the results are quantitative. Nevertheless, due to the ease of use, standardless analysis is universally employed for rapid elemental assessment.

2.1.3.4 Particle-induced X-ray emission spectrometry

As with EDS, PIXE utilizes the X-ray generative principle previously described in 2.1.3.1.3. The difference between both techniques is the mechanism by which the inner shell electron is emitted. In EDS, an incident focused electron beam is employed, while for PIXE analysis, collimated ion beams are used. For an efficient electron shells ionisation, the particle energy must be greater than the ionisation potential of the electron, and the velocity of the particle must match the velocity of the electron in its orbital.

Proton sources are commonly used in PIXE experiments, and since protons are about 1836 times more massive than electrons, greatly less deceleration is obtained, and therefore much weaker Bremsstrahlung emission is induced. The continuous Bremsstrahlung radiation is reduced in PIXE spectra by a factor of about 100 relatively to the equivalent EDS experiments, resulting in lower background and sharper X-ray characteristic peaks. The induced X-ray emission is quite isotropic while Bremsstrahlung radiation is maximized along the direction perpendicular to the incident beam axis, and the detection geometry of the experimental apparatus is commonly optimized in order to improve the sensitivity of the technique, which typically is of the order of ppm for most elements (the reported sensitivities of the technique are 10–20 ppm for Na to Cl and 1–10 ppm for Ca and heavier elements [56]).

In a PIXE spectrometer, a finely collimated proton beam is produced by an ion accelerator, and hits perpendicularly the sample. X-ray absorber filters can be positioned in front of the X-ray detector, which typically is of Si(Li)-type, to attenuate dominant peaks of lower energy, allowing for greater trace sensitivity for heavier elements. Thin absorber foils can be also used to avoid the formation of lattice defects in the detector crystal caused by the incidence of protons scattered from the sample surface. The use of an internal Faraday cup is not a requirement, however it provides secondary electron suppression, measuring and controlling of the relative number of protons that strikes the sample (see Figure 2.25). For data analysis, an interactive

software package is normally used to convert raw spectral data into elemental concentrations [57].

The technique has been employed in the present work to precisely quantify the contamination arising from the milling media and incorporated in the milled metal-carbon nanocomposites.

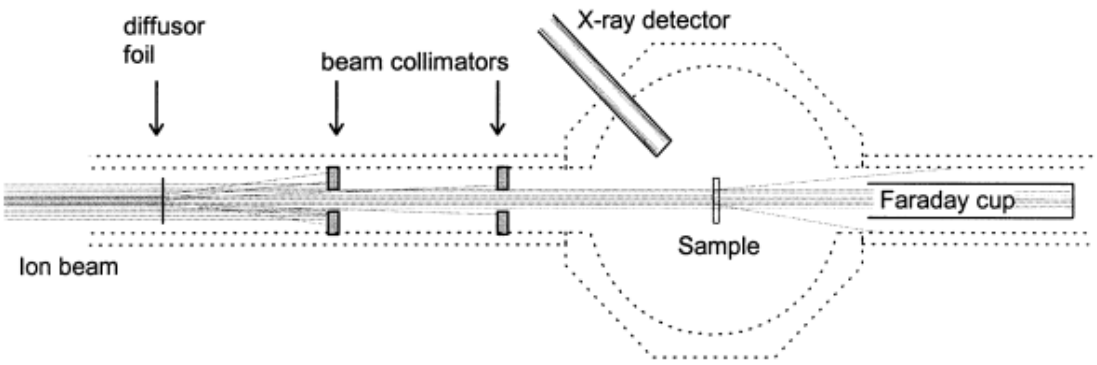

Figure 2.25. PIXE set-up [58].

2.1.3.5 Raman spectroscopy

Raman spectroscopy is used to investigate the way in which radiation is inelastically scattered by a sample. When the light source (usually in the form of a laser) is focused on a substance most of the beam energy is scattered inelastically: the molecules of the substance are excited to a virtual electronic state and immediately fall back to their original state by releasing a photon. The laser beam used may be in the near-UV, visible or near-infrared regions of the spectrum [59].

The Raman effect is based on molecular deformations induced by the electric field determined by molecular polarizability: the laser beam can be considered as an oscillating electromagnetic wave with electrical vector E, and upon interaction with the sample it induces electric dipole moment which deforms periodically the molecules (Eq. 2.24) [60].

$$P = \alpha \mathsf{E} \qquad (2.24)$$

where α is the molecular polarizability and P is the electric dipole moment.

In other words, the laser light with frequency υ_0 excites molecules and transforms them into oscillating dipoles, which emit light of three different frequencies:

(i) A molecule with no Raman-active modes absorbs a photon and returns back to the basic vibrational state by emitting light with υ_0 frequency. This type of interaction is called elastic Rayleigh scattering.

(ii) Upon absorption of a photon, a Raman-active molecule, which at the time of interaction is in the basic vibrational state, starts vibrating with characteristic frequency υ_m and amplitude (nuclear displacement). Part of the photon's energy is transferred to the Raman-active mode with frequency υ_m and the frequency of the resulting scattered light is reduced to $\upsilon_0 - \upsilon_m$, called Stokes frequency

(iii) Upon absorption of a photon, a Raman-active molecule, which at the time of interaction is already in the excited vibrational state, releases the excess energy when returning to the basic vibrational state and the frequency of the resulting scattered light is $\upsilon_0 + \upsilon_m$., called AntiStokes frequency.

About 99.999% of all incident photons in spontaneous Raman undergo elastic Rayleigh scattering, which is useless for practical purposes of molecular characterization. Only about 0.001% of the incident light produces inelastic Raman signal with frequencies $\upsilon_0 \pm \upsilon_m$ [61].

The difference in energy between the incoming and scattered photon (Raman shift) corresponds to the energy difference between vibrational energy levels of the molecule (Figure 2.26). The different vibrational modes of a molecule can therefore be identified by recognizing Raman shifts (or 'bands') in the inelastically scattered light spectrum.

A Raman system typically consists of four major components: the excitation source (laser), the sample illumination system and light collection optics, the wavelength selector (filter or spectrophotometer), and the detector. The scattered light is collected with a lens and is sent through an interference filter or spectrophotometer to produce a Raman spectrum. It should be noticed that Raman scattering is effective for covalent bonds, and very weak for ionic and metallic bonds [61].

In the present work Raman spectroscopy was used to characterize the phase transformations occurring in the carbon phases during the ball milling operation in the presence of metal atoms and during the subsequent annealing treatments.

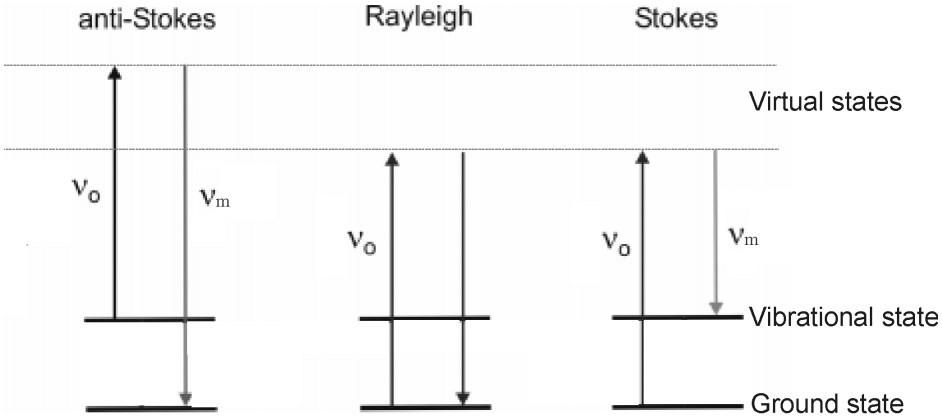

Figure 2.26. Energy level diagram representing the elastic Rayleigh scattering and the inelastic anti-Stokes and Stokes Raman scattering [62].

Carbon phases display unique Raman peaks that ensure precise identification. Pure diamond crystals exhibit one Raman peak at ~1332 cm^{-1}corresponding to the vibration of sp^3 bonds (F_{2g} mode) [63]. For nanodiamond a downshift and asymmetric broadening of this Raman line occurs due to phonon confinement [64]. Furthermore, polycrystalline diamond frequently presents regions with graphitic [65–67] and/or amorphous carbon [66,67] and exhibits additional bands in the Raman spectrum. Raman spectra of large graphite crystals show a sharp peak at 1580 cm^{-1}, corresponding to the vibration of sp^2 bonds (E_{2g} mode) [66,68]. Due to phonon confinement, for small crystallite sizes the sharp peak becomes a broad band (G-band) and two additional 'disorder' peaks appear at 1355 cm^{-1} (D-band, A_{1g} vibration mode) [68,69] and 1620 cm^{-1} (D′-band) [64,70]. Amorphous carbon produces a broad asymmetric band in the 1000-1600 cm^{-1} region [71,72].

2.1.3.6 Microhardness

Hardness is the plastic resistance against local penetration, which is related to the indentation area in loaded state [73]. A conventional microhardness testing procedure consists of applying a fixed load, typically in the 0.01-1 kgf range [74], through a diamond indenter and measuring the dimension of the resulting indentation on the material surface after unloading. The hardness value is given by the ratio of the applied load, F, to the indentation contact area, A:

$$H = \frac{F}{A} \tag{2.26}$$

A variety of indenter geometries are available, and the most commonly used, the Vickers indenter, consists of a diamond four-sided square based pyramid with an angle of 136º between opposite faces. The Vickers hardness number (HV) is determined through Equation 2.26, using:

$$A = \frac{d^2}{2\sin\left(\frac{136}{2}\right)} \tag{2.27}$$

where d is the arithmetic mean of the indentation diagonal lengths in millimeters [75]. For F in kgf:

$$HV = \frac{2F\sin\left(\frac{136}{2}\right)}{d^2} = \frac{1.854F}{d^2} \tag{2.28}$$

Since the size of the geometrically similar indentation increases linearly with the load, the Vickers hardness number is reasonably independent of the load applied (an exception worth mentioning is the indentation size dependence observed for the low loads used in nanoindentation [75-77]). In consequence, Vickers hardness is a versatile mechanical characterization method for parts of various thickness and size [75].

There is a straightforward correlation between the materials hardness, as given by the Vickers number, and the yield stress, a fundamental mechanical property of the material, known as the Tabor factor [78].

Since the indenter surface is not parallel to the sample surface, the stress state generated during indentation is complex. The problem can be treated in two dimensions assuming a plane strain state [79,80]. In these conditions, according to the Huber-Mises criterion, plastic deformation occurs when the maximum shear stress reaches a critical value, k, [79,80], so that:

$$2k = 1.15\sigma \tag{2.29}$$

where σ is the yield stress. The slip-line field theory can then be used to define the pattern of plastic flow around the Vickers indenter [81] (see Figure 2.27), and the estimated pressure normal to the surface of the indenter (P) is:

$$P = 2k\left(1 + \frac{\pi}{2}\right) \tag{2.30}$$

Replacing Equation 2.29 into 2.30, results in:

$$P = \frac{2\sigma}{\sqrt{3}}\left(1 + \frac{\pi}{2}\right) \sim 2.96\sigma \tag{2.31}$$

The Vickers hardness number is related to the applied pressure through: HV = 0.927 P, as 0.927 is the ratio of the area of the base of the pyramid (the projected area) to the area of the sides of the pyramid (contact area). Considering Equation 2.31, the Tabor stated the following relationship [75]:

$$HV = 2.74\sigma \tag{2.32}$$

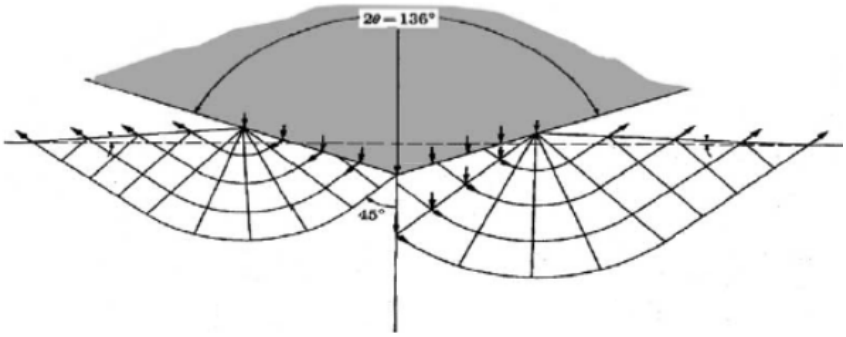

Figure 2.27. Slip-line field produced by a Vickers indenter [80].

2.1.3.7 Differential thermal analysis

In differential thermal analysis the material under study and an inert reference are submitted to identical thermal cycles, while recording the temperature difference between them, which is derived from the voltage difference between the sample and the reference thermocouples and is then plotted against time or temperature. Phase transformations occurring in the samples, either exothermic or endothermic, can be detected relative to the inert reference. The minimum temperature difference detectable is typically 0.01 K [82].

The DTA equipment (Figure 2.28) comprises a pair of crucibles, thermocouples, furnace, temperature programmer and a recording system. The temperature programmer is essential in order to obtain constant heating rates, and the furnace should provide a stable and sufficiently large hot-zone and must respond rapidly to commands of the temperature programmer. The crucibles are supported by a pair of vertical thermocouples (differential thermocouple). The differential thermocouple output (heat flow in micro-volts or differential temperature) is displayed on a PC monitor as a function of time or temperature. High purity alumina is a standard DTA crucible

material. Zirconia and yttria crucibles can be used for highly reactive metals [83]. The apparatus works under inert gas, such as helium or argon.

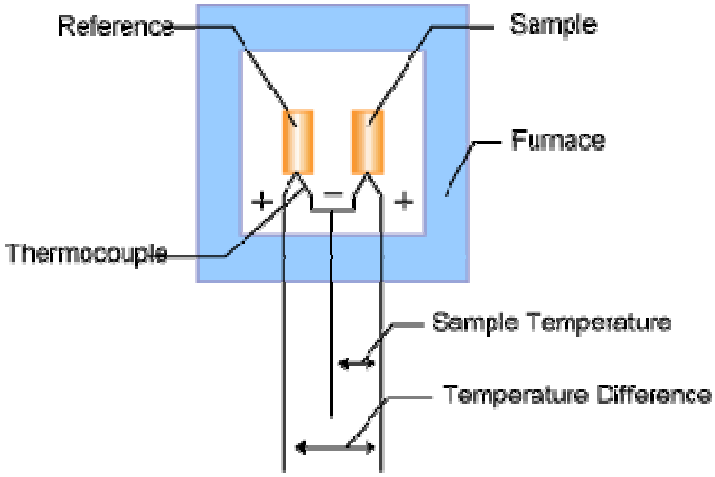

Figure 2.28. Diagram of a DTA furnace [84].

The onset temperature of a transformation is usually inferred from the DTA curve derivative. On heating, melting requires an input of heat and the downward peak is endothermic, whereas on cooling, freezing releases heat and the upward peak is exothermic. A similar interpretation is used for any other phase transformations occurring during the thermal cycle. Larger sample masses produce larger peak signals (deflection from the baseline) which are therefore more easily detected. However, larger masses also delay the temperature at which the signal returns to the baseline, rendering detection of closely spaced thermal events more difficult. Sample shape is also a significant factor to take into account since the thermal contact area between the sample and the cup will change during the melting process [85].

2.2 Specific experimental details

The nanodiamond particles were purchased from the NanoCarbon Research Institute as NanoAmando Hard Hydrogel, with a water content of 21.5% and a nominal average particle diameter of 5.0 nm [86,87]. Although a previous high-resolution TEM investigation has shown that each nD particle presents in fact multiple 4-5 nm cores enveloped by graphite-like layers [88]. Prior to milling, the water was evaporated from the Hard Hydrogel for 4 h at 338 K. This operation resulted typically in nD

agglomerates with 2–3 μm in size, which were subsequently disintegrated during milling [89]. The graphite powder (G) was of synthetic origin with 99.99% of purity, had an average particle size of 74 μm, and consisted of a mixture of hexagonal (2H) and rhombohedral (3R) phases [90]. Copper powder had 99.95% purity and particle sizes in the 44-149 μm range. Nickel powder had 99.9% purity and an average particle size of 44 μm. Tungsten powder had 99.95% purity and median particle size of 1 μm.

Milling has been performed in a Retsch PM400 planetary ball mill. DIN 1.4034 stainless steel mill containers were employed with 10 mm diameter hardened DIN 1.4034 stainless steel balls. Hardmetal mill containers and 10 mm diameter balls (WC–6 wt.% Co) have also been used. The containers were evacuated and filled with argon to prevent oxidation during the milling operation.

The heat treatments were carried out by placing the powders directly in silica crucibles in an evacuated furnace under an argon atmosphere.

XRD measurements have been performed with a RIGAKU Geigerflex diffractometer fitted with a graphite monochromator, using CuK_{α} radiation. The measurements were performed in the 20º–110º 2θ range at 0.01º/s. XRD data analysis took into account a calibrated instrumental broadening of 0.11°. The average Cu and Ni grain sizes were determined through Scherrer equation using K=0.89 (Scherrer factor), and the internal strain effect was accessed through the Williamson–Hall approach [44]. Lattice parameters were determined with the Nelson–Riley method [39,47], and the results were confirmed using the software package PowderCell [91]. Silicon was employed as internal standard material.

Microstructural observations were carried out after standard metallographic preparation by SEM under BSE mode using a JSM 7001F JEOL instrument equipped with an Oxford energy dispersive X-ray spectrometer. TEM observations were carried out with a Hitachi H8100 microscope equipped with a ThermoNoran light element energy dispersive X–ray spectrometer and operated at 200 kV. TEM sample preparation involved embedding the as–milled or annealed powders in Gatan G1 epoxy glue, cutting discs with 3 mm diameter, grinding to a thickness of 50 μm and subsequent thinning to electron transparency by argon ion milling using a Gatan–Duo Mill machine, operating at an accelerating voltage of 4 kV, with a 14° incidence angle. The chemically extracted carbon phases were directly observed by TEM on 200–mesh copper grids covered with formvar.

Raman spectroscopy experiments were carried out with a Labram 300 Jobin Yvon spectrometer, equipped with a 17 mW He–Ne laser operating at 632.8 nm. The laser beam is focused with a 50x Olympus objective lens, whose power is varied with a set of neutral density filters of optical densities in the 0.3–2 range. Raw spectra have been treated by linear baseline subtraction and intensity normalization [92].

Microhardness measurements were performed on large particles present in polished metallographic sections of resin-embedded materials. A Shimadzu HMV 2000 hardness tester has been used to apply a load of 0.245 N for 15 s with a Vickers indenter. Average Vickers microhardness values and associated errors were determined from 10 measurements.

Differential thermal analysis has been carried out using a Setaram Setsys Evolution 16/18 DTA/DSC with sample masses in the 70-120 mg range. The experiments were performed with open alumina crucibles under permanent argon flow with heating/cooling rates of 20 $K.min^{-1}$.

2.2.1 Copper-carbon composites

Cu–10nD and Cu–10G composites were prepared by ball milling copper with 10 at.% C, which corresponds to a volume fraction of 5% for nD and 7% for G. A Cu-10 at.% nD mixture has also been milled with 0.1 at.% Cr to produce A Cu–0.1Cr–10nD composite. The Cr atomic fraction used has been previously reported in Ref. [93]. Cr incorporation was carried out by charging the mill with the suitable proportion of a water atomized Cu-2.6 wt% Cr alloy powder [94,95].

A DIN 1.4034 stainless steel mill container was charged with 0.020 kg of the elemental powder mixture and 0.4 kg of 10 mm diameter hardened DIN 1.4034 stainless steel balls. A rotation speed of 400 rpm has been used for milling times of 0.25, 0.5, 1, 2, 4, and 6 h. The Cu–10nD and Cu–10G nanocomposites milled for 4 h have been further annealed for 1h at 773, 873, 973 or 1073 K. The Cu–0.1Cr–10nD mixture has been milled for 4 h and subsequently annealed for 1 h at 873 K. As a control, pristine nD has also been annealed for 1h at 1073 K. All heat treatments have been carried out in a tubular furnace under an argon flow.

Chemical extraction of the carbon phases was carried out by etching the Cu matrix with pure HNO_3 under magnetic stirring (1ml HNO_3:1g composite). The

extracted carbon powder was centrifuged at 3000 rpm with demineralised water and the pellets obtained were subsequently dried at 323 K for 24 h.

Two methods have been tested to consolidate the Cu-carbon nanocomposites: hot extrusion and spark plasma sintering:

- Hot extrusion of a Cu-NbC composite at 873 K resulted in superior densification [96], hence the same temperature has been employed in the present case. Hot extrusion was performed using an INSTRON tensile testing machine, fitted with compression plates. The Cu–10nD material milled for 4 h was encapsulated in a pure copper can and extruded with MoS_2 lubrication through a conical 90º die locally heated by induction. An extruded rod with 6 mm diameter was produced with an area reduction ratio of 7:1.
- Regarding SPS, consolidation at 873 K demonstrated to be ineffective in avoiding porosity [17], thus a temperature of 1073 K has been selected. The Cu–0.1Cr–10nD material milled for 4 h has been exposed to a temperature of 1073 K under a load of 400 MPa for 3 min. The SPS consolidation has been carried out in the National Institute of Advanced Industrial Science and Technology (AIST), Tsukuba, in the framework of a scientific collaboration. The density of the consolidated materials was determined using Archimedes' principle [97,98].

The lattice parameter of the copper matrix was determined using the Cu_{111}, Cu_{200}, Cu_{220}, Cu_{311}, Cu_{400} and Cu_{420} reflections. The average grain diameter of copper was determined through Scherrer equation applied to the highest intensity low angle Bragg's reflection, Cu_{111}. The internal strain effect was determined using the Cu_{111}, Cu_{200}, Cu_{220}, Cu_{311} and Cu_{222} reflections.

The average Cu grain and carbon particle sizes were determined from TEM micrographs of as–milled and heat treated materials with the method described in ref. [99] using the iTEM software package [100]. Due to contrast issues related with the small scale of the microstructure and the heavy deformation of the crystallites, the average Cu grain diameter has been estimated by measuring grains close to a Bragg's condition (i.e. with a dark contrast). The average carbon particle diameter has been determined from the area of particles with clear individual contour assuming a spherical shape.

Milling media contamination in as–milled materials was evaluated from PIXE spectra collected in energy–dispersive mode. The experiments were carried out with 2.0 MeV proton beams of ~3 μm x 3 μm impinging the samples with perpendicular incidence and a Si(Li) detector disposed at 135º relatively to the ion beam direction. A 50 μm mylar foil was used as absorber layer for protective proposes. The integrated intensity of the X–ray peaks and the subsequent quantitative analysis were performed with the AXILV3.0 and DATTPIXE software packages [101,102].

2.2.2 Nickel-carbon composites

Ni–10nD, Ni-20nD, Ni–10G and Ni-20G composites were prepared by ball milling nickel with 10 at.% and 20 at.% C, which correspond to volume fractions of, respectively, 5 and 11 % for nD and 8 and 17% for G.

A DIN 1.4034 stainless steel mill container was charged with 0.020 kg of the elemental powder mixture and 0.4 kg of 10 mm diameter hardened DIN 1.4034 stainless steel balls. Rotation speeds of 200 and 400 rpm and milling times of 0.25, 0.5, 1, 2, 4, 6 and 8 h have been tested. Annealing treatments have been carried out in a tubular furnace under an argon flow for 1h at 973 and 1073 K. Pristine nD has been annealed for 1h at 1073 K as a control. Milling media contamination has been assessed with area and point EDS analyses.

For a detailed analysis of the structural changes induced in the carbon-based phases, the nickel matrix was chemically dissolved by etching the as-milled and heat-treated nanocomposites with pure HNO_3 (3ml HNO_3:1g composite) under magnetic stirring for 24h. The extracted carbon powder was centrifuged at 3000 rpm with demineralized water and the pellet obtained was subsequently dried at 323 K for 24 h.
Nickel lattice parameters were determined using the Ni_{111}, Ni_{200}, Ni_{311}, Ni_{222} , Ni_{400} and Ni_{331}, reflections. The average Ni grain size was determined through Scherrer equation applied to the highest intensity low angle Bragg's reflection, Ni_{111}. The internal strain effect was determined using the Ni_{111}, Ni_{200}, Ni_{220}, Ni_{311} and Ni_{222} reflections.

2.2.3 Tungsten-carbon composites

W–10nD, W-20nD, W–10G and W-20G composites were prepared by ball milling tungsten with 10 at.% and 20 at.% C, which correspond to volume fractions of, respectively, 4 and 11% for nD and 6 and 12% for G. A higher nD fraction (40 at.% C, corresponding to a volume fraction of 19%), has been selected to evaluate the effect of milling energy on carbide formation. Pure milled W has been used as control.

A cemented carbide (WC–6 wt.% Co) mill container was charged with 0.020 kg of pristine powder mixtures and 0.4 kg of 10 mm diameter cemented carbide balls (WC–6 wt.% Co). Rotation speeds of 200, 300 and 400 rpm and milling times of 2 and 4 h have been tested.

The tungsten matrix has been chemically dissolved to allow for a detailed analysis of the structural changes induced in the carbon phase. Chemical extraction has been carried out by etching the milled powder with a mixed solution (10 ml solution:1g composite) of HF (60 % vol. conc.) and HNO_3 (40 % vol. conc.) under magnetic stirring. The extracted particles were centrifuged at 3000 rpm with demineralized water and the pellet obtained was subsequently dried at 323 K for 24 h.

DTA measurements for the W-20nD material milled at 200 rpm for 4 h have been carried out. Moreover, the W-40nD material milled at 200 rpm for 4 h has been consolidated by spark plasma sintering at a temperature of 1073 K and under a load of 400 MPa for 3 min.

2.2.4 Transformation of nanodiamond into onion-like carbon

For this investigation nD has been milled with 20 at.% of Cu, Ni or W. The materials so produced are designated, respectively, as nD(Cu), nD(Ni) and nD(W). A DIN 1.4034 stainless steel mill container was charged with 0.020 kg of the elemental powder mixture and 0.4 kg of 10 mm diameter hardened DIN 1.4034 stainless steel balls. A rotation speed of 200 rpm has been employed and the carbon structural modifications have been studied for milling times of 4h.

Heat exposure has been carried out with DTA experiments up to temperatures varying from 1323-1773 K. The carbon phase transition temperatures were determined with the derivative curves from DTA data [103].

The as-milled and heat-exposed materials have been characterized by XRD and Raman spectroscopy. TEM observations have been carried out by depositing the materials directly on 200-mesh copper grids covered with formvar.

In a parallel study the *in situ* transformation of nanodiamond into onion-like carbon within a Ni-10nD composite has been investigated. The composite was prepared by milling at 200 rpm for 4h and was subsequently heated up to 1673 K at 20 $K.min^{-1}$ in a DTA experiment. The structural changes induced in the carbon phase have been subsequently investigated after extraction of the carbon phase through chemical dissolution of the metallica matrix.

2.3 References

[1] C. Suryanarayana, Prog. Mater. Sci. 46 (2001) 1–184.

[2] J.S. Benjamin, Metall. Trans. B 1 (1970) 2943–2051.

[3] J.S. Benjamin, T.E. Volin, Metall. Trans. B 5 (1974) 1929–1934.

[4] A.E. Ermakov, E.E. Yurchikov, V.A. Barinov, Phys. Met. Metall. 52 (1981) 50–58.

[5] C.C. Koch, O.B. Cavin, C.G. McKamey, J.O. Scarbrough, Appl. Phys. Lett. 43 (1983) 1017–1019.

[6] B.S. Murty, S. Ranganathan, Int. Mater. Rev. 43 (1998) 101–141.

[7] L. Lü, M.O. Lai Mechanical Alloying, Kluwer Academic Publishers, Springer, 1998.

[8] C.C. Koch, Mat. Sci. Eng. A 244 (1998) 39–48.

[9] J.S. Benjamin, Mater. Sci. Forum 88-90 (1992) 1–18.

[10] H.J. Fecht, E. Hellstern, Z. Fu, W. L. Johnson, Metall. Mater. Trans. A 21 (1990) 2333–2337.

[11] J.S. Benjamin, Sci. Am. 234 (1976) 40–48.

[12] R.M. Davis, C.C. Koch, Scripta Metall.21 (1987) 305–310.

[13] E. Gaffet, M. Abdellaoui, N. Malhouroux-Gaffet, Mater. Trans., JIM 36 (1995) 198–209.

[14] http://www.retsch.com/

[15] D. Gu, Y. Shen, Appl. Surface Sci. 256 (2009) 223–230.

[16] K. Aoki, A. Memezawa, T. Masumoto, Mater. Sci. Eng. A 181–182 (1994) 1263–1267.
[17] D. Nunes, V. Livramento, J.B. Correia, K. Hanada, P.A. Carvalho, R. Mateus, N. Shohoji, H. Fernandes, C. Silva, E. Alves, E. Ōsawa, Mater. Sci. Forum 636 (2010) 682–687.
[18] A.V. Gubarevich, S. Usuba, Y. Kakudate, A. Tanaka, O. Odawara, Diamond Relat. Mater. 14 (2005) 1549–1555.
[19] H.E. Rose, R.M.E. Sullivan, A Treatise on the Internal Mechanics of Ball, Tube and Rod Mills, Constable, London, 1957.
[20] J.S.C. Jang, C.C. Koch, J. Mater. Res. 5 (1990) 498–510.
[21]Y. Chen. R. Le Hazif, G. Martin, Mater. Sci. Forum 88-90 (1992) 35–42.
[22] R.B. Schwarz, C.C. Koch, Appl. Phys. Lett. 49 (1986) 146–148.
[23] L. Lu, M.O. Lai, Mater. Des. 16 (1995) 33–39.
[24] R. Chaim, Mater. Sci. Eng. A 443 (2007) 25–32.
[25] U. A.Tamburini, J.E. Garay, Z.A. Munir, Scripta Mater. 54 (2006) 823–828.
[26] K. Hanada, K. Yamamoto, T. Taguchi, E. Ōsawa, M. Inakuma, V. Livramento, J.B. Correia, N. Shohoji, Diamond Relat. Mater. 16 (2007) 2054–2057.
[27] V. Livramento, J.B. Correia, D. Nunes, P.A. Carvalho, H. Fernandes, IAEA Technical Meeting on Research Using Small Fusion Devices. AIP Conference Proceedings 996 (2008) 166–171.
[28] M. Omori, Mater. Sci. Eng. A 287 (2000) 183–188.
[29] M. Tokita, Mechanism of Spark Plasma Sintering (SPS), Sumitomo Coal Mining Company, Ltd., Japan.
[30] http://world.intellectualprops.com/chemistry/transparent-ceramics-magnesium-alumnate/
[31] H. Kronberger, Proc. Roy. Soc. A 311 (1969) 331–347.
[32] http://www.efunda.com/processes/metal_processing/extrusion.cfm
[33] http://industrialextrusionmachinery.com/extrusion_process_hot_extrusion.html
[34] C. Hammond, The basics of crystallography and diffraction, OUP/International Union of Crystallography, 2nd edition, Oxford University Press, 2001.
[35] http://203.199.213.48/1745/1/x_ray_diffraction.pdf
[36] B.E. Faulkner, J. Russell, High Performance Pigments, Wiley-VCH, 2nd edition, 2009.

[37] B.D. Cullity, Elements of X Ray Diffraction, 2nd edition, Addison-Wesley Publishing Company, 1978.
[38] http://xdb.lbl.gov/Section1/Sec_1-2.html
[39] D.Brandon, W.D.Kaplan, Microstructural charecterization of materials, John Wiley and sons, Chichester, 1999.
[40] Z. Zhao, V. Buscaglia, M. Viviani, M. T. Buscaglia, L. Mitoseriu, A. Testino, M. Nygren, M. Johnsson, P. Nanni, Phys. Rev. 70 (2004) 024107-1/8.
[41] C.B. Ferrer, S.P. Esclapez, D. L.Castelló, A.B. López, J. Rare Earths 28 (2010) 647–653.
[42] http://www.mpip-mainz.mpg.de/~andrienk/journal_club/xray.pdf
[43] V. Ciupină, S. Zamfirescu, G. Prodan, Nanotechnology – toxicological issues and environmental safety, NATO Security through Science Series (2007) 231–237.
[44] G.K. Williamson, W.H. Hall, Acta Metall. 1 (1953) 22–31.
[45] M. Hosokawa, K. Nogi, M. Naito, T. Yokoyama, Nanoparticle Technology Handbook, Elsevier, Amsterdam, 2007.
[46] B. Fultz , J.M. Howe, Transmission Electron Microscopy and Diffractometry of Materials, 3rd ed., Springer, Berlin-Heidelberg, 2008.
[47] Y. Waseda, E. Matsubara, K. Shinoda X-ray Diffraction Crystallography: Introduction, Examples and Solved Problems, Springer, New York, 2011.
[48] http://science.howstuffworks.com/scanning-electron-microscope2.htm
[49] J.I. Goldstein, D.E. Newbury, P. Echlin, D.C. Joy, C. Fiori, E. Lifshin, Scanning Electron Microscopy and X-ray Microanalysis, Plenum Press, New York, 1981.
[50] http://www.ccber.ucsb.edu/research/esau/topics-of-study/microscopes/
[51] D.B. Williams, C.B. Carter, Transmission Electron Microscopy: A textbook for Materials Science, Plenum Press, New York, 1996.
[52] http://www.mete.metu.edu.tr/pages/tem/TEMtext/TEMtext.html
[53] S. Cronjé, TEM Investigation of Rapidly Deformed Cu and Mo Shaped Charge Liner Material, Dissertation of University of the Free State Republic of South Africa, 2007.
[54] http://www2.rgu.ac.uk/life_semweb/xray.html
[55] A.U. Hamid, H.M. Tawancy, A.I. Mohammed, S.S. Al-Jaroudi, N.M. Abbas, Mater. Charact. 56 (2006) 192–199.

[56] G. Remond, C. Gilles, D. Isabelle, C. Choi, M. Azahra, O. Rouer, F. Cesbron, Appl. Radiat. Isot. 46 (1995) 563–570.

[57] G.W. Grime, Nucl. Instr. Meth. B, 109–110 (1996) 170–174.

[58] IAEA Manual, Instrumentation for PIXE and RBS, Austria, 2000.

[59] J.R. Ferraro, K. Nakamoto, C.W. Brown, Introductory Raman Spectroscopy, 2nd ed. Elsevier, 2003.

[60] S. Garoff, B. Liokkala, Characterizing molecular vibrations using Raman Spectroscopy, Carnegie Mellon University, 2011.

[61] http://www.geo.uib.no/bgf/index.php/raman/ramantech

[62] http://www.wiley-vch.de/books/sample/3527405062_c01.pdf

[63] S.A. Solin, K. Ramdas, Phys. Rev. B 1 (1970) 1687–1698.

[64] J. Qian, C. Pantea, J. Huang, T.W. Zerda, Y. Zhao, Carbon 42 (2004) 2691–2697.

[65] W. Zhu, C.A. Randall, A.R. Badzian, R. Messier, J. Vac. Sci. Technol. A 7 (1989) 2315–2324.

[66] R.J. Nemanich, J.T. Glass, G. Lucovsky, R.E.Shroder, J. Vac. Sci. Technol. A6 (1988) 1783–1785.

[67] L. Fayette, B. Marcus, M. Mermoux, L. Abello, G. Lucazeau, Diamond Relat. Mater. 3 (1994) 438–442.

[68] F. Tuinstra, J.L. Koenig, Chem. J. Phys. 53 (1970) 1126–1130.

[69] M.T. Marques, J.B. Correia, O. Conde, Scripta Mater. 50 (2004) 963–967.

[70] Y. Kawashima, G. Katagiri, Phys. Rev. B 52 (1995) 10053–10059.

[71] T.D. Shen, W.Q. Ge, K.Y. Wang, M.X. Quan, J.T. Wang, W.D. Wei, C.C. Koch, Nanostructured Mater. 7 (1996) 393–399.

[72] M. Yoshikawa, G. Katagiri, H. Ishida, A. Ishitani, Solid Stat. Comm. 66 (1988) 1177–1180.

[73] G. Zamfirova, A. Dimitrova, Polymer Testing 19 (2000) 533–542.

[74] G.V. Voort, R. Fowler, Obtaining Consistent Vickers Hardness at Loads ≤ 100 Grams Force, Microscopy and Microanalysis (2011) 1040-1041.

[75] G.F.V. Voort, Metallography, principles and practice, ASM International, Ohio, 1999.

[76] G.F.V. Voort, G.M. Lucas, Microindentation Hardness Testing. Adv. Mater. Proc. 154 (1998) 21–25.

[77] C. Chuenarrom, P. Benjakul, P. Daosodsai, Mater. Res. 12 (2009) 473-476.

[78] D. Tabor, The Hardness of Metals, Oxford University Press, New York, 1951.

[79] G.E. Dieter, Mechanical Metallurgy, 3rd ed., Mc Graw-Hill Book Co., New York 1986.

[80] J.T. Busby, M.C. Hash, G.S. Was, J. Nuclear Mater. 336 (2005) 267–278.

[81] L. Prandtl, Nachr. Ges. Wiss. Gottingen. (1920) 74.

[82] T. Hatakeyama, F.X.Quin, Thermal Analysis, Fundamentals and Applications to Polymer Science, 2nd Edition, Wiley, England, 1999.

[83] H.K.D.H. Bhadeshia, Thermal analyses techniques. Differential thermal analysis, University of Cambridge, Materials Science& Metallurgy.

[84] http://www.siint.com/en/products/thermal/tec_descriptions/dta.html

[85] W.J. Boettinger, U.R. Kattner K.W. Moon, J.H. Perepezko, DTA and Heat-flux DSC Measurements of Alloy Melting and Freezing, special Publications, Washington, 2006.

[86] A. Krüger, M. Ozawa, F. Kataoka, M. Ozawa, T. Fujino, Y. Suzuki, A.E. Aleksenskii, A.Y. Vul', E. Ōsawa, Carbon 43 (2005) 1722–1730.

[87] E.D. Eidelman, V.I. Siklitsky, L.V. Sharonova, M.A. Yagovkina, A.Y. Vul, M. Takahashi,M. Inakuma, M. Ozawa, E. Ōsawa, Diamond Relat. Mater. 14 (2005) 1765–1769.

[88] Q. Zou, Y.G. Li, B. Lv, M.Z.Wang, L.H. Zou,Y.C. Zhao, Inorganic. Mater. 46 (2010) 127–131.

[89] V. Livramento, J.B. Correia, N. Shohoji, E. Ōsawa, Diamond Relat. Mater. 16 (2007) 202–204.

[90] H. Shi, J. Barker, M.Y. Saïdi, R. Koksbang, L. Morris, J. Power Sources 68 (1997) 291–295.

[91] W. Krauss, G. Nolze, J. Appl.Cryst.29 (1996) 301–303.

[92] J.R. Ferraro, K. Nakamoto, C.W. Brown, Introductory Raman Spectroscopy, 2nd ed. Elsevier, 2003.

[93] L. Weber, R. Tavangar, Scripta Mater. 57 (2007) 988–991.

[94] J.B. Correia, H.A. Davies, C.M. Sellars, Acta Mater. 45 (1997) 177–190.

[95] D. Nunes, J.B. Correia, P.A. Carvalho, N. Shohoji, H. Fernandes, C. Silva, L.C. Alves, K. Hanada, E. Ōsawa, Fusion Eng. Design. 86 (2011) 2589–2592.

[96] M.T. Marques, J.B. Correia, R. Vilar, Rev. Adv. Mater. 18 (2008) 403–407.

[97] V. Livramento, D. Nunes, J.B. Correia, P.A. Carvalho, U. Mardolcar, R. Mateus, K. Hanada, N. Shohoji, H. Fernandes, C. Silva, E. Alves, J. Nuclear Mater. 416 (2011) 45–48.

[98] P. Jenei, E.Y. Yoon, J. Gubicza, H.S. Kim, J.L. Lábár, T. Ungár, Mater. Sci. Eng. A 528 (2011) 4690–4695.

[99] American Society for Metals, G.F.V. Voort, ASM International Handbook Committee.ASM handbook: Metallography and Microstructures, volume 9, ASM International, 2004.

[100] Information on http://www.soft-imaging.net/

[101] P. Van Espen, K. Janssens, I. Swentens, AXIL, X-ray Analysis Software - User Manual, Canberra Packard, Benelux, 1986.

[102] M.A. Reis, L.C. Alves, A.P. Jesus, Nucl. Instr. Meth. B 109/110 (1996) 134–138.

[103] W.J. Boettinger, U.R. Kattner, K.W. Moon, J.H.Perepezko, DTA and Heatflux DSC Measurements of Alloy Melting and Freezing, Special Publications, Washington; 2006.

Chapter 3

Chapter 3 – Copper-carbon composites

3.1 Introduction

In the present chapter nanodiamond and graphite have been milled with copper to produce Cu–10nD and Cu–10G composites. Cr has also been incorporated to produce a Cu–0.1Cr–10nD composite. Heat treatments in the 773-1073 K temperature range have been performed to evaluate the nanocomposites thermal stability. As–milled composites have been consolidated by hot extrusion and spark plasma sintering. Structural changes induced by high-energy milling, annealing and consolidation have been investigated by X–ray diffraction, electron microscopy and Raman spectroscopy. Contamination in as–milled materials has been monitored through proton-induced X–ray emission spectroscopy and energy dispersive X-ray spectroscopy. The copper matrix has been chemically dissolved to allow for a detailed analysis of the structural changes induced in the carbon-based phases. The effect of milling time and heat treatment temperature on copper grain size has been quantitatively assessed. The strength level and thermal stability have been evaluated through microhardness tests. Strengthening mechanisms and the load transfer ability to reinforcement particles are discussed.

3.2 Results and discussion

Cu–10nD and Cu–10G composites were prepared by ball milling at a rotation speed of 400 rpm, a well-established parameter for Cu milling [1-3], for milling times of 0.25, 0.5, 1, 2, 4, and 6 h. The Cu–10nD and Cu–10G nanocomposites milled for 4 h have been further annealed for 1h at 773, 873, 973 or 1073 K. As a control, pristine nD has also been annealed for 1h at 1073 K. A Cu–0.1Cr–10nD mixture has been milled for 4 h and subsequently annealed for 1 h at 873 K.

The present work was focused on the production of metal-carbon nanocomposites by ball milling, nevertheless some consolidation work has been carried out in order to

assess the viability of the full processing route. The Cu–10nD material milled for 4 h has been consolidated by hot extrusion at 873 K while the Cu–0.1Cr–10nD material milled for 4 h has been consolidated by SPS at 1073 K.

X-rays diffractograms

The intense copper reflections, and the corresponding background level, obscured the carbon peaks in the XRD data obtained from the Cu–10nD and Cu–10G composites. As a result, the structural changes induced in the carbon phases could only be evaluated after Cu extraction.

Figure 3.1 shows diffractograms obtained from nD (a) and G (c) powders extracted respectively from as-milled Cu-10nD and Cu-10G (4 h) composites and pristine nD and G powders (respectively, (c) and (d)).

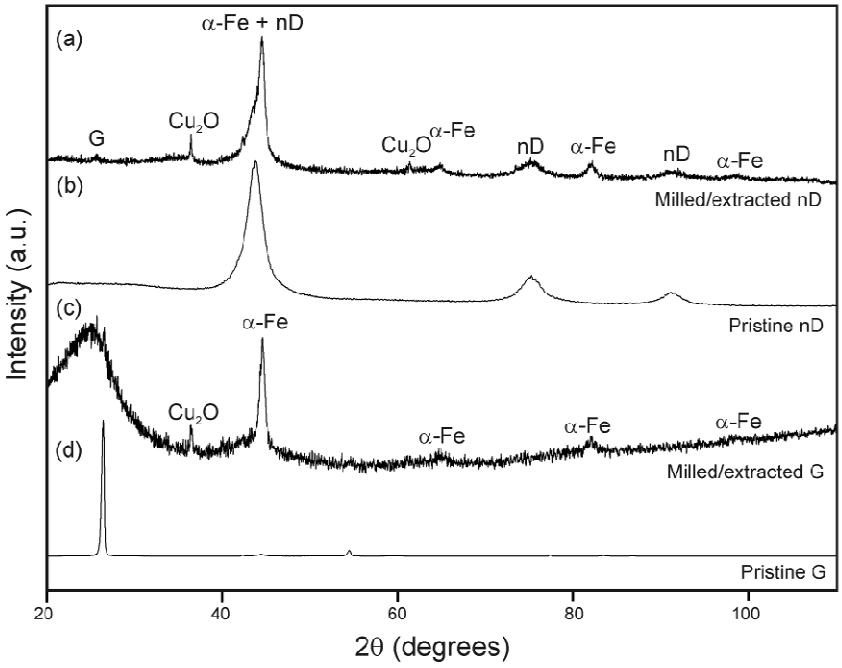

Figure 3.1. Experimental X-ray diffractograms of milled/extracted nD (a), pristine nD (b), milled/extracted G (c), and pristine G powders (d).

The α-Fe peaks in Figure 3.1 resulted from milling media contamination, whereas Cu_2O is likely to have originated from residual oxidation of the original copper powder. The peaks at 44°, 75° and 92° in the milled/extracted nD diffractogram (a) can be indexed to nD, although the highest intensity peak is convoluted with the α–Fe_{110} reflection. The minor graphite$_{002}$ peak at 26° in (a) is not present in the diffractogram of the pristine nD in (b) although a similar peak has been reported for detonation nanodiamond [4,5]. In the case of the milled/extracted G in (c), the broad band suggests extensive amorphization in agreement with a report by Shen *et al.* [6], who demonstrated that a mixture of nanocrystalline graphite and amorphous carbon is produced during high-energy milling of pure graphite, with higher amorphization occurring for increased milling time. The present results point to a preservation of the carbon-based phases during the Cu dissolution process, as previously reported by Shao *et al.* [7]. SEM/EDS analyses showed that the remaining Cu after dissolution was below 2 at.% (part of which in Cu_2O form).

The present XRD results demonstrate that, contrarily to the G behavior, nD preserves crystallinity during high-energy milling, which to the author's best knowledge has not been described before.

Microstructural observations and elemental analysis

Figure 3.2 presents representative microstructures of Cu–10nD (a) and Cu–10G (b) composite powders milled for 4 h, together with the microstructures of the same materials heat-treated at 873 K (c) and 973 K (d). Figure 3.3 presents representative microstructures of the Cu–0.1Cr–10nD powder milled for 4 h (a) and the same material heat-treated at 873 K (b). The carbon particles are readily identifiable by the brighter contrast resulting from the low atomic number.

The as–milled microstructures display fine Cu grains with mottled contrast and ill-defined boundaries, characteristic of high–energy non–equilibrium states induced by intense deformation (Figures 3.2 (a) and (b), and Figure 3.3 (a)). The carbon-rich particles, with diameters in the 5–20 nm range, are uniformly dispersed in the metallic matrices and are frequently localized at Cu grain boundaries. This phenomenon is

associated with the cold welding processes occurring at the many deformation events that produce convolutions and Cu subgrain recombinations [8]. In the case of the Cu–10G material (Figure 3.2 (b)) the particles presented higher aspect ratios owing to the intense localized deformation imposed on the relatively softer carbon phase. Both as–milled nanocomposites exhibited apparent bonding at the Cu/carbon interfaces suggesting a potentially efficient load transfer.

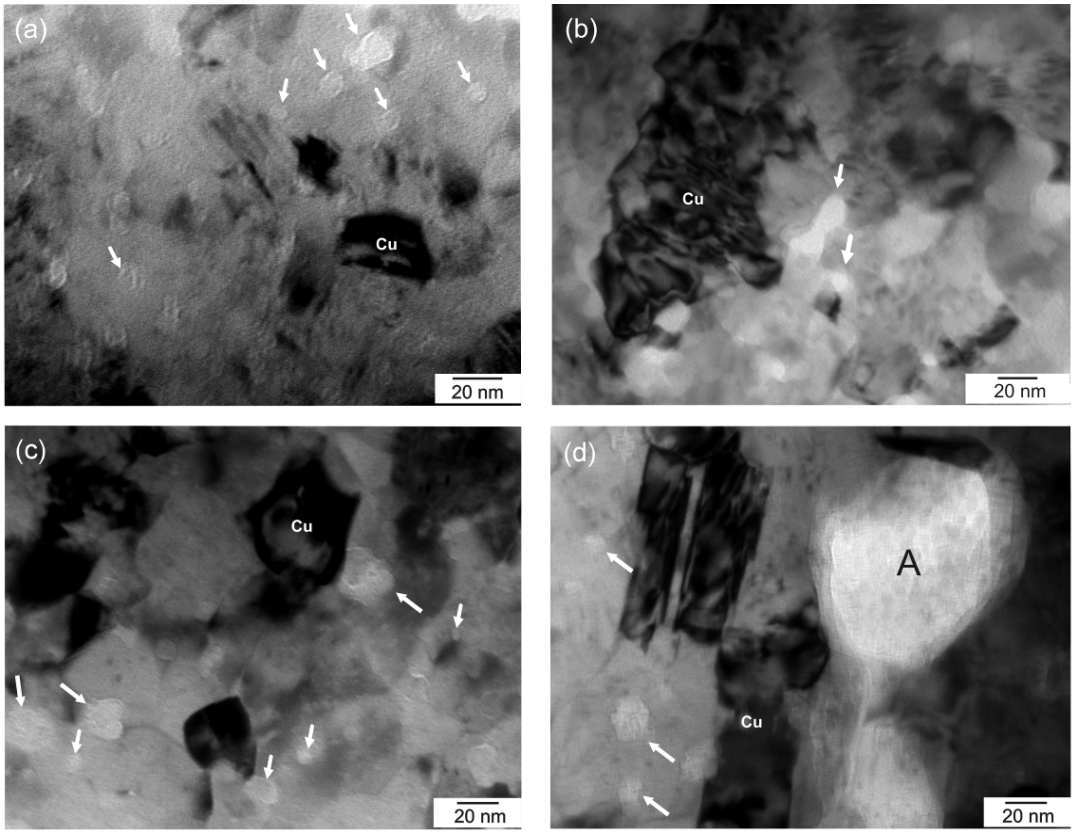

Figure 3.2. Bright–field TEM images of Cu–10nD (a) and Cu–10G (b) composites milled for 4 h. Cu–10nD composites milled for 4 h and heat-treated at 873 K (c) and 973 K (d). The arrows indicate low–Z contrast regions. The A in (d) indicates a large carbon-rich region.

Table 3.1 shows the content of exogenous elements in the Cu–10nD and Cu–10G as-milled materials as determined by proton-induced X–ray emission spectroscopy and energy dispersive X-ray spectroscopy. The chief impurities are Fe and Cr, present with a ratio comparable to the Cr/Fe = 0.159 of the DIN 1.4034 stainless steel used as milling media [9]. The overall contamination remained below 0.7 wt.%, which can be considered low taking into account the relatively high milling energy employed. Significantly higher

contamination was expected for the Cu–10nD composites, owing to the high hardness of the carbon allotrope. However, the results demonstrate that, at the nanoscale, diamond produces minimal wear of the milling media, in agreement with a reported self-lubrication mechanism [10]. The Cu–0.1Cr–10nD composite exhibited a Cr/Fe ratio of 0.218, which exceeded the ratio of the milling media steel due to Cr incorporation in the mill charge. The data presented in Table 3.1 demonstrate that the values obtained by EDS are similar to the concentrations established by PIXE.

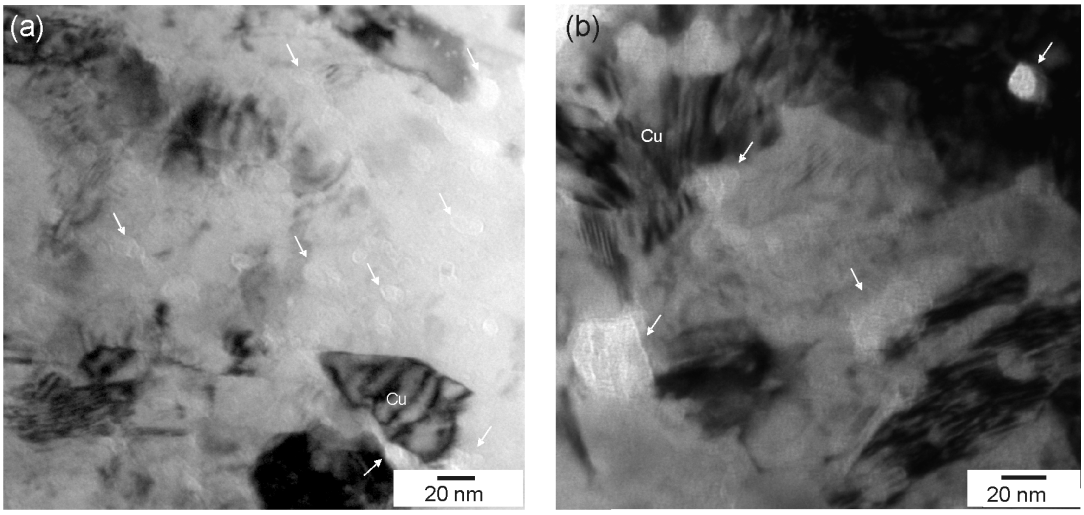

Figure 3.3. Bright–field TEM images of the Cu–0.1Cr–10nD composite milled for 4 h (a) and Cu–0.1Cr–10nD composite milled for 4 h and heat-treated at 873 K (b). The arrows indicate low–Z contrast regions.

Table 3.1. Milling media contamination of as–milled materials evaluated by PIXE and EDS.

Condition	Fe (wt.%) PIXE	Cr (wt.%) PIXE	Ca (wt.%) PIXE	Ti (wt.%) PIXE	Cu (wt.%) PIXE	Fe (wt.%) EDS
as–milled Cu–10nD (4 h)	0.55	0.09	0.01	0.01	99.34	0.47
as–milled Cu–10G (4 h)	0.52	0.08	0.01	0.01	99.38	0.71
as–milled Cu–0.1Cr–10nD (4 h)	0.55	0.12	-	-	99.33	-

The heat treatments resulted in modest Cu grain growth in the Cu–10nD and Cu–0.1Cr–10nD composites, with the metallic matrix remaining nanostructured after annealing (see Figure 3.2 (c) and Figure 3.3 (b)). Moderate coarsening was also observed for the carbon particles. However, for the Cu–10nD composite, a striking

dispersion in particle size was apparent in the materials treated at the highest temperatures (973K and 1073K). These materials exhibited carbon particles with sizes comparable to the as–milled ones (see arrows in Figure 3.2 (d)) together with large low–Z regions (see A in Figure 3.2 (d)).

Figure 3.4 presents micrographs of nD (a) and G (c) powders extracted respectively from as-milled Cu-10nD and Cu-10G composites. The milled/extracted nD presented individual particles with diameters in the 5–20 nm range, whereas a fairly homogeneous carbon-based phase was observed for the milled/extracted G. Ring diffraction patterns attested for the crystallinity of the milled/extracted nD (c), while the diffuse halo observed for the milled/extracted G (d) suggests an essentially amorphous carbon phase. Fe(Cr)–rich inclusions were detected in both materials, although they were more discernible in the milled/extracted G due to the absence of diffraction contrast in the carbon phase. An α–Fe(Cr) ring could be indexed in (d). Overlapping with an intense nD reflection (see Figure 3.1 (a)) hindered the detection of this α–Fe(Cr) ring in (b).

Figure 3.5 shows micrographs of nD extracted from annealed Cu-10nD composites ((a) to (d)). Individual particles with diameters essentially in the 5–20 nm range were observed for annealing temperatures up to 873 K (Figure 3.5 (a) and (b)). For higher annealing temperatures the milled/annealed/extracted materials presented also larger particles (Figure 3.5 (c) and (d)) that correspond to regions such as A in Figure 3.2 (d).

The growth mechanism of the carbon particles in the Cu-10nD composites during annealing is worth discussing. At moderate annealing temperatures diamond is very stable and small particles are not likely to dissolve in order to incorporate larger ones (a similar behavior has been reported for Zirconia dispersoids in a platinum matrix [11]). In addition, diamond is not expected to grow under atmospheric pressure. Therefore coarsening of nanodiamond through a diffusional Ostwald ripening mechanism could not have occurred. On the other hand, at higher annealing temperatures the nanodiamond tends to amorphize [12] and this phase transformation facilitates dissolution. The observed increase in particle size seems hence to have occurred with amorphous carbon, through a precipitate growth regime until C supersaturation in the Cu matrix dropped close to its equilibrium value (0 at.%), at which time a coarsening Ostwald ripening regime took over. The nD growth phenomenon is thus associated with a phase

transformation, which has operated essentially during the heat treatments at 973 K and 1073 K (see Figure 3.5). This transformation has been hastened by the prior milling operation, since pristine (non-milled) nD powder annealed at 1073 K consisted of particles with diameters in the 5-20 nm range (Figure 3.5 (e)) that presented essentially the diamond structure, as demonstrated by ring electron diffraction patterns (Figure 3.5 (f)).

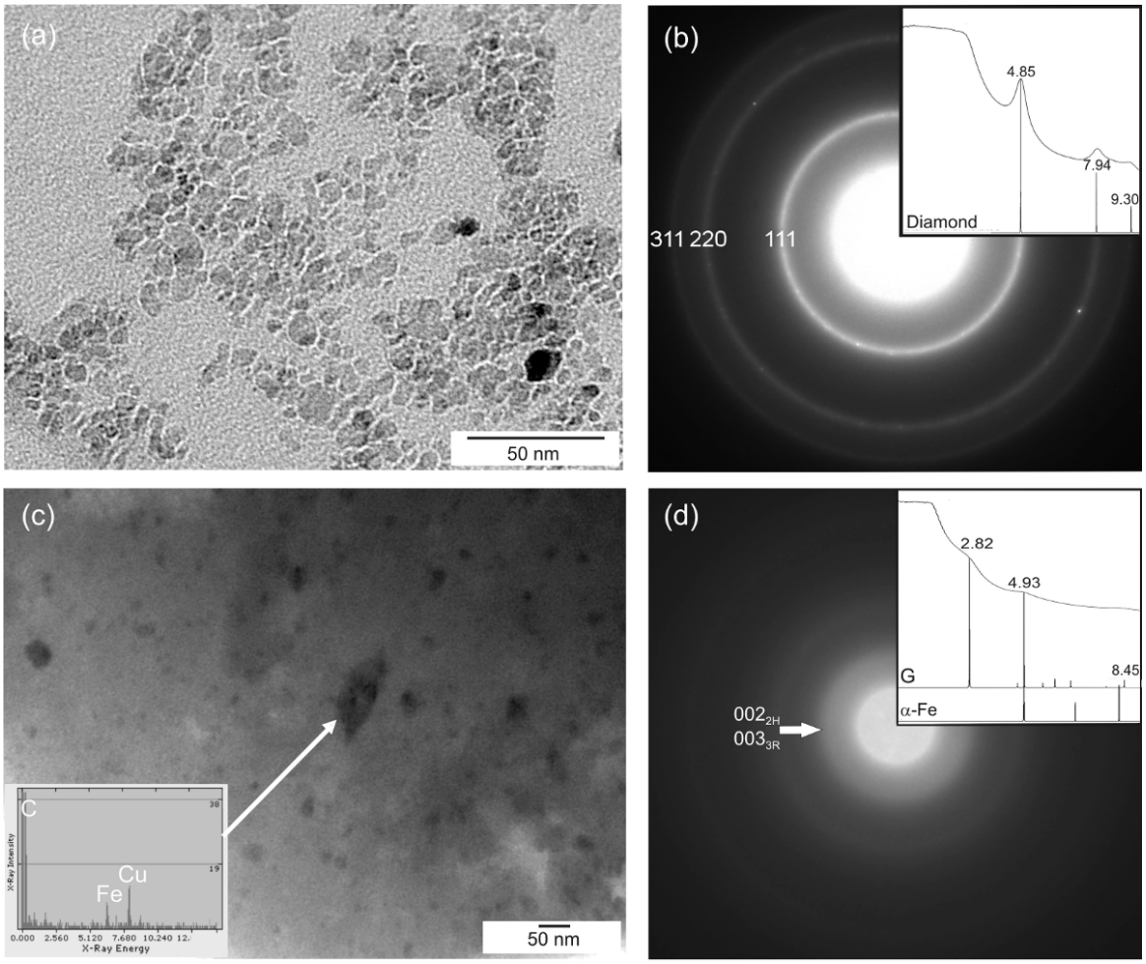

Figure 3.4. (a) Bright–field TEM image of the milled/extracted nD powder. (b) Ring diffraction pattern obtained from a large area similar to (a) with integrated radial profile (diamond simulation included with legend in nm^{-1}). (c) Bright–field TEM image of the milled/extracted G powder with EDS point analysis (the TEM grid contributed to the Cu peak). (d) Ring diffraction pattern obtained from a large area similar to (c) with integrated radial profile (graphite and α–Fe simulations included with legend in nm^{-1}).

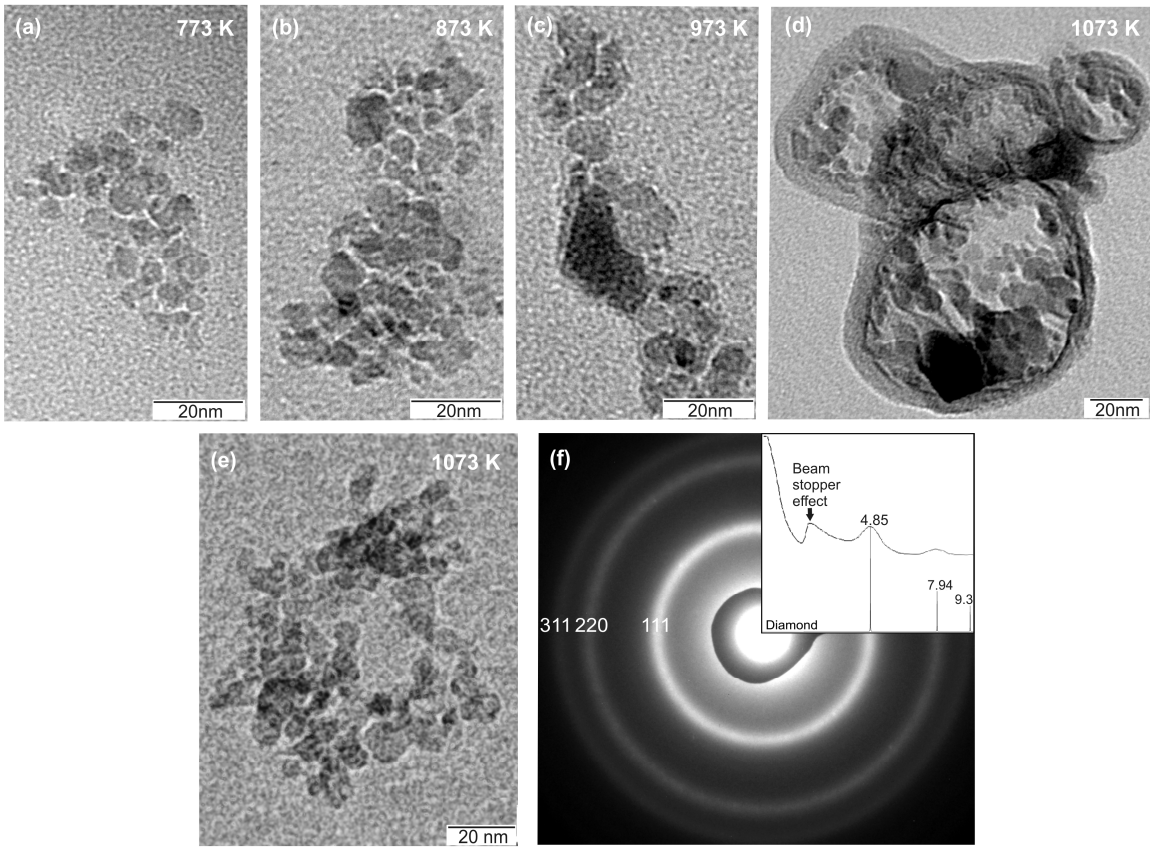

Figure 3.5. Bright–field TEM images of milled/annealed/extracted materials nD: (a) 773 K, (b) 873 K, (c) 973 K and (d) 1073 K. (e) Pristine nD powder annealed at 1073 K, and (f) ring diffraction pattern obtained from a large area similar to (e) with integrated radial profile (diamond simulation included with legend in nm^{-1}).

Micro-Raman spectroscopy

Figure 3.6 shows Raman spectra of milled/extracted and pristine nD (a); milled/extracted and pristine G (b); milled/annealed/extracted nD annealed at different temperatures (c); and milled/annealed/extracted G annealed at different temperatures (d).

The spectrum of milled/extracted nD is similar to that of pristine nD showing that the material remains stable during high-energy milling. Both spectra in Figure 3.6 (a) present a band in the 1150–1200 cm^{-1} region, a major peak at ~1320 cm^{-1} and a broad band ranging from 1400 to 1700 cm^{-1}. The band at 1150–1200 cm^{-1} is likely to correspond to

Trans-polyacetylene, that exhibits Raman peaks at 1125 cm^{-1} and 1480 cm^{-1} [13] and has been reported to exist in nD produced by different routes [14–17].In agreement with the diffraction studies (see Figures 3.1 (a) and 3.4 (b)), the peak at ~1320 cm^{-1} corresponds to structural sp^3 vibrations and the observed downshift (~10 cm^{-1}) is related to phonon confinement in nanoscale particles [18,19].The broad band at 1400-1700 cm^{-1} is probably a convolution of a 1480 cm^{-1} *Trans*-polyacetylene peak and an sp^2 Raman peak originating from the outer graphite-like layers that envelope the diamond cores of nD powder [20,21].

The spectrum of pristine synthetic graphite powder (Figure 3.6 (b)) presents a major peak at 1580 cm^{-1} (G) and two bands at 1270-1370 cm^{-1} (D) and 1610–1620 cm^{-1} (D′). The milled/extracted G material shows an intense D-band at 1200–1430 cm^{-1} and convoluted G and D′ bands at 1500–1700 cm^{-1}. A single broad asymmetric band corresponding to fully amorphous carbon was not observed [6,22]. Nevertheless, the Raman spectra evolution indicates that during milling G becomes a mixture of residual sp^2 clusters with amorphous carbon.

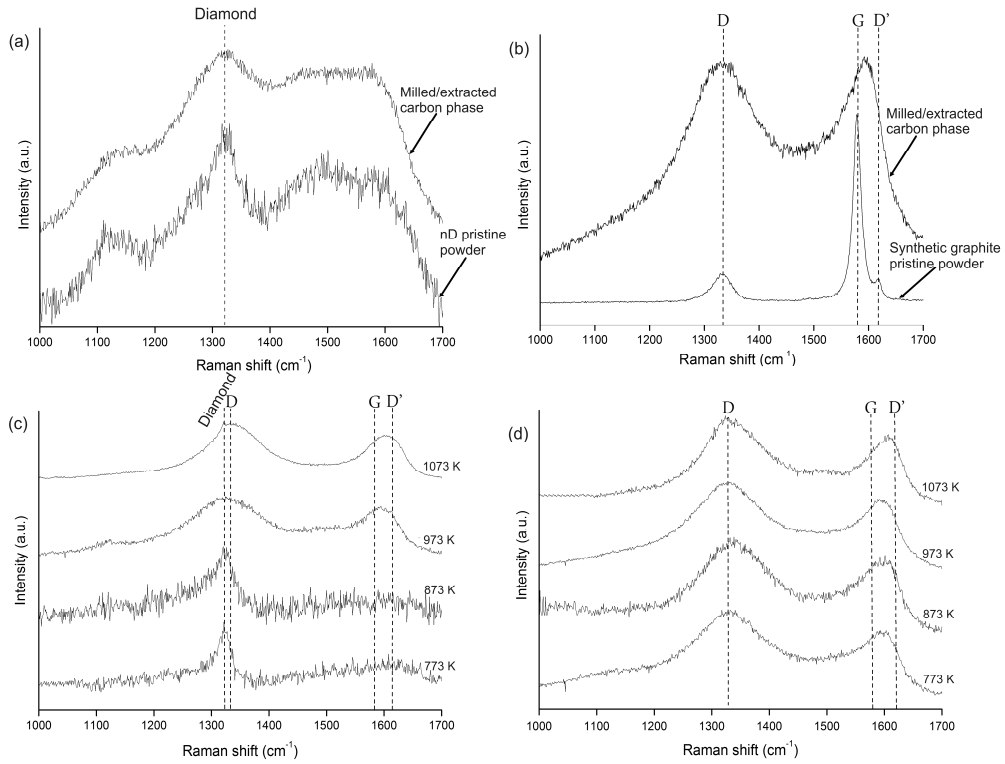

Figure 3.6. Raman spectra of milled/extracted and pristine nD (a) and milled/extracted and pristine G (b). Milled/annealed/extracted nD (c) and milled/annealed/extracted G (d) at several annealing temperatures.

The Raman spectra of the milled/annealed/extracted nD materials (Figure 3.6 (c)) indicate that *Trans*-polyacetylene evaporates during the heat–treatments (as inferable from the absence of bands at ~1125 cm^{-1} and 1480 cm^{-1}, compare with Figure 3.6 (a)). At the highest temperatures, the well defined band at ~1600 cm^{-1} points to a progressive increase of sp^2 clusters, furthermore, the 1250–1400 cm^{-1} signal represents an overlap of the diamond and graphite D bands. A well-defined ~1600 cm^{-1} band appeared at 973 K, a lower temperature than the 1173 K [23] and the 1273 K [18] previously reported for annealed (pristine) nD. The observed behavior suggests therefore that amorphization of nD during annealing is facilitated by the structural defects induced by high-energy milling.

The Raman spectra of the milled/annealed/extracted G materials (Figure 3.6 (d)) remained essentially unchanged with the heat–treatments, except for an upshift of the ~1600 cm^{-1} band which is consistent with a higher degree of disorder for the highest annealing temperatures. Full graphitization of the amorphous material would require temperatures above 2273 K [6].

Consolidated materials

The samples consolidated by hot extrusion at 873 K and by SPS at 1073 K exhibited, respectively, a densification of 99% and 96%, as determined by Archimedes' principle. Figure 3.7 shows representative microstructures of the Cu–10nD composite milled for 4 h and consolidated by hot extrusion and of the Cu–0.1Cr–10nD composite milled for 4 h and consolidated by SPS.

The presence of pores in the Cu–10nD hot extruded material could not be detected by SEM (Figure 3.7 (a)). The absence of porosity was confirmed by TEM observation (Figure 3.7 (b)), and the interfaces between the carbon particles and the copper matrix pointed to bonding between the two phases. The low-Z contrast carbon particles exhibited sizes typically in the 10-50 nm range, showed equiaxed morphologies, were uniformly dispersed and were frequently localized at the grain boundaries of the Cu matrix, which presented a grain size in the 50–100 nm range (Figure 3.7 (b)). The dynamic

recrystallization processes occurring during hot extrusion induced the presence of subgrains, as well as a high number of twins (Figure 3.7 (b)).

The microstructure of the Cu–0.1Cr–10nD consolidated material (Figure 3.7 (c)) showed pure Cu layers at the prior powder boundaries (ppb): SPS induced melting at the surface layers, which segregated carbon but were able to bond the powder particles. The presence of pores, albeit with a low volume fraction could be detected by SEM (Figure 3.7 (c)). TEM micrographs showed that in the central regions of the prior powder particles the metallic matrix remained nanostructured with Cu grain sizes in the 100–200 nm range (Figure 3.7 (d)). The low-Z contrast carbon particles exhibited sizes typically in the 20-100 nm range, showed equiaxed morphologies, were uniformly dispersed and were frequently localized at grain boundaries of the Cu matrix (Figure 3.7 (b)).

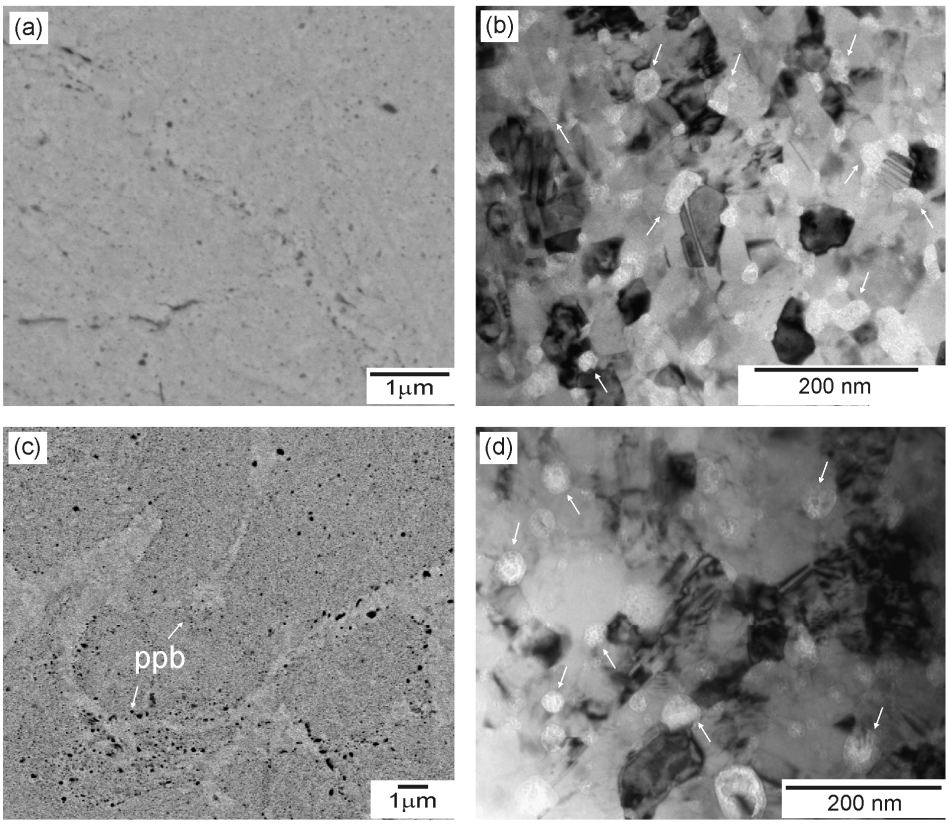

Figure 3.7. (a) BSE SEM image and (b) bright–field TEM image of the Cu–10nD material milled for 4 h and subsequently consolidated by hot extrusion at 873 K. (c) BSE SEM image and (d) bright–field TEM image of the Cu–0.1Cr–10nD material milled for 4 h and subsequently consolidated by spark plasma sintering at 1073 K. The arrows in (c) indicate the prior powder boundaries, while in (b) and (d) indicate the low–Z contrast regions.

Densification is highly dependent on the consolidation route [24,25]. The present results demonstrate that high densification is attainable with both consolidation techniques, although the porosity level is lower for the former. Furthermore, the microstructural heterogeneity observed with SPS, i.e., pure Cu at the ppb and composite central regions, is likely to embrittle the materials rendering hot extrusion a preferable consolidation method.

The Cu grain size of the hot extruded material is comparable to the one of Cu–10nD milled/annealed material at 873 K (compare Figures 3.2 (c) and 3.7 (b)). The SPS material exhibited a bimodal grain size distribution (see Figure 3.7 (d)), which has not been detected in the annealed materials. Nevertheless, both consolidation techniques efficiently prevented excessive Cu grain grown. In analogy with the Cu–10nD and Cu–0.1Cr–10nD annealed materials (Figures 3.2 (d) and 3.3 (b)), the coarsening of carbon particles observed in both consolidated materials (Figure 3.7 (b) and (d)) must have involved a prior amorphization of nanodiamond [12]. As expected, the composite extruded at 873 K exhibited lower carbon coarsening than the material consolidated by SPS at 1073 K as a result of the lower processing temperature, especially in view of the fact that at 873 K the diamond structure is largely preserved as opposed to 1073 K (see Figure 3.6 (c)).

Microstructural stability

Figure 3.8 presents the evolution of the Cu grain diameter (Scherrer equation) with milling time for Cu–10nD and Cu–10G composites (a), as well as the evolution of the Cu grain diameter (TEM measurements and Scherrer equation) and nD particle diameter (TEM measurements) with annealing temperature (respectively, (b) and (c)).

The Cu grain size decreased considerably with milling time up to 2 h for both types of nanocomposites, albeit more effectively for Cu–10nD which showed clear grain size stabilization after 2 h of milling (Figure 3.8 (a)). The consistently lower grain sizes achieved for Cu–10nD when compared with Cu–10G result from a probable additional milling mechanism produced by the hard nD particles that break up copper crystallites at a much smaller scale than that of the milling balls.

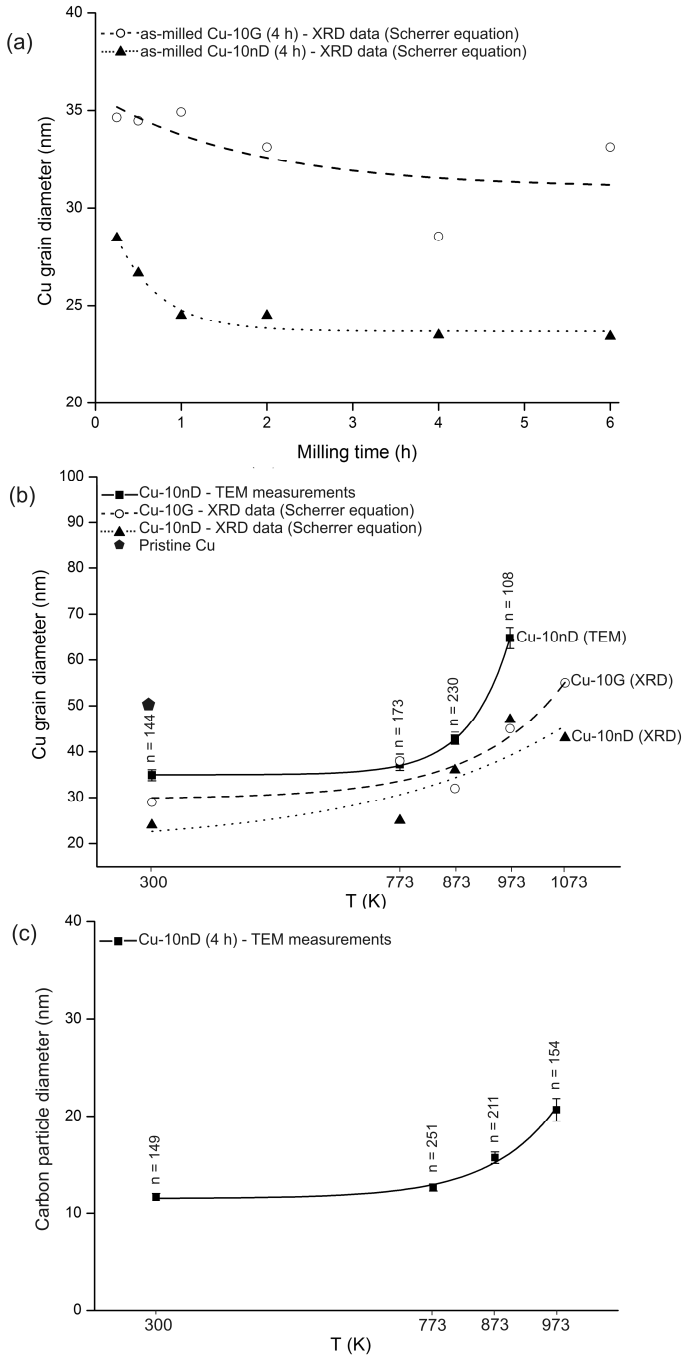

Figure 3.8. (a) Cu grain diameter evolution with milling time in both Cu–10nD and Cu–10G composites (XRD data – Scherrer equation). (b) Cu grain diameter in Cu–10nD composites milled for 4 h (TEM measurements and XRD data – Scherrer equation) and in Cu–10G composites milled for 4 h (XRD data – Scherrer equation) against temperature (1 h annealing). (c) nD particle diameter in Cu–10nD composites milled for 4 h (TEM) against temperature (1 h annealing). The number of grains/particles measured from TEM micrographs (n) is indicated above each point with error bars.

The apparent overestimation of the Cu grain diameter measured on TEM micrographs when compared with the values obtained from Scherrer equation (Figure 3.8 (b)) is justified by the existence of subgrains and/or defects like twins, since coherency domains contribute individually to the average grain size in XRD data and are not always clearly distinguishable in TEM images [26]. Nevertheless, as expected, the evolution of Cu grain size with temperature in the Cu-10nD composites shows a similar trend with both techniques (Figure 3.8 (b)).

Overall, the results demonstrate a remarkable microstructural thermal stability for both the Cu–10nD and Cu–10G composites with copper grain size remaining below 70 nm after 1 h at 973 K. Considering that the thermal stability of fine grained and nanostructured copper is low even at moderate temperatures (for instance, the 50% recrystallization temperature of 98% cold rolled 99.999% pure Cu is 360 K [27]), the current results demonstrate that the presence of carbon is inhibiting the matrix grain growth either through GB pinning by nanoparticles and/or through a solute drag effect resulting from GB stabilization by interstitial atoms. Although the solid solubility of C in Cu is virtually zero, the particle precipitation/coarsening process implies C diffusion through Cu, most probably via GB but also across the matrix. The mobility of the interstitial C atoms is indeed expected to be high, however the low equilibrium solubility favors solute stabilization at defective sites, contributing for GB pinning.

The carbon particles dispersed in the Cu–10nD composites evidenced also moderate growth with the heat treatments (Figure 3.8 (c)). Figure 3.9 presents the particle size distribution for each annealing temperature. The large particles present in the materials annealed at 873 and 973 K correspond to large low-Z regions such as A in Figure 3.2 (d). These regions contribute heavily to the average diameter increase determined for the highest annealing temperatures. Raman spectroscopy demonstrated that the observed growth is associated with a phase transformation where nD nanoparticles are progressively converted into larger regions of amorphous carbon.

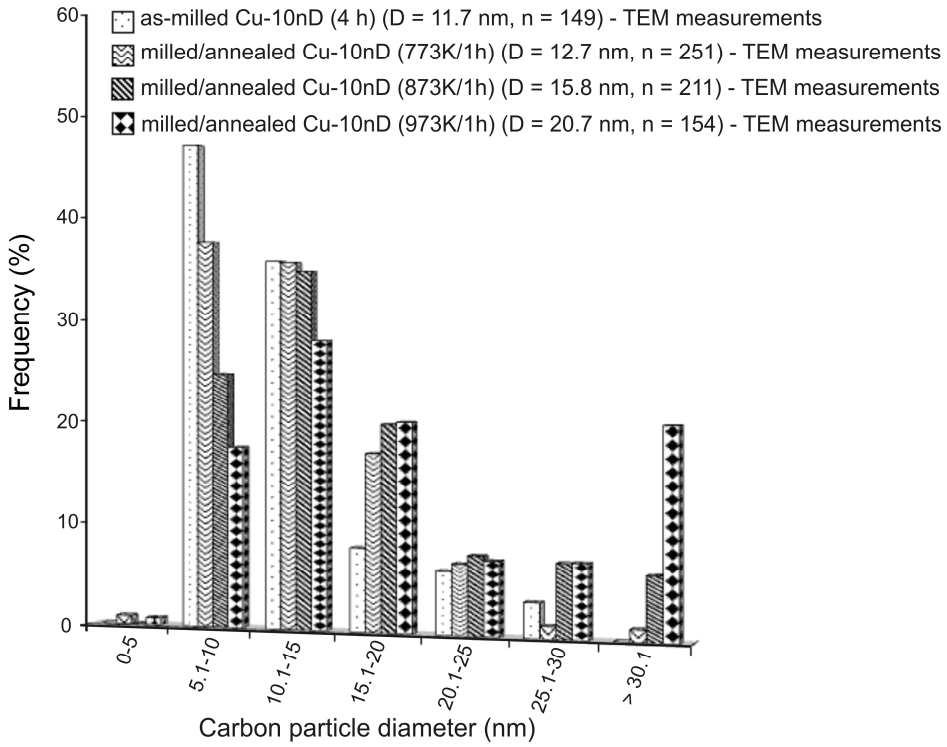

Figure 3.9. Histograms of carbon particle size (diameter) measured from TEM micrographs. The total number of particles measured (n) and the average diameter (d) are indicated in the legend for each condition.

Figure 3.10 presents the experimental Cu grain diameter (TEM and XRD) as a function of carbon particle average radius (TEM) for Cu–10nD, together with the expected equilibrium relation as determined from Zener equation [28]. Due to the low equilibrium solubility of carbon in Cu [29], *f* was considered roughly equivalent to the pre-milling volume ratio, i.e., 0.05. As expected, since equilibrium conditions were not reached after annealing for 1 h, the Cu grain sizes determined experimentally are lower then the calculated values and Zener model cannot be used to describe the observed behavior. However, the heat treatments at higher temperatures should have resulted in structures closer to equilibrium, i.e., with grain size closer to the values predicted by Zener equation. The fact that the difference between the experimental and equilibrium values (see shadowed region in Figure 3.10) is increasing instead of decreasing with annealing temperature suggests that, in addition to GB pinning, another mechanism such as solute drag may be operative.

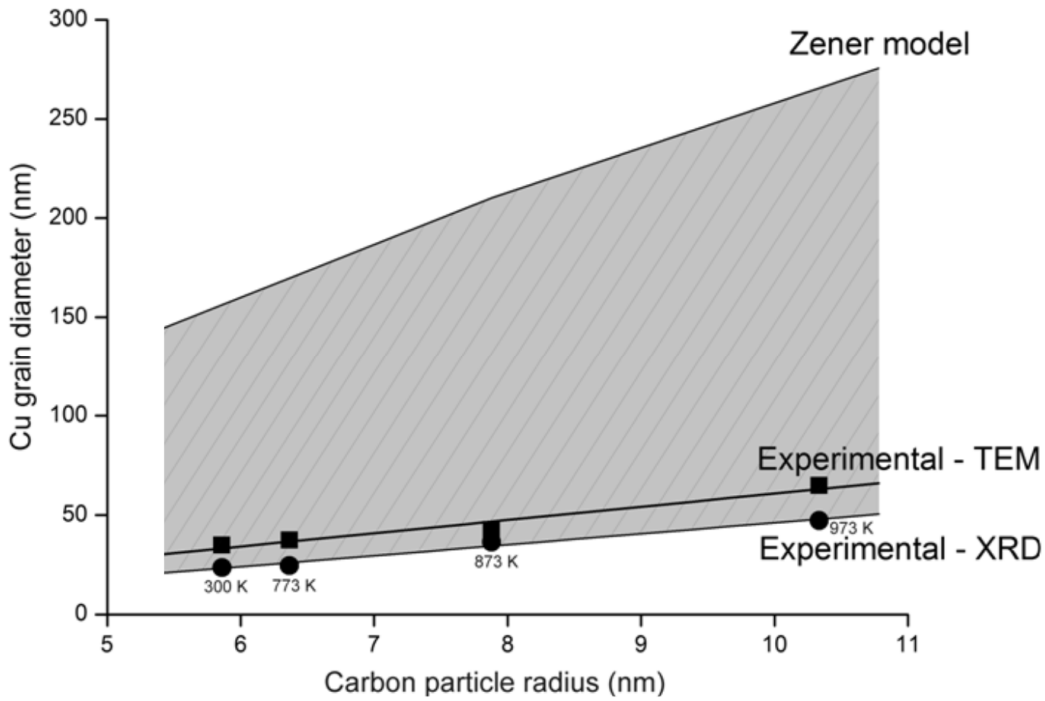

Figure 3.10. Cu grain diameter (XRD (Scherrer equation) and TEM) against carbon particle average radius (TEM). The Zener model prediction is also shown.

Previous investigations on nanostructured copper-based materials produced by high-energy milling demonstrated that Scherrer and Williamson-Hall methods yield similar grain sizes [1,30]. Nevertheless, to attest the influence of internal strain on XRD peak broadening, the Williamson-Hall method has also been used on the data collected from the Cu–10nD, Cu–0.1Cr–10nD, and Cu–10G materials. Table 3.2 lists the Cu grain diameter obtained from XRD data with Scherrer equation and with the Williamson-Hall method. The results confirm that in the present case the internal strains are extremely low in the as–milled conditions and virtually zero in the annealed materials. Therefore, the XRD peak broadening results essentially from mosaicity and is well accounted for as a grain size effect.

Strengthening mechanisms

Microhardness values for the conditions studied are presented in Table 3.2. The microhardness variation with milling time for the Cu–10nD composites shows that saturation occurs early during the milling process (2 h) in agreement with the grain size evolution (see Figure 3.7 (a)). The data demonstrates a remarkable hardness increase over pure nanostructured Cu ($H_{24\ nm}$ ~2.4 GPa [31,32] and $H_{10\text{-}30\ nm}$ ~2.5 GPa [33]) for the Cu–10nD (50 %), Cu–0.1Cr–10nD (46 %), and Cu–10G (~ 20%) composites in as–milled condition. No significant microhardness difference could be detected between the Cu–0.1Cr–10nD nanocomposite and the Cu–10nD nanocomposite, consequently the level of bonding strength is not significantly enhanced with Cr dissolution in the matrix. The present results demonstrate that high-energy milling alone achieves an effective bonding between the two phases at the nanoscale. Exposure to elevated temperatures led to a rampant decrease in hardness for all the as–milled materials due to Cu coarsening. Still the thermal stability of the nanostructured composites is notable since after annealing for 1 h at 773 K, which corresponds to a homologous temperature of 0.57 for pure Cu, the Cu–10nD composite remained significantly harder (~ 40 %) than pure nanostructured copper, while the Cu–10G composite presented the hardness level of pure nanostructured Cu. The microhardness results observed in both consolidated materials are also close to the hardness level of pure nanostructured Cu. The hardness decrease of the SPS material despite the presence of as–milled particles is associated to the heterogeneous constitution of the material, with areas of pure Cu softening the material. Hot extrusion shows results comparable to the Cu–10nD milled/annealed material at 873 K.

The Hall-Petch relation established for pure copper [31,32] is presented in Figure 3.11 together with values corresponding to the Cu–10nD, Cu–0.1Cr–10nD, and Cu–10G composites. The composites presented higher hardness then pure nanostructured copper, except for the Cu–0.1Cr–10nD composite annealed at 873 K and for both Cu–10nD and Cu–10G materials annealed at 973 K, where the carbon nanoparticles seem to have a weakening effect.

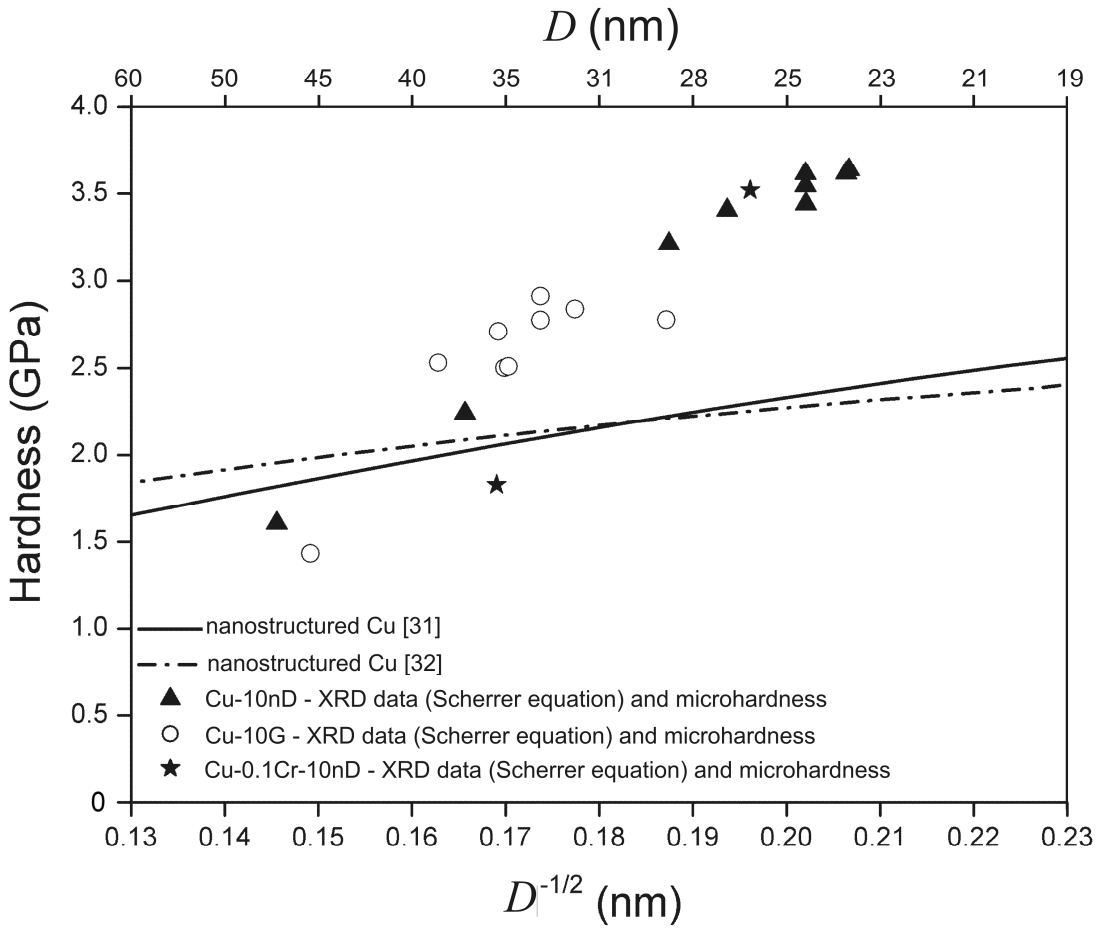

Figure 3.11. Relation between hardness and Cu grain size (XRD – Scherrer equation) for the Cu–10nD, Cu–0.1Cr–10nD, and Cu–10G composites. Curves commonly accepted for pure nanostructured Cu is shown for comparison [31,32].

Table 3.2. Vickers microhardness and Cu grain diameter obtained with TEM, Scherrer equation and Williamson-Hall method (WH) for the milled and heat-treated Cu–10nD, Cu–0.1Cr–10nD, and Cu–10G composites. The microhardness of the consolidated materials is also presented.

Condition	*H* (GPa)	*D* (TEM) (nm)	*D* (Scherrer) (nm)	*D* (WH) (nm)	Internal Strain (%)	Condition	*H* (GPa)	*D* (Scherrer) (nm)	*D* (WH) (nm)	Internal Strain (%)	Δ*H*
as–milled Cu-10nD (0.25 h)	3.21 ± 0.03	-	28	30	0.08	as–milled Cu-10G (0.25 h)	2.50 ± 0.02	35	43	0.11	0.71
as–milled Cu-10nD (0.5 h)	3.40 ± 0.03	-	27	25	0.09	as–milled Cu-10G (0.5 h)	2.51 ± 0.03	34	33	0.06	0.89
as–milled Cu-10nD (1 h)	3.54 ± 0.03	-	25	23	0.08	as–milled Cu-10G (1 h)	2.71 ± 0.03	35	38	0.07	0.83
as–milled Cu-10nD (2 h)	3.61 ± 0.03	-	24	24	0.08	as–milled Cu-10G (2 h)	2.77 ± 0.02	33	38	0.09	0.84
as–milled Cu-10nD (4 h)	3.62 ± 0.04	35	23	31	0.13	as–milled Cu-10G (4 h)	2.78 ± 0.04	29	24	0.04	0.84
as–milled Cu-10nD (6 h)	3.64 ± 0.03	-	23	22	0.08	as–milled Cu-10G (6 h)	2.91 ± 0.06	33	52	0.12	0.73
milled/annealed Cu-10nD (4 h/773K (1h))	3.44 ± 0.05	37	24	20	0.04	milled/annealed Cu-10G (4 h/773 K (1 h))	2.53 ± 0.04	38	44	0.09	0.91
milled/annealed Cu-10nD (4h/873 K (1 h))	2.24 ± 0.07	43	36	37	0.04	milled/annealed Cu-10G (4 h/873 K (1 h))	2.83 ± 0.06	32	30	0.06	0.59
milled/annealed Cu-10nD (4h/973 K (1 h))	1.61 ± 0.04	65	47	54	0.06	milled/annealed Cu-10G (4 h/973 K (1 h))	1.43 ± 0.04	45	43	0.03	0.18
as–milled Cu-0.1Cr-10nD (4 h)	3.52 ± 0.04	42	26	25	0.08						
milled/annealed Cu-0.1Cr-10nD (4 h/873 K (1 h))	1.83 ± 0.04	50	35	30	0.03						
milled/hot extruded Cu-10nD (4 h/873 K)	2.38 ± 0.05	60	-	-	-						
milled/SPS Cu-0.1Cr-10nD (4 h/1073 K)	2.45 ± 0.01	78	-	-	-						

Several mechanisms may be responsible for the observed behavior and are worthy of discussion:

(i) Solid solution

Although the solid solubility of C in Cu is virtually zero [3,34,35] metastable dissolution in the metallic matrix may occur due to the non-equilibrium processing conditions, especially for the Cu-10G composites due to the softer nature and lower milling stability of graphite when compared with diamond. However, the lower hardness of the as-milled Cu–10G as compared with Cu-10nD demonstrates that solid solution hardening, resulting from possible interstitial carbon, represents an overall minor contribution.

On the other hand, in spite of the low solid solubility of iron and chromium in copper, these milling media elements may dissolve in the metallic matrix, [36,37].

Nevertheless, the Cu lattice parameter showed no significant expansion with increasing milling time nor any reduction with annealing (Figures 3.12 (a) and (b), respectively). Since the lattice parameter is normally sensitive to changes in solute concentration, these results point to negligible C, Fe and Cr metastable dissolution in the Cu matrix. Therefore, solid solution strengthening effects have not been considered [36-39].

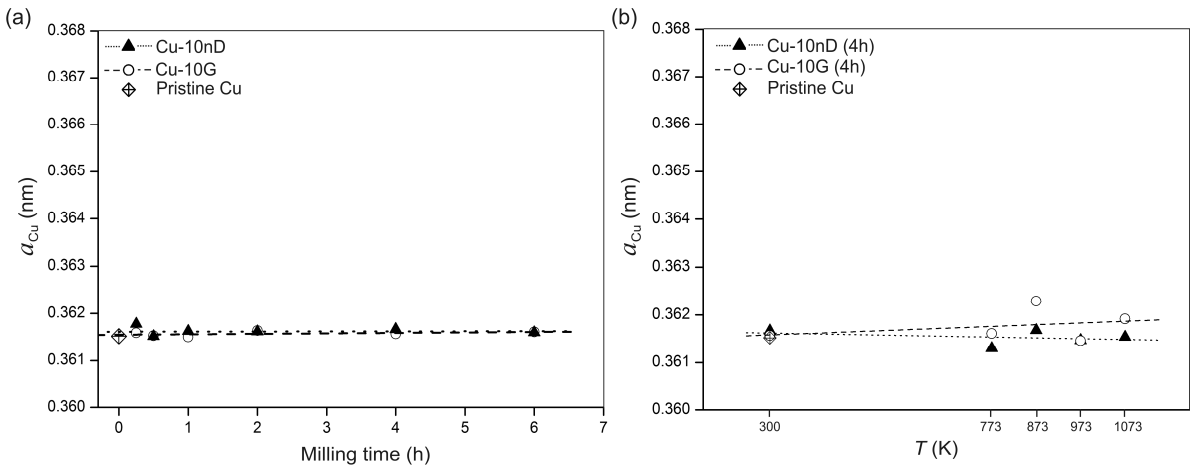

Figure 3.12. (a) Experimental lattice parameter evolution (a_{Cu}) with milling time (the pristine Cu lattice parameter is also presented). (b) Lattice parameter evolution with annealing treatments for the materials milled for 4 h. An estimated error of 0.0005 nm in lattice parameter was associated to the measurements [40,41].

(ii) Grain size

The Hall-Petch relation established for pure copper can be used to account for the Cu grain size strengthening effect in Cu–10nD, Cu–0.1Cr–10nD, and Cu–10G composites. Pure copper with grain size in the 10-30 nm range exhibits a maximum hardness of ~2.5 GPa [33]. The enhanced hardness of the composites above that of pure nanostructured copper can thus be considered to have another origin.

The quantitative determination of the grain size confirmed the microstructural stability of the annealed materials, which remained nanostructured (see Table 3.2). A slightly higher Cu grain size has been estimated for the consolidated materials when compared to the materials simply annealed (see Table 3.2). In the case of the SPS consolidated material the observed behavior represents the increase of Cu grain size in the nanostructured composite core and not the effect of the heterogeneous grain size distribution associated to the larger pure copper grains localized at prior powder boundaries surrounding the nanostructured composite cores (Figure 3.7 (c)). In the case of the extruded material the grain size attained reflects a dynamic recrystallization mechanism where deformation processes, that generate crystalline defects and decrease grain size, are competing with recovery and recrystallization phenomena, that generate recovered/recrystallized grains.

(iii) Orowan mechanism

A possible strengthening mechanism at the finer scales is the one first proposed by Orowan [42], which comprises dislocation bowing out and bypassing undeformable particles leaving a dislocation loop around them.

Partial dislocation emission from grain/domain boundaries with concomitant generation of stacking faults is a major deformation mechanism in nanostructured copper [43]. Since the absence of perfect dislocations in the nanostructured Cu grains was confirmed by TEM observation, the Burgers vector considered in the present analysis was

of the $\mathbf{b} = \frac{1}{6}\langle 11\bar{2}\rangle$ type. The stacking fault generated by the partial dislocation glide, which forms during the deformation of pure nanostructured copper, does not critically contribute to the Orowan stress increment since its stress term $\tau = \gamma/b$ depends on the stacking fault energy γ, and on the displacement of the matrix atoms b, but not on the dislocation line curvature [44].

Figure 3.13 presents the calculated dependence of ΔH on the carbon particle diameter for partial dislocations as given by Equation 1.16. The dependence for the stiffer perfect dislocations was also included for comparison and the parameters used are listed in Table 3.3. The curves show that a dispersion of 5-20 nm carbon particles throughout a Cu matrix induces a stress increment in the 0.5-2 GPa range for volume fractions of 5% for nD and 7% for G. However, the build-up of carbon phase at the grain boundary regions (see Figure 3.2) means that only a small fraction of the particles remains dispersed within the grains, furthermore carbon particles with sizes comparable to those of the Cu grains (20-30 nm see Table 3.2) are not expected to efficiently strengthen the material through an Orowan mechanism.

Table 3.3. Parameters used in the analysis of the Orowan-Ashby mechanism effect (Equation1.16).

Parameter	Value
M	3.06
k	0.84
$\lvert\mathbf{b}\rvert = \left\lvert\frac{1}{2}\langle 1\bar{1}0\rangle\right\rvert$ (nm)	0.255
$\lvert\mathbf{b}\rvert = \left\lvert\frac{1}{6}\langle 11\bar{2}\rangle\right\rvert$ (nm)	0.147
$f_{Cu\text{-}10nD}$ (initial)	0.05
$f_{Cu\text{-}10G}$ (initial)	0.07
ν	0.303
G (GPa)	42.1

Under favorable contrast conditions carbon clusters with sizes ≤ 5 nm have been observed within some Cu grains (see inset in Figure 3.13 and Ref. [3]). Although the

distribution homogeneity and volume fraction of such structures are unknown the clusters are expected to difficult dislocation glide, strengthening the as-milled Cu-10nD and Cu-10G materials.

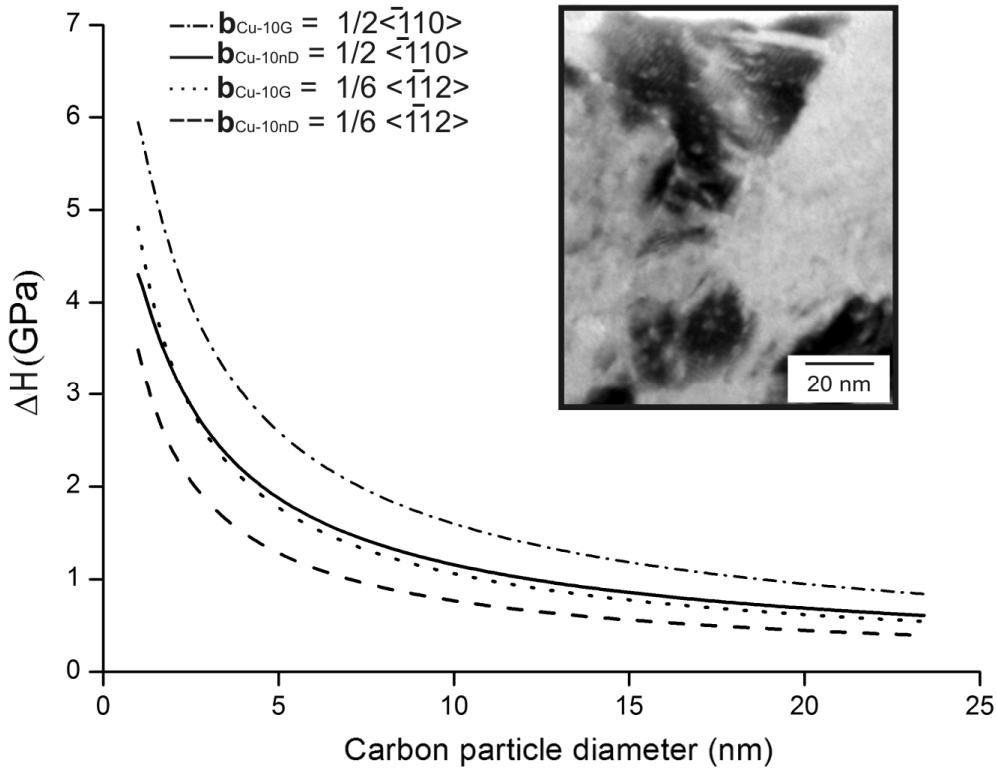

Figure 3.13. Orowan-Ashby model for perfect and partial dislocations. The nanocomposite distinction reflects the different volume fraction (5 % for nD and 7 % for G). The inset shows carbon clusters with sizes ≤ 5 nm dispersed within Cu grains of the milled (4 h) and annealed (773K/1h) Cu-10nD composite.

Similar considerations are valid for clusters arising from milling media contamination. The iron concentration has been determined by EDS analyses for the as-milled powders after milling times of 2, 4 and 6 h (Figure 3.14 (a)). As expected, the Fe content increased with milling time, although it remained below 1 at.% after milling for 6 h. X-ray maps obtained from as-milled powders showed an essentially homogeneous distribution of milling media debris. A few large Fe,Cr-rich inclusions (~500 nm) have also been observed (see squares in Figures 3.14 (b-d)), however these large inclusions

were expected to disintegrate into clusters and be dispersed throughout the Cu matrix during the milling operation [45]. Indeed, iron clusters as fine as 5 nm have been previously observed in Cu matrices [46]. Nevertheless accumulation at the Cu grain boundaries should occur and the volume fraction of Fe,Cr clusters effectively within the Cu grains is unknown. Due to the similar contrast, these metallic clusters could not be distinguished from the Cu matrix in TEM micrographs, yet these structures are expected to strengthen the as-milled Cu-10nD and Cu-10G materials by an Orowan mechanism.

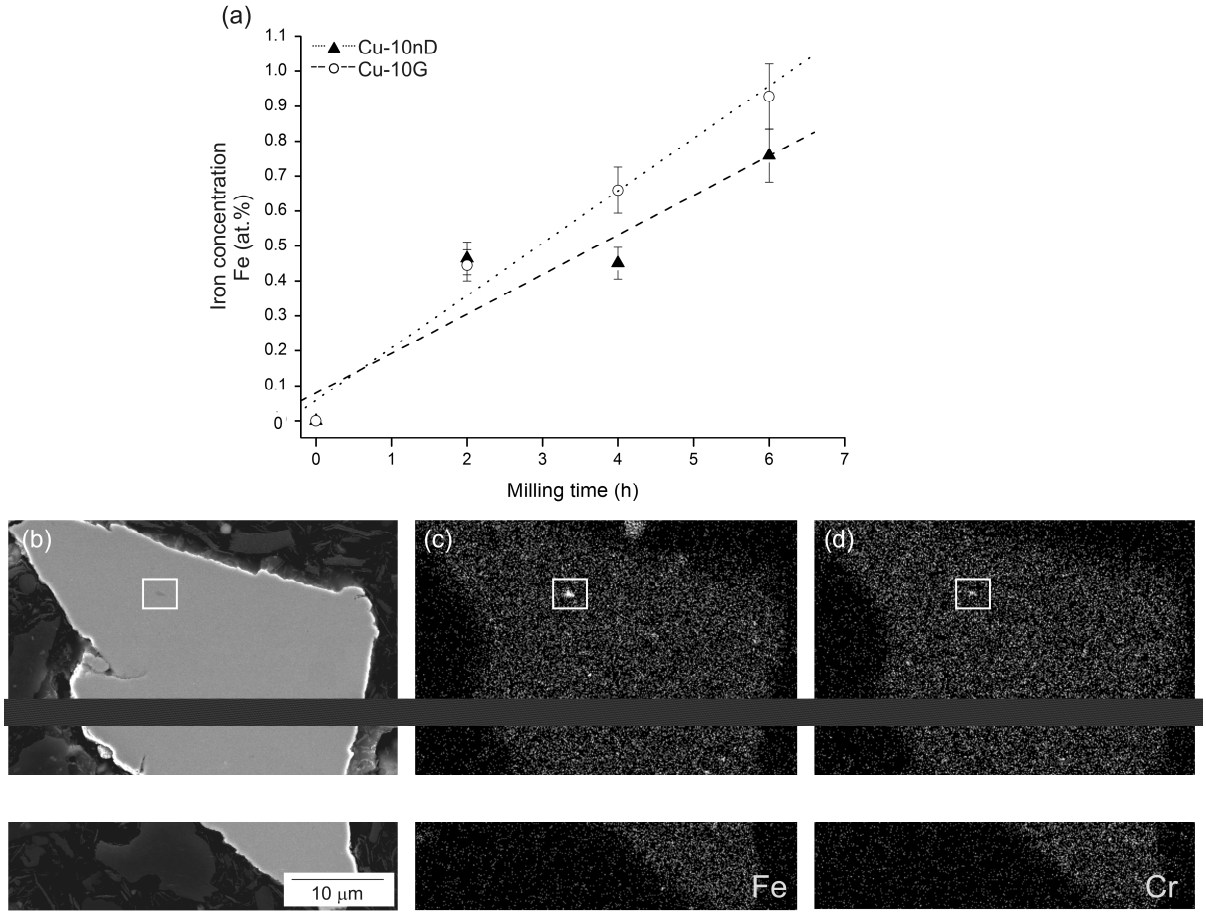

Figure 3.14. (a) Iron concentration versus milling time determined from 10 EDS point analyses. (b) BSE image of Cu-10nD as-milled powders after 4 h of milling with corresponding X-ray maps: Fe in (c) and Cr in (d). A Fe,Cr-rich inclusion is evidenced by the squares.

In order to determine the influence of carbon fraction and milling energy on carbide formation, a systematic investigation has been carried out using 10 and 20 at.% C and rotation speeds of 200 rpm and 400 rpm, for 4 h of milling time. Figure 4.2 shows diffractograms obtained for the materials produced. Ni_3C peaks were not detected in any of the diffractograms of Ni–10nD and Ni-20nD composites demonstrating that extensive carbide formation has not occurred for the conditions investigated (Figures 4.2 (a-d)). Ni_3C peaks have also not been observed for Ni-10G milled at 200 or 400 rpm, nor for Ni–20G milled at 200 rpm. Nonetheless, the Ni peak shift and asymmetry reflect the presence of solid solutions in the Ni-G materials (see Figures 4.2 (e-g)), which is justified by the lower milling stability of graphite when compared with diamond. On the other hand intense Ni_3C peaks were present in the diffractogram of Ni–20G milled at 400 rpm (Figure 4.2 (h)). The impact energy corresponding to 400 rpm is thus clearly higher than the activation energy required for Ni_3C synthesis from Ni and graphite, leading to extensive carbide conversion. The peaks of the pristine carbon phases are not observed due to the very large difference in atomic number between C and Ni and owing to the relatively small fraction of C in the composites.

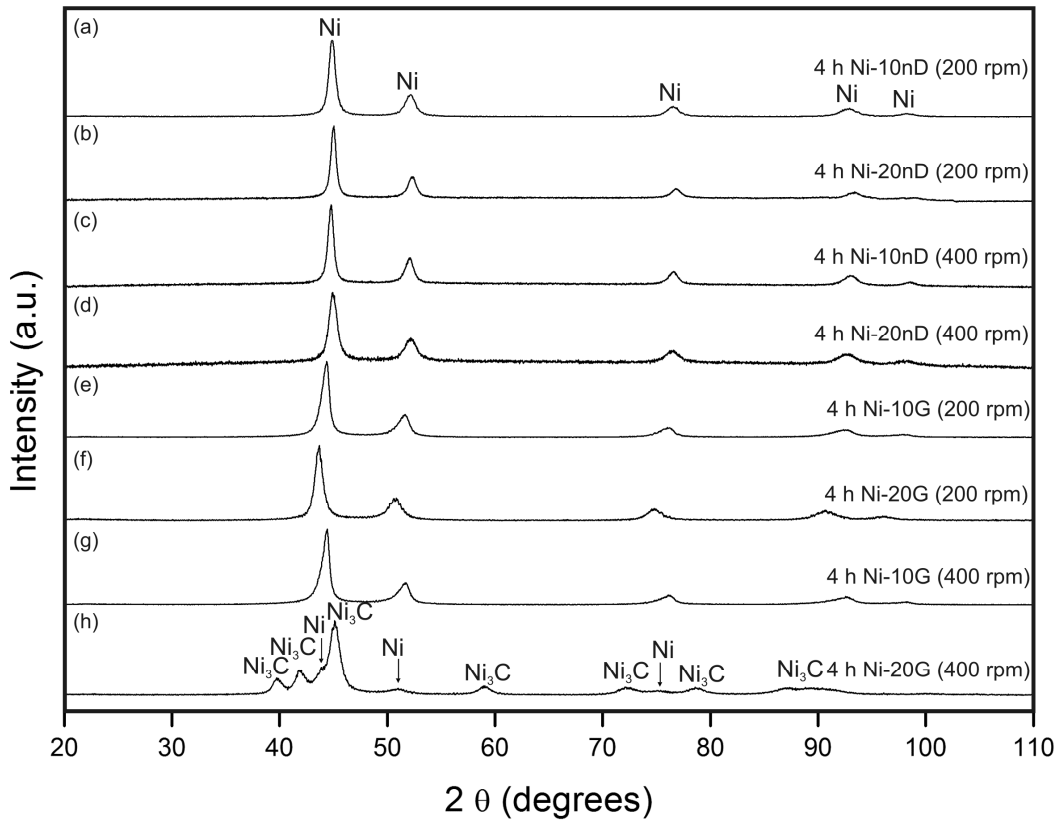

Figure 4.2. Experimental X–ray diffractograms of the as-milled nanocomposites. (a) 4 h Ni–10nD (200 rpm, (b) 4 h Ni–20nD (200rpm), (c) 4 h Ni–10nD (400 rpm), and (d) 4 h Ni–20nD (400 rpm). (e) 4 h Ni–10G (200 rpm), (f) 4 h Ni–20G (200 rpm), (g) 4 h Ni–10G (400 rpm), and (h) 4 h Ni–20G (400 rpm).

These preliminary experiments enabled to set suitable milling parameters for a compared assessment of the mechanical behavior of Ni–nD and Ni–G nanocomposites: 4 h of milling time, rotation speed of 200 rpm and 10 at.% C, which translated into homogeneous microstructure and particle distribution, minimal milling media contamination and negligible carbide formation.

Microstructural observations

Figure 4.3 shows representative microstructures of as–milled Ni–10nD and Ni–10G as well as milled/annealed Ni–10nD composites. Ring diffraction patterns attested for the absence of carbides, although extremely weak NiO rings (likely to originate from residual oxidation of the pristine nickel powder) could be detected (see Figure 4.3 (b)). Carbon particles were readily identifiable by the brighter contrast resulting from the low atomic number (see arrows in Figures 4.3 (a), (c) and (e)). Both as–milled microstructures displayed nanometric Ni grains with mottled contrast and ill-defined boundaries, characteristic of high-energy non-equilibrium states induced by intense deformation. Carbon particles, with diameters in the 5–20 nm range, were uniformly dispersed in the metallic matrices and frequently localized at Ni grain boundaries (GB). This phenomenon is associated with the cold welding processes occurring at the many deformation events that produce convolutions and Ni subgrain recombinations [2]. The carbon particles presented smaller sizes in the as–milled Ni–nD (0 to 10 nm) than in the as–milled Ni–10G (up to 20 nm) materials. The latter showed also higher aspect ratios owing to the intense localized deformation imposed on the relatively softer carbon phase. Both as–milled nanocomposites exhibited apparent bonding at the Ni/carbon interfaces suggesting a potentially efficient load transfer. The heat treatments resulted in Ni grain growth to submicrometer sizes in both Ni-10G and Ni-10nD materials (only the microstructure of Ni-10nD annealed at 1073 K is presented in Figure 4.3 (e)). The carbon particles globalized during annealing, coarsened up to 200 nm (see the magnified inset image and region A in Figure 4.3 (e)) and were distributed both along grain boundaries and within Ni grains.

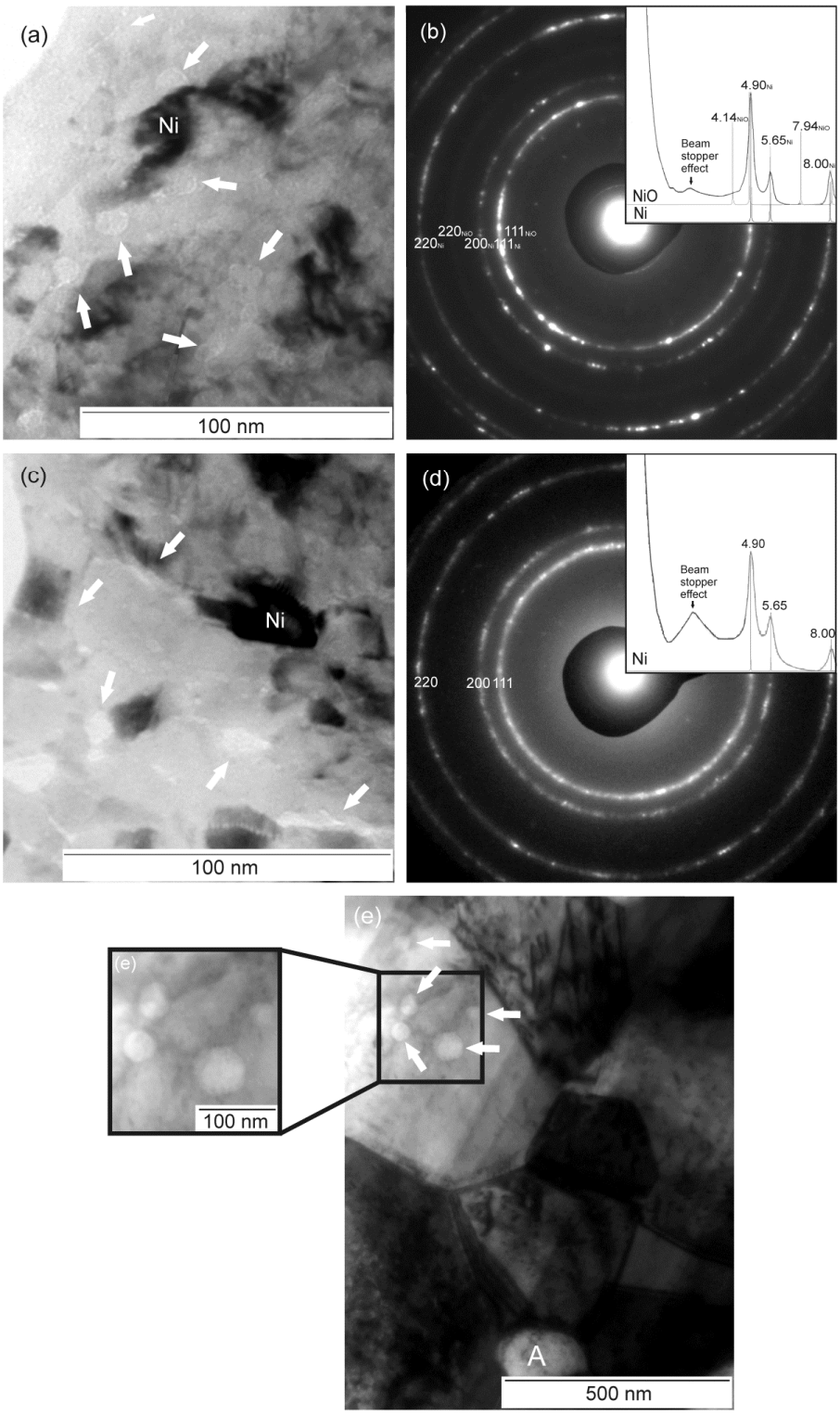

Figure 4.3. Bright–field TEM images of 10 at.% C nanocomposites milled for 4 h at 200 rpm. (a) Ni–10nD. (b) Diffraction pattern obtained from a large area similar to (a) with integrated radial profile (Ni and NiO simulations included with legend in nm^{-1}). (c) Ni–10G. (d) Diffraction pattern obtained from a large area similar to (c) with integrated radial profile (Ni simulation included with legend in nm^{-1}). (e) Ni-10nD composite milled for 4 h and heat-treated at 1073 K. The region A in (e) corresponds to a large carbon-rich particle. Carbon–rich regions within a Ni grain are shown in the magnified inset of (e). The arrows indicate low–Z contrast regions.

At moderate annealing temperatures diamond is very stable and small particles are not likely to dissolve in order to incorporate larger ones (a similar behavior has been observed for Zirconia dispersoids in a platinum matrix [3]). In addition, diamond is not expected to grow under atmospheric pressure. Therefore, the observed coarsening of nanodiamond could not have occurred through a diffusional Ostwald ripening mechanism. On the other hand, at higher annealing temperatures nanodiamond tends to amorphize [4] and this phase transformation facilitates dissolution. Hence, in the case of the annealed Ni–10nD materials, the observed increase in carbon particle size occurred with amorphous carbon, through a precipitate growth regime until C supersaturation in the Ni matrix dropped close to its equilibrium value (~1 at.% at 1073K [5]), at which time a coarsening Ostwald ripening regime took over. The nD growth phenomenon is thus associated with a phase transformation, which has operated during the heat treatments at 973 K and 1073 K (Figure 4.5).

Structural changes induced in the carbon phases could only be thoroughly evaluated after Ni extraction. EDS analyses showed that the remaining Ni after dissolution was kept below 6 at.% (part of which in NiO form).

Figure 4.4 shows TEM micrographs of the carbon phases extracted from milled composites with corresponding diffraction patterns. Individual particles with diameters in the 5-10 nm range were obtained from the Ni–10nD composites (a), whereas an amorphous phase was observed in the Ni–10G case (c). Ring diffraction patterns attested for the crystallinity of the milled/extracted nD (b), while the diffuse halo observed for the milled/extracted G (d) demonstrates an essentially amorphous nature.

Figure 4.5 shows micrographs and diffraction patterns of carbon phases extracted from annealed Ni–10nD and Ni–10G composites. After annealing at 1073 K the nD particles presented the typical interplanar spacings of graphite (see Figures 4.5 (a) and (b)). This transformation was hastened by the prior milling operation, since pristine (non-milled) nD powder annealed at 1073 K consists of particles with diameters in the 5–20 nm range presenting unequivocally the diamond structure (see Figure 3.5 (e) and (f), Chapter 3) and graphite forms only for temperatures higher than 1173 K [6,7]. These results show that the structural defects induced by ball milling, together with a possible catalytic function of Ni doping [8,9,10], contributed for a decrease in the graphitization temperature. The amorphous carbon resulting from milling the Ni–10G material has been converted into graphite sheets during annealing of the composites at

973 and 1073 K (see Figure 4.5 (c)). Since milled pure graphite remains amorphous up to 1573 K [11], the present results show that the presence of Ni enhances graphitization.

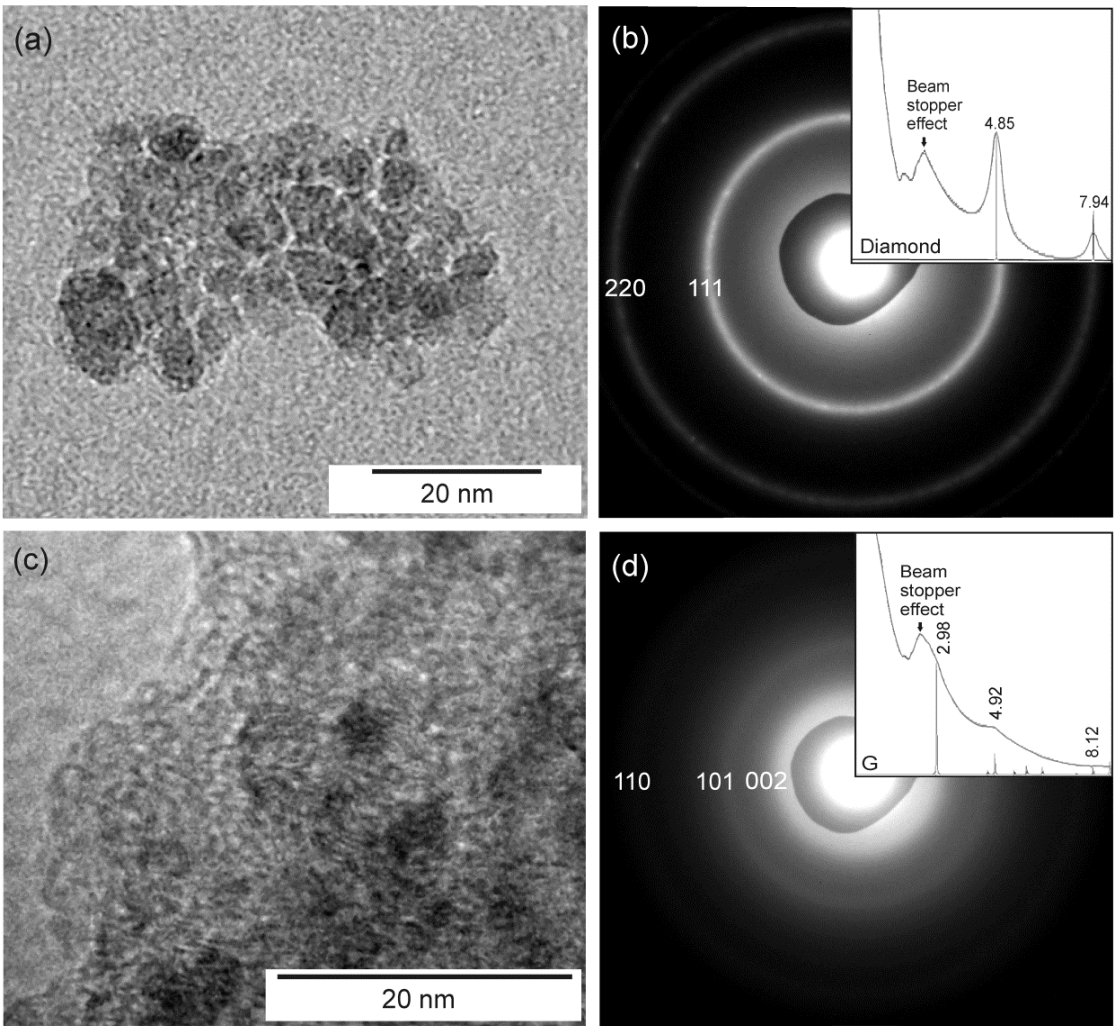

Figure 4.4. (a) Bright–field TEM image of carbon extracted from a Ni–10nD composite. (b) Diffraction pattern obtained from a large area similar to (a) with integrated radial profile (diamond simulation included with legend in nm^{-1}). (c) Bright–field TEM image of carbon extracted from a Ni–10G composite. (d) Diffraction pattern obtained from a large area similar to (c) with integrated radial profile (graphite simulation included with legend in nm^{-1}).

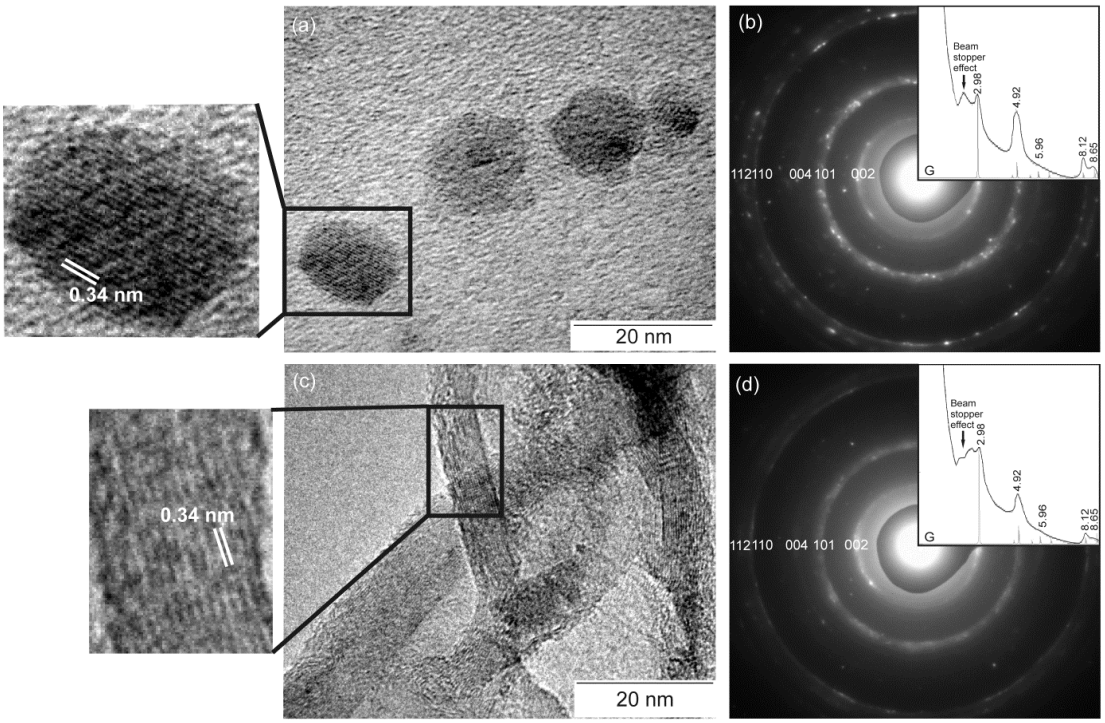

Figure 4.5. (a) Bright–field TEM image of the carbon phases extracted from the Ni–10nD milled composite annealed at 1073 K. (b) Diffraction pattern obtained from a large area similar to (a) with integrated radial profile (graphite simulation included with legend in nm^{-1}). (c) Bright–field TEM image of the carbon phases extracted from the Ni–10G milled composite and annealed at 1073 K. (d) Diffraction pattern obtained from a large area similar to (c) with integrated radial profile (graphite simulation included with legend in nm^{-1}).

Micro-Raman spectroscopy

Figure 4.6 presents the Raman spectroscopy results obtained from the carbon phases extracted from the Ni–10nD and Ni–10G materials. Figure 4.6 (a) shows Raman spectra of pristine nD, milled/extracted nD, pristine nD annealed at 1073 K and milled/annealed/extracted nD. Figure 4.6 (b) shows Raman spectra of pristine G, milled/extracted G and milled/annealed/extracted G.

The spectrum of milled/extracted nD is similar to that of pristine nD showing that the material remains stable during milling (Figure 4.6 (a)). These spectra present a band in the 1050–1200 cm^{-1} region, a major peak at ~1320 cm^{-1} and a broad band ranging from 1400 to 1700 cm^{-1}. The band at 1050-1200 cm^{-1} is likely to correspond to *Trans*-polyacetylene, that exhibits Raman peaks at 1125 cm^{-1} and 1480 cm^{-1} [12] and has been reported to exist in nD produced by different routes [13–16]. The peak at

~1320 cm^{-1} corresponds to structural sp^3 vibrations and the observed downshift (~10 cm^{-1}) is related to the phonon confinement effect in nanoscale particles [1717,18]. In both material types the broad band at 1400–1700 cm^{-1} is probably a convolution of the 1480 cm^{-1} *Trans*-polyacetylene peak and a sp^2 Raman peak originating from the outer graphite-like layers that envelope the diamond cores of nD powder [19,20].

The absence of the bands at ~1125 and 1480 cm^{-1} in the Raman spectra of milled/annealed/extracted nD (Figure 4.6 (a)) shows that *Trans*-polyacetylene is eliminated during the heat-treatments at 973 K and 1073 K. The well defined band at ~1580 cm^{-1} points to the presence of graphitic regions after the heat-treatments, while the 1250–1430 cm^{-1} signal represents a convolution of the diamond and graphite D bands. These results are in agreement with the electron diffraction patterns and indicate that graphitization of the milled nD occurred significantly at 973 K and was enhanced at 1073 K. The Raman spectrum of pristine nD material (non-milled) annealed at 1073 K, used as control, is similar to that of pristine nD, proving that the material remains stable during the heat treatment. However, contrarily to the milled/annealed/extracted materials, the *Trans*-polyacetylene peaks are still present in the annealed pristine nD.

The spectrum of pristine synthetic graphite powder (Figure 4.6 (b)) presents a major peak at 1580 cm^{-1} (G) and two bands at 1270–1370 cm^{-1} (D) and 1610–1620 cm^{-1} (D′). The milled/extracted G material shows an intense D-band at 1200-1400 cm^{-1} corresponding to fully amorphous carbon. The Raman spectra of the milled/annealed/extracted G materials show an intense D-band at 1200–1400 cm^{-1} and convoluted G and D′ bands at 1500–1650 cm^{-1}. The presence of the latter bands indicates that partial graphitization and coarsening of the essentially amorphous as–milled carbon occurred during the heat treatments of 973 K and 1073 K.

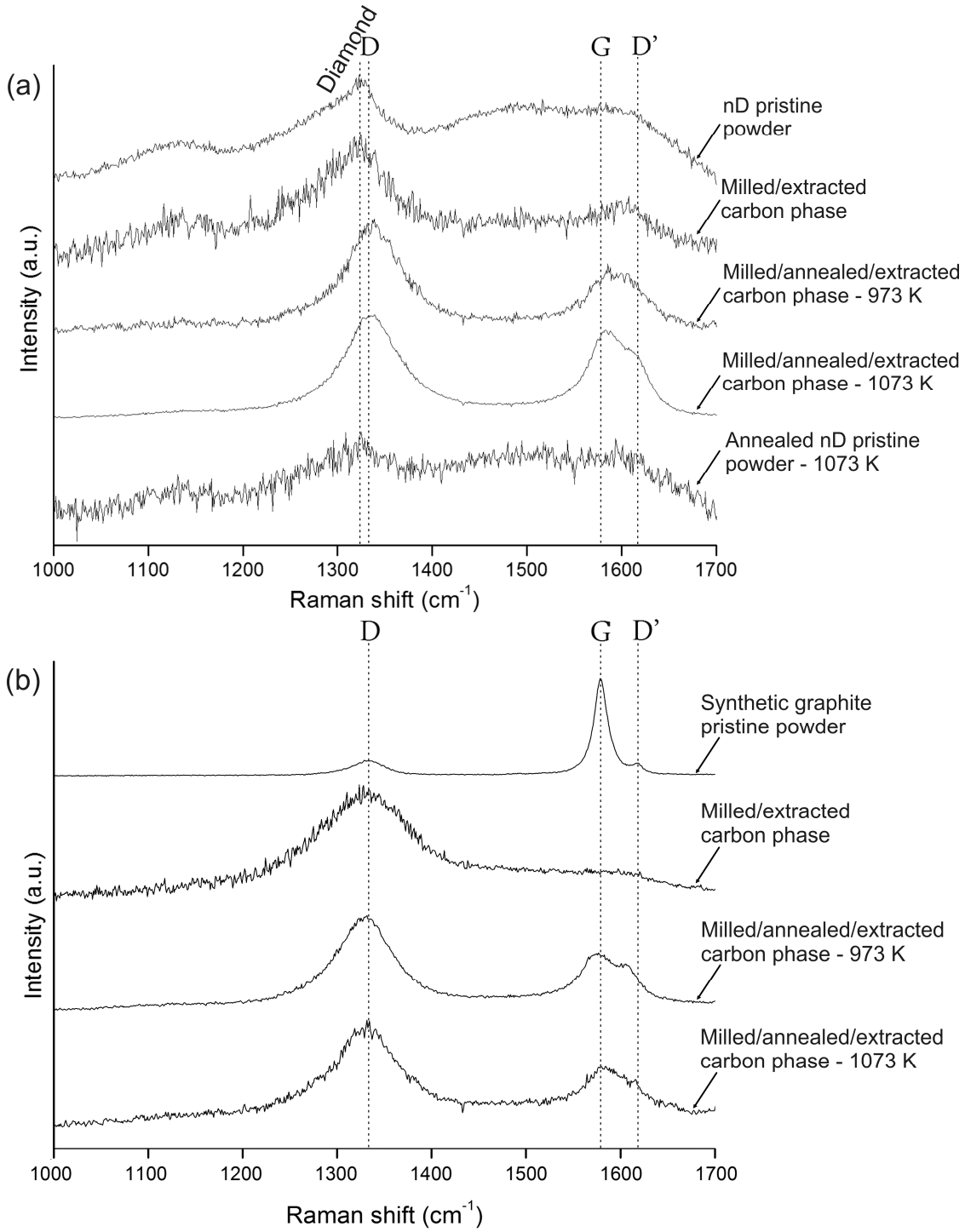

Figure 4.6. Raman spectra of pristine nD, milled/extracted, milled/annealed/extracted nD and annealed pristine nD powders (a). Raman spectra of pristine G, milled/extracted and milled/annealed/extracted G powders (b).

Table 4.2 presents the grain size and microhardness evolutions with milling time and annealing treatments for the Ni–10nD and Ni–10G materials. The grain size values calculated with Sherrer's equation are similar to the ones determined using the Williamson-Hall method, demonstrating a negligible effect of internal strain on XRD peak broadening in agreement with the results presented in Chapter 3 and previous studies on nanostructured metal–carbon composites produced by high–energy milling [21,22]. Both the Ni grain size and microhardness values showed saturation around 4 h of milling time. On the other hand exposure to elevated temperatures led to a rampant decrease in microhardness for both materials, indicating that GB pinning by nanoparticles or a solute drag effect were not very effective in stabilizing the microstructure of the Ni–10nD and Ni–10G composites at high temperature.

The Hall–Petch relation established for pure nickel [23] is presented in Figure 4.7 together with the experimental values corresponding to the Ni–10nD and Ni–G composites. At the finer scales the as–milled Ni–10nD and Ni–10G materials present a remarkable ~70% hardness enhancement ($H_{10\text{-}20\ \mathrm{nm}}$ ~ 10 GPa) over that of pure nanostructured Ni ($H_{10\text{-}20\ \mathrm{nm}}$ ~ 6 GPa). In the case of as-milled materials, a reinforcement effect can be ascribed to nD whereas solid solution strengthening occurred for Ni-G composites (see the Ni peak shifts in Figure 4.2 (e-g)). However, at the larger microstructural scales, i.e. for the annealed materials, the composites proved to be weaker than pure nickel of similar grain size. This resulted from the absence of solid solution and from the fact that carbon was present only under graphitic form (see Figure 4.5) which due to its soft nature could not effectively reinforce the matrix. The low microhardness values observed at intermediate microstructural scales, i.e., for low milling times, can be justified by the porosity associated to the convoluted layered structures.

Table 4.2. Vickers microhardness and Ni grain diameter obtained with Scherrer equation and Williamson-Hall method (WH) for the milled and heat–treated Ni–10nD and Ni–10G composites.

Condition	*H* (GPa)	*D* (Scherrer) (nm)	*D* (WH) (nm)	Internal strain (%)	Condition	*H* (GPa)	*D* (Scherrer) (nm)	*D* (WH) (nm)	Internal strain (%)
as–milled Ni–10nD (0.25 h)	2.15 ± 0.15	56	100	0.12	as–milled Ni–10G (0.25 h)	2.09 ± 0.09	57	92	0.11
as–milled Ni–10nD (0.5 h)	2.35 ± 0.12	53	71	0.1	as–milled Ni–10G (0.5 h)	2.06 ± 0.07	52	69	0.09
as–milled Ni–10nD (1 h)	4.01 ± 0.20	48	60	0.09	as–milled Ni–10G (1 h)	2.44 ± 0.09	43	53	0.09
as–milled Ni–10nD (2 h)	6.89 ± 0.18	30	29	0.06	as–milled Ni–10G (2 h)	5.49 ± 0.21	35	37	0.07
as–milled Ni–10nD (4 h)	8.83 ± 0.14	21	20	0.07	as–milled Ni–10G (4 h)	9.23 ± 0.10	(15)*	(11)*	*
as–milled Ni–10nD (6 h)	9.51 ± 0.16	21	23	0.07	as–milled Ni–10G (6 h)	9.90 ± 0.19	(12)*	(10)*	*
as–milled Ni–10nD (8 h)	9.79 ± 0.15	21	18	0.02	as–milled Ni–10G (8 h)	9.89 ± 0.19	(12)*	(10)*	*
milled/annealed Ni–10nD (4 h/973 K(1h))	0.94 ± 0.06	173	-	-	milled/annealed Ni–10G (4 h/973 K(1h))	3.23 ±0.05	113	-	-
milled/annealed Ni–10nD (4 h/1073 K(1h))	1.18 ± 0.07	202	-	-	milled/annealed Ni–10G (4 h/1073 K(1h))	1.45 ± 0.06	217	-	-

* Peak asymmetry induced by C solid solution (see Figures 4.2 (e-g)) interfered with the peak broadening [24] invalidating strain measurements. *D* values determined from Scherrer equation and the WH method are therefore merely indicative.

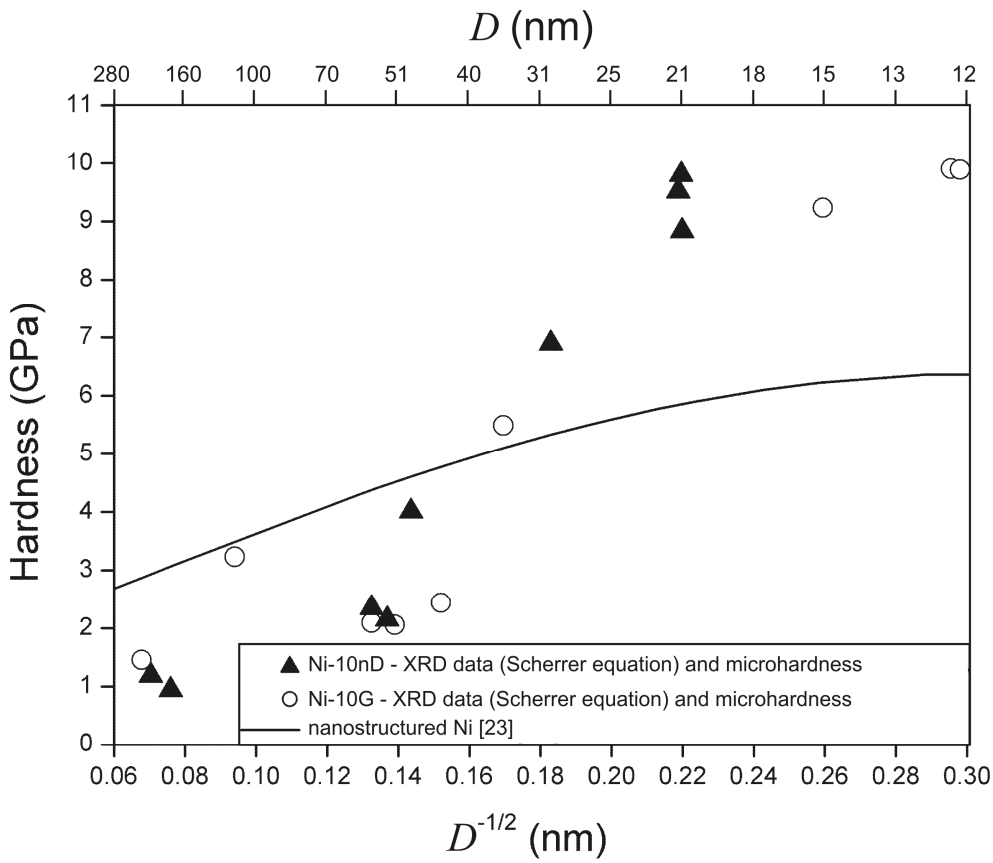

Figure 4.7. Relation between hardness and Ni grain size (XRD – Scherrer equation) for the Ni–10nD and Ni–10G composites. A curve commonly accepted for pure nanostructured Ni is shown for comparison.

Several mechanisms may be responsible for the observed behavior and are discussed next:

(i) Solid solution

Under equilibrium conditions the maximum solubility of carbon in Ni is 2.7 at.% (at 1600K [5]). However, a higher metastable solid solubility can be expected for materials produced by ball milling, especially in the case of the Ni–10G composites due to the softer nature and lower milling stability of graphite compared to diamond. Indeed, the Ni lattice parameter showed a substantial variation with increasing milling time for Ni–10G composites, in contrast to that of Ni–10nD composites where only a slight variation was observed (Figure 4.8 (a)). These results are in agreement with previous studies on Ni–C solid solutions [25,26].

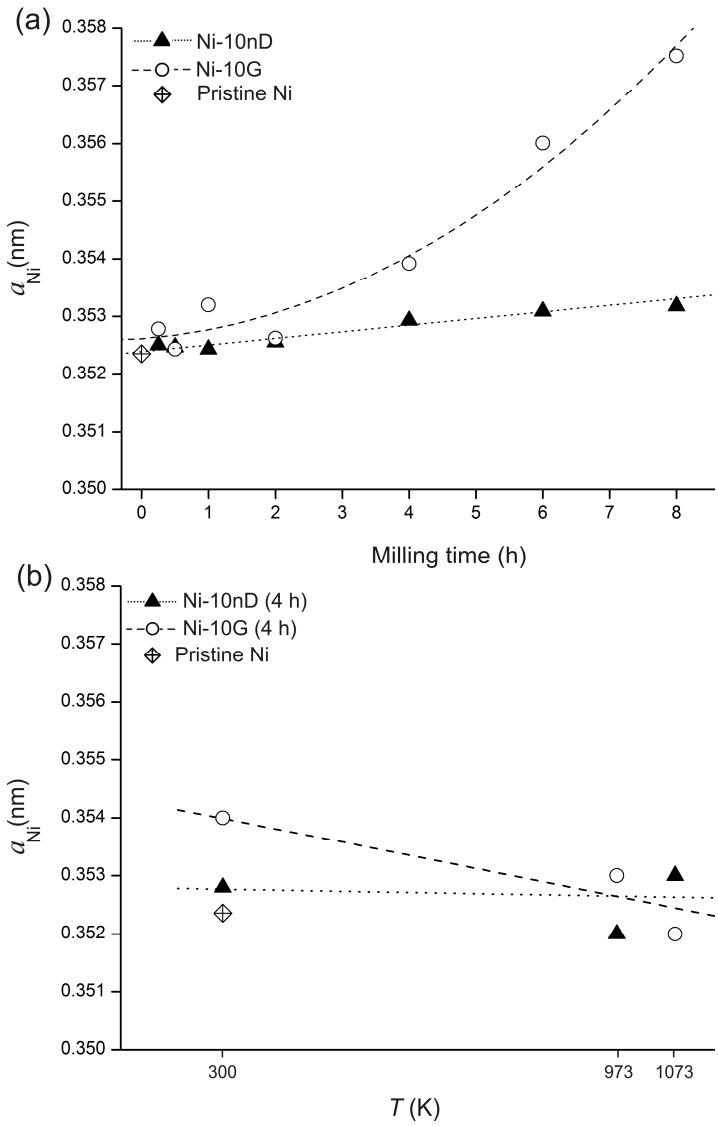

Figure 4.8. (a) Experimental lattice parameter evolution with milling time (the pristine Ni lattice parameter is also presented). (b) Lattice parameter evolution with annealing treatments for the materials milled for 4 h. An estimated error of 0.0005 nm in lattice parameter was associated to measurements [27,28].

After annealing at 973K the Ni–10G composite presented a smaller Ni grain size and higher hardness than the Ni–10nD one (see Table 4.2), suggesting that solid solution may have delayed coarsening at 973 K. Nevertheless, the lattice parameter indicates a residual presence of C in solid solution after 1 h at 973 K for both materials (Figure 4.8 (b)), and thus the hardness enhancement of Ni–10G compared to Ni–10nD (see Table 4.2) is likely to result only from the smaller grain size.

Extraneous elements originating from milling media materials may also have dissolved in the metallic matrix, and indeed it has been shown that iron in pure nickel results in significant solid solution strengthening [29,30]. The presence of iron arising

from milling media has been estimated from EDS analyses performed on materials milled for 4, 6 and 8 h. This element has been assumed to be fully dissolved in the Ni matrix and its influence on the Ni lattice parameter has been determined through the Vegard's law for the Fe-Ni system [29,30]: $a_{\mathrm{Ni}}^{\mathrm{Fe}}$(nm) = 0.35239 + 0.000139 Fe (at.% Fe) (Figure 4.9 (a)). The influence of the minor elements that constitute the DIN 1.4034 stainless steel has been neglected. The concentration of C in solid solution was determined from the Vergard's law for the C-Ni system [31]: $a_{\mathrm{Ni}}^{\mathrm{C}}$(nm) = 0.35238 + 0.00074 C (at.% C) by subtracting the effect of iron solute on the Ni lattice parameter expansion, i.e., by assuming that $a_{\mathrm{Ni}} = a_{\mathrm{Ni}}^{\mathrm{C}} + a_{\mathrm{Ni}}^{\mathrm{Fe}}$ (Figure 4.9 (b)).

The relative contributions of C and Fe on the expansion of the Ni lattice parameter are given in Figure 4.9 (c) and (d), respectively, for Ni-10G and Ni-10nD composites. These results imply a significant contribution of solid solution hardening in the case of Ni–10G composites and a minor one for Ni-10nD composites.

(ii) Grain size

The Hall-Petch relation established for pure nickel should account for the hardening effect of Ni grain size, and the strengthening above that of pure nanostructured Ni observed for the Ni–10nD and Ni–10G composites has thus another origin. Finer Ni grain sizes were expected for the as–milled Ni–10nD composites due to an anticipated additional milling mechanism between the steel spheres and the hard nD particles that may assist grain refinement, as described for the Cu-10nD material in Chapter 3. However, the Ni–10G materials presented a somewhat steeper grain size decrease with milling time compared to the Ni–10nD composites (see Table 4.2). This may be a spurious effect resulting from peak asymmetry [24] induced by the C atoms in solution, and/or may originate from a difference in fracture toughness of the solid solution hardened matrix.

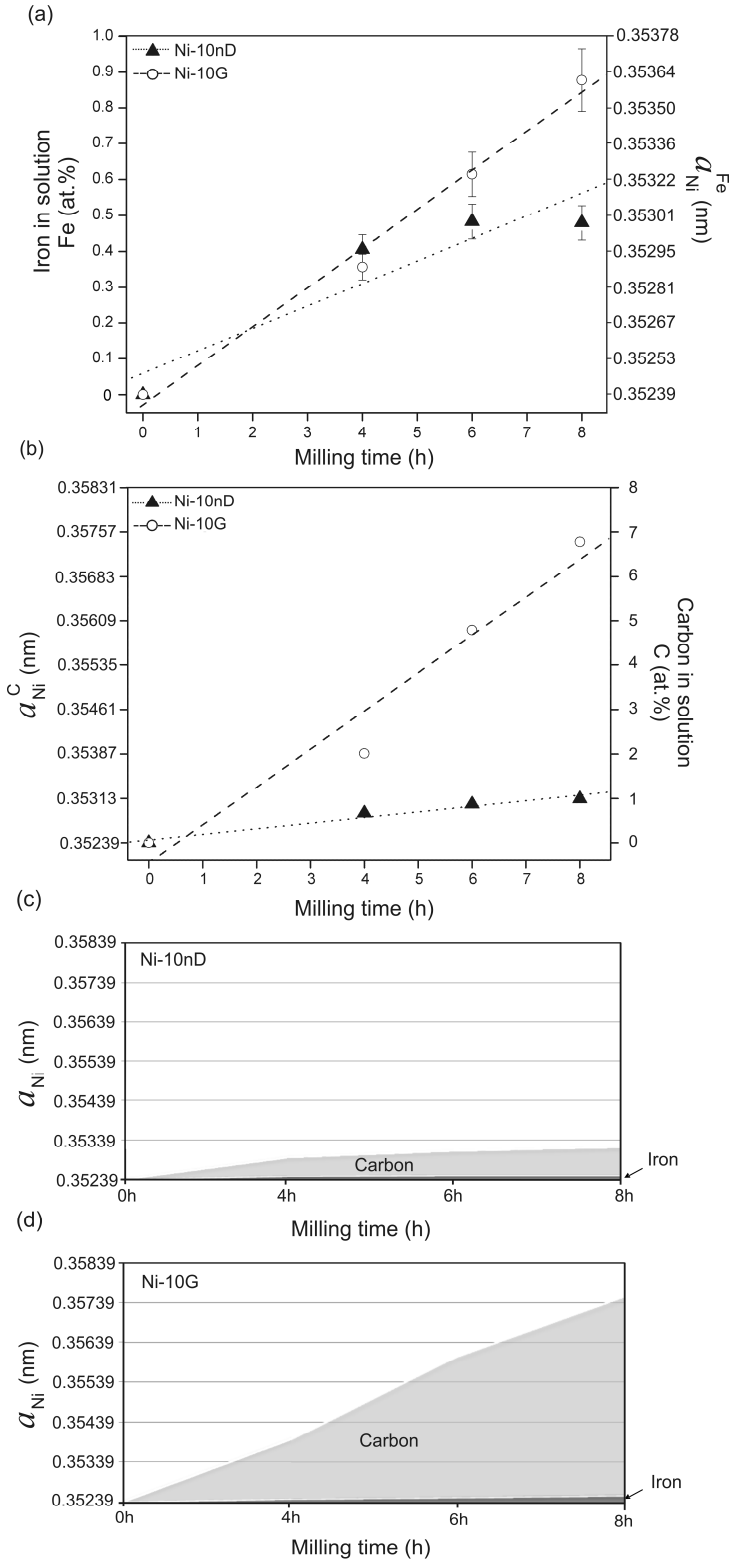

Figure 4.9. (a) Measured iron concentration (left-hand axis) for milling times of 4, 6 and 8 h, and expansion of Ni lattice parameter (right-hand axis) determined through the Fe-Ni Vergard's law [29,30]. (b) Lattice parameter expansion induced by C in solution (left-hand axis) determined from the measured lattice parameter by subtracting the effect of Fe, and C solute (right-hand axis) determined from the C-Ni Vergard's law [31]. Relative effect of Fe and C on the Ni lattice parameter expansion against milling time for Ni-10nD (c) and Ni-10G (d).

(iii) Orowan mechanism

As indicated in Chapter 3, a possible strengthening mechanism at the finer scales is the one first proposed by Orowan [32]. Partial dislocation emission from grain/domain boundaries with concomitant generation of stacking faults is a major deformation mechanism in nanostructured nickel [33]. Since the absence of perfect dislocations in the nanostructured Ni grains was confirmed by TEM observations, the Burgers vector considered in the present analysis was of the $\mathbf{b} = \frac{1}{6}\langle 11\bar{2} \rangle$ type. The stacking fault generated from the partial dislocation glide, which forms during the deformation of pure nanostructured nickel, has been assumed to not critically contribute to the Orowan stress increment as explained in Chapter 3.

Figure 4.10 presents the calculated dependence of ΔH on the carbon particle diameter for partial dislocations given by Equation 1.16, where the analysis for perfect dislocations was included for comparison. The parameters used in the calculations are listed in Table 4.3. The curves show that a dispersion of 5–20 nm carbon particles (see Figure 4.3) throughout a Ni matrix induces stress increments in the 1-3 GPa range for volume fractions of 5% for nD and 8% for G. However, the build-up of carbon phase at the grain boundary regions (see Figure 4.3) means that only a small fraction of the particles remains dispersed within the grains, furthermore carbon particles with sizes comparable to those of the Ni grains (20-30 nm see Table 4.2) are not expected to efficiently strengthen the material through an Orowan mechanism. Contrarily to the Cu-based composites, clusters of carbon and of milling media debris are not likely to be dispersed in the Ni grains since both phases can fully dissolve in the metallic matrix (as attested by the expressive Ni lattice parameter expansion in Figures 4.8 and 4.9). Therefore the Orowan strengthening has been considered negligible in Ni-10nD and Ni-10G composites.

Table 4.3. Parameters used in the analysis of the Orowan-Ashby mechanism (Equation1.16).

Parameter	Value
M	3.06
k	0.84
$\lvert\mathbf{b}\rvert = \left\lvert\frac{1}{2}\langle 1\bar{1}0\rangle\right\rvert$ (nm)	0.249
$\lvert\mathbf{b}\rvert = \left\lvert\frac{1}{6}\langle 11\bar{2}\rangle\right\rvert$ (nm)	0.144
$f_{Ni\text{-}10nD}$ (initial)	0.05
$f_{Ni\text{-}10G}$ (initial)	0.08
ν	0.31
G (GPa)	76

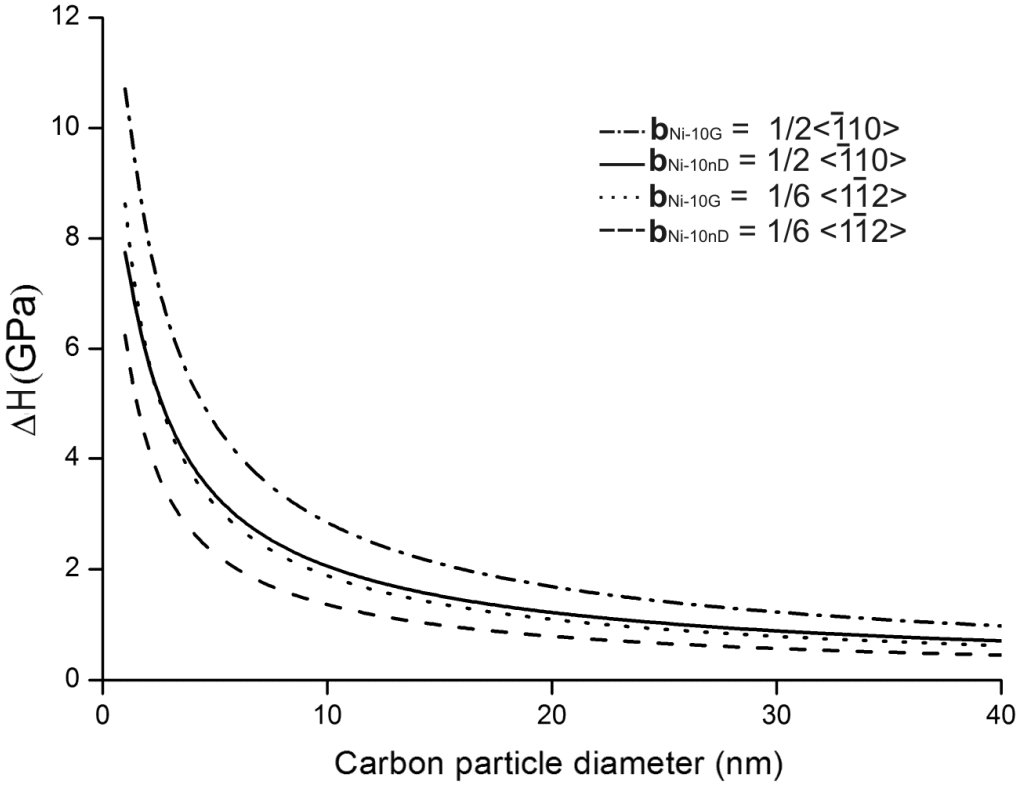

Figure 4.10. Orowan-Ashby model for perfect and partial dislocations. The nanocomposite distinction reflects the different volume fraction (5 % for nD and 8 % for G).

(iii) Second-phase reinforcement

The relatively modest solid solutions observed for as-milled Ni-10nD composites (Figure 4.9 (c)) indicates that the high hardness of these materials originates from the load bearing ability of the nD particles, which in turn attests for a relatively efficient load transfer at the carbon/metal interfaces. Second phase reinforcement is thus one of the operating strengthening mechanisms in this system.

The same behavior was not expected for the Ni–10G composites due to the soft nature of milled graphite, which is likely to have a weakening influence. Indeed, in this system the strength enhancement over that of pure nanostructured nickel results probably from solid solution hardening (see Figures 4.8 (a) and 4.9 (b)).

The transformation of nD into soft graphitic structures during the heat treatments reduced the load bearing ability of the carbon particles. This phenomenon in association with solute segregation from the metallic matrix (see Figure 4.8 (b)) weakened the annealed Ni-10nD and Ni-G materials in relation to pure nanostructured nickel of comparable grain size (see Table 4.2 and Figure 4.7).

The reinforcement effect of nD particles and the expected weakening influence of amorphous carbon particles are assumed to contribute to the strength of the as-milled materials according to a law of mixtures with a direct dependence on the efficiency of the interfacial load transfer [22].

(iv) Cumulative effects

As with the Cu-based nanocomposites, a linear additive model can be employed to estimate the contribution of each strengthening mechanism based on the following premises:

- The effect of Ni grain size can be estimated with models developed for pure nanostructured nickel, such as the one given by Equation 1.8.
- The hardness level of the as-milled Ni-10nD nanocomposite reflects an effective load transfer to the reinforcing nD particles, which can be described by a rule of mixtures (Equation 1.20).
- The strengthening above that of pure nanostructured Ni observed for the Ni-10G material (see Figure 4.7) cannot originate from load transfer to the soft graphite.

- In the present systems the solid solution of C and Fe must influence the materials strength, especially in the case of the Ni-10G material.
- Milling media contamination is expected to represent a minor strengthening contribution when compared to carbon solid solution (see Figure 4.8 (c) and (d)).
- The hardness level attained by the Ni-10nD and Ni-10G composites is similar, i.e., the nD reinforcement effect in Ni-10nD is comparable to the solid solution hardening in Ni-10G.
- Since both C and Fe can easily dissolve in the metallic matrix, clusters of these elements are not likely to occur and the Orowan mechanism has been considered negligible.

Combining the effects of the nanostructured Ni grain size and the C and Fe solid solutions with the intrinsic hardness of the carbon allotrope (Equations 1.4, 1.8, and 1.20, respectively):

$$H = \delta\, H_R\, f + \left[H_0^Z + \mathcal{K}_{\mathrm{C}}^{\mathrm{SS}}\, \mathrm{C}^{\mathsf{m}_{\mathrm{C}}} + \mathcal{K}_{\mathrm{Fe}}^{\mathrm{SS}} \mathrm{Fe}^{\mathsf{m}_{\mathrm{Fe}}} + \left[k_H^Z + k_H^D D^{-1/2}\right] exp\left[\frac{1}{T}\frac{\mathcal{H}_{\mathrm{m}}/(3\mathcal{R})}{D/(6\mathrm{h})-1}\right]\right](1-f) \qquad (4.1)$$

where the nomenclature is given in Chapter 1. The solid solution coefficients, $\mathcal{K}_{\mathrm{C}}^{\mathrm{SS}}$ and $\mathcal{K}_{\mathrm{Fe}}^{\mathrm{SS}}$, were adapted from equation 1.4 for, respectively, interstitial carbon and substitutional iron. Two independent solid solution exponents, respectively, m_{C} and m_{Fe}, have also been considered for the two solute types. Both solid solution contributions have been incorporated in the intrinsic matrix hardness term H_0, which accounts for strengthening mechanisms other than grain size: $H_0 = H_0^Z + H_{SS} + H_{Orow}$ (Eq. 3.2) [34]. The Orowan term (H_{Orow}) has not been considered for the current composite systems.

The experimental and theoretical parameters used in the model are listed in Tables 4.4 and 4.5, respectively. The volume fraction, *f*, of dispersed carbon particles (see Figure 4.3) was calculated by subtracting the carbon in solution and by considering the milling media input. Only as-milled materials have been considered since the load transfer at the Ni/C phase interface is likely to have changed during the annealing treatments. Furthermore, full microstructure homogenization was attained only for 4, 6 and 8 h milling times. The carbon phase hardness values (H_R) have been assumed to be 60 GPa [35] for diamond, and 0.3 GPa for milled graphite [36,37].

Table 4.4. Ni lattice parameter, Ni grain size obtained with Scherrer equation, carbon and iron in solution, volume fraction of reinforcing particles and Vickers hardness for the 4, 6 and 8 h milling time conditions.

Conditions	Ni lattice parameter *a* (nm)	Ni grain size *D* (nm)	Total carbon (at.%)	Carbon in solution C (at.%)	Total iron (in solution) Fe (at.%)	Total volume fraction of the carbon phase	Volume fraction of carbon reinforcement (not dissolved) *f*	Experimental *H* (GPa)
as–milled Ni–10nD (4 h)	0.35293	21	9.05%	0.67	0.40	5%	3.86%	8.83
as–milled Ni–10nD (6 h)	0.35309	21	9.04%	0.87	0.48	5%	3.77%	9.51
as–milled Ni–10nD (8 h)	0.35318	21	9.04%	0.99	0.48	5%	3.71%	9.79
as–milled Ni–10G (4 h)	0.35392	15	9.05%	2.01	0.35	8%	4.85%	9.23
as–milled Ni–10G (6 h)	0.35601	12	9.03%	4.79	0.61	8%	2.98%	9.90
as–milled Ni–10G (8 h)	0.35752	12	9.01%	6.78	0.87	8%	1.58%	9.89

Table 4.5. Theoretical parameters used in the cumulative model.

Parameters	Ni-10nD	Ni-10G
H_0^Z (GPa) [23]	1.021	1.021
H_R (GPa)	60	0.3
k_H^Z (GPa) [23]	0.071	0.071
k_H^D (GPa nm$^{-1/2}$) [23]	26.63	26.63
T (K)	300	300
$\mathcal{H}_m$ (kJ mol) [23]	17.47	17.47
h (nm) [23]	0.2754	0.2754
$\mathcal{R}$(KJ/molK)	0.008314	0.008314
G (GPa)	76	76

The efficiency of the load transfer to the reinforcement phase (δ) [22], as well as the solid solution coefficients, κ_C^{SS} and κ_{Fe}^{SS} and exponents, m_C and m_{Fe},, have been used as fitting parameters. The fitting parameter δ has been assumed to be equal both for Ni-10nD and Ni-10G systems, as nanodiamond particles are surrounded by graphite-like carbon [38] and during milling graphite undergoes a phase transformation into amorphous carbon that can present a mixture of sp^2/sp^3 [39]. Therefore, similar interfacial bonding can be expected for both carbon phases.

Fitting of Equation 4.1 to the experimental hardness values has been carried out using nonlinear least squares regression employing the Newton method for error minimization [40]. The parameters resulting from fitting Equation 4.1 are presented in Table 4.6. The efficiency of the load transfer from the Ni matrix to the carbon phases is 0.32, significantly higher than the one achieved to the Cu composites (0.21). This result demonstrates a superior metal-carbon bonding for nickel in agreement with its higher affinity for carbon [41]. The solid solution parameters resulting from fitting point to a considerable strengthening effect for C, while the substitutional contribution originating from milling media contamination proved to be negligible. The solid solution term in Equation 4.1 corresponds to: $H_{SS} = 3.18\ C^{0.1}$ (see Figure 4.11). This represents a relatively weak dependence of hardness on the solute concentration for carbon contents such as the ones inferred for the Ni-10G composites (see Table 4.2), which is compatible with the hardness evolution for 4, 6 and 8 h of milling time observed.

Table 4.6. Parameters determined from fitting the cumulative model.

Parameters	Value
δ	0.32
K_C^{SS}	3.18
m_c	0.1
K_{Fe}^{SS}	0
m_{Fe}	-

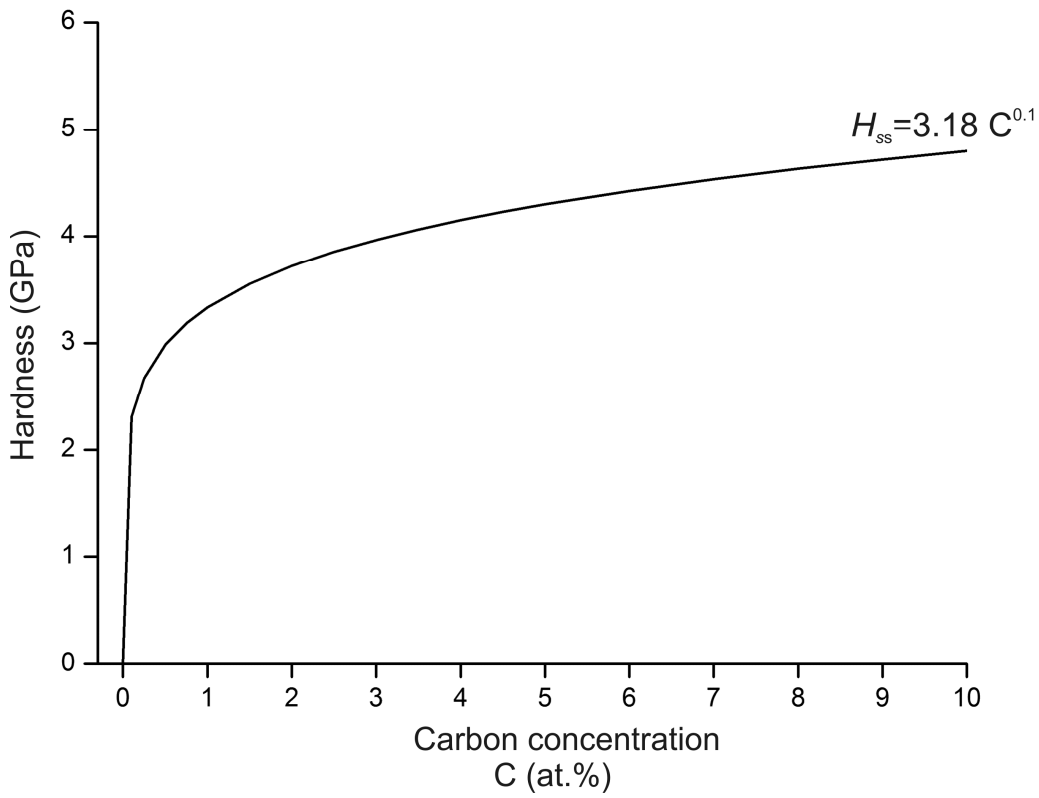

Figure 4.11. Hardness calculated with the carbon solid solution term versus carbon concentration.

The grain size dependence calculated with the cumulative model for each condition is shown in Figure 4.12. Regarding the quality of the fitting the optimized parameters were rather insensitive to changes in initial guesses as well as to numerical convergence parameters. Globally an average relative error of 2.3% has been achieved, attesting for the fitting quality (see Table 4.7 and Figure 4.12).

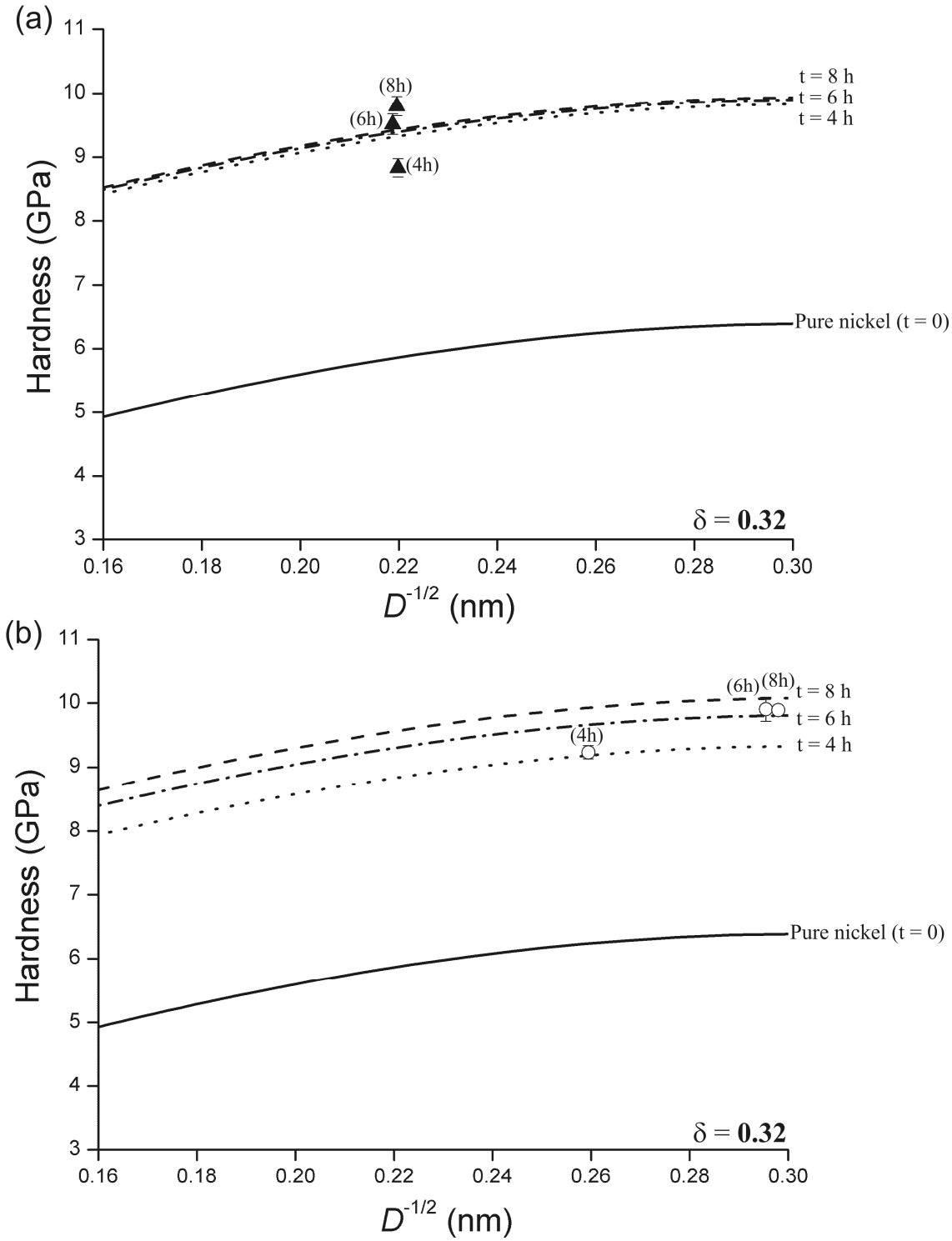

Figure 4.12. Relation between Ni grain size and hardness calculated with the cumulative model. Experimental hardness values show reasonable agreement with the model for (a) Ni-10nD and (b) Ni-10G nanocomposites. Error bars frequently fall within the respective data point symbol.

Table 4.7. Experimental hardness and calculated hardness values. The relative error is also presented.

Conditions	Experimental *H* (GPa)	Calculated *H* (GPa)	Relative error (%)
as–milled Ni–10nD (4 h)	8.83	9.32	5.54
as–milled Ni–10nD (6 h)	9.51	9.38	1.41
as–milled Ni–10nD (8 h)	9.79	9.43	3.80
as–milled Ni–10G (4 h)	9.23	9.19	0.52
as–milled Ni–10G (6 h)	9.90	9.80	0.10
as–milled Ni–10G (8 h)	9.89	10.05	1.66

Figure 4.13 compares the individual contributions of the strengthening mechanisms. In agreement with the results obtained for the Cu-based composites, grain refinement proved to be a major effect for both composite types, by inducing average hardness increments of 4.6 GPa for Ni-10nD and 5.1 GPa for Ni-10G, and is followed by solid solution hardening with 3 GPa for Ni-10nD and 3.5-4 GPa for Ni-10G. The average increment resulting from the second-phase reinforcement is 0.73 GPa for the Ni-10nD and 0.003 GPa for the Ni-10G. The solid solution contribution increased significantly with milling time in the Ni-10G material due to the higher fraction of dissolved carbon in the metallic matrix (see Table 4.4). This effect was not so noticeable in the Ni-10nD nanocomposite due to the higher milling stability of the carbon allotrope.

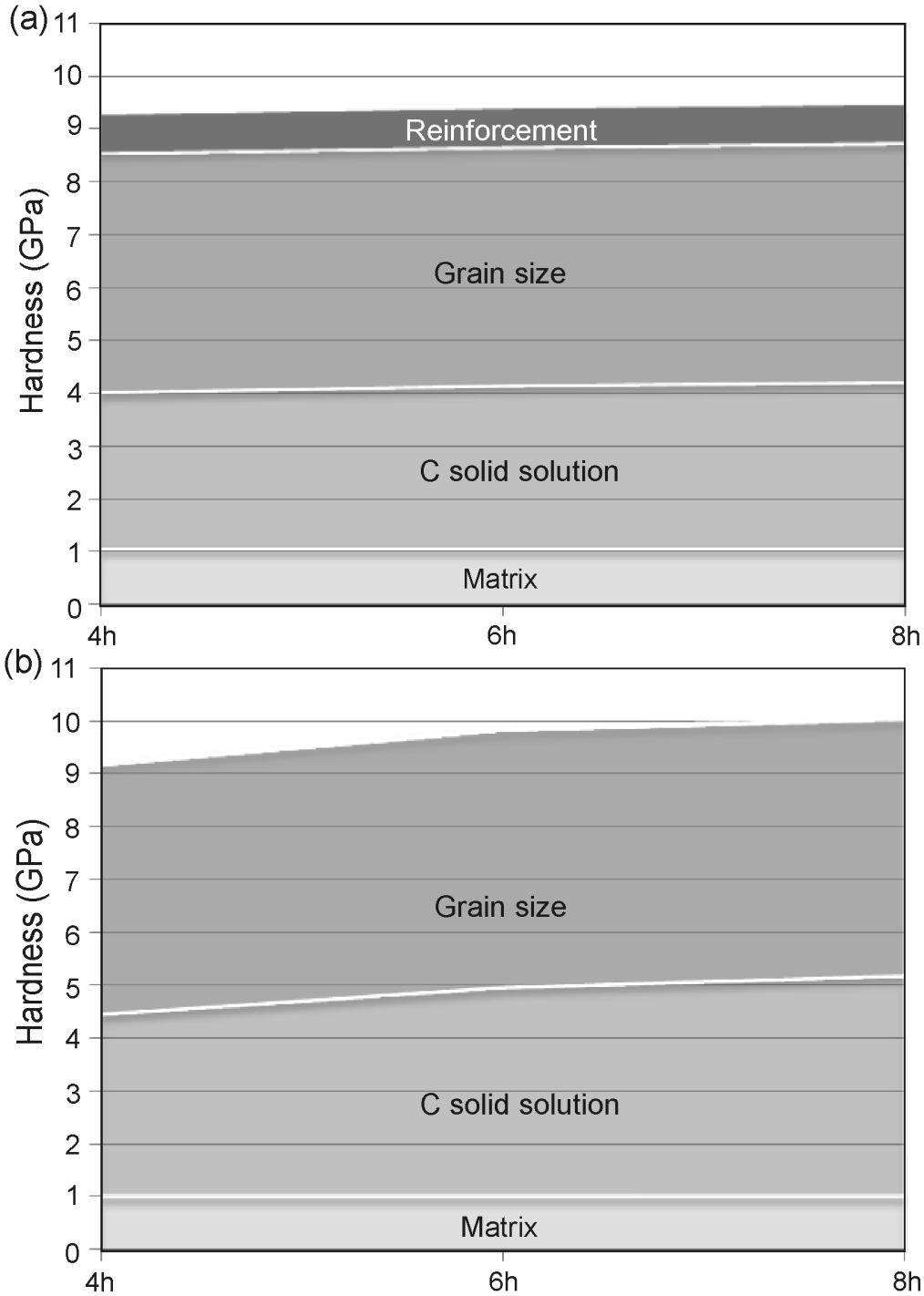

Figure 4.13. Contribution of each strengthening mechanism for milling times of 4, 6, and 8 h. (a) Ni-10nD and (b) Ni-10G nanocomposites.

4.3 Summary

The microstructural observations showed well-dispersed carbon particles in a nanostructured nickel matrix. Preservation of the nD crystalline structure during high-energy milling with Ni was demonstrated by XRD, electron diffraction and Raman spectroscopy, while an essentially amorphous nature was inferred for graphite in the as–milled Ni-10G materials. Graphitization of the carbon phases occurred progressively during annealing at 973 and 1073 K for both composite types. The process was assisted by the structural defects induced by milling and possibly by a Ni doping effect. Grain boundary pinning by nanoparticles or a solute drag effect could not effectively ensure microstructural thermal stability of the Ni–nD and Ni–G composites during heat-treatments at 973 and 1073 K. A remarkable 70% hardness increase has been achieved for both as-milled nanocomposites over pure Ni. The lattice parameter variation indicates that solid solution is active mainly in the Ni-10G material. A cumulative model has been used to analyze the contribution of the several strengthening mechanisms. The major contribution resulted from grain refinement, while the additional hardness increase over that of pure nanostructured nickel was attributed to carbon solid solution in both composite types, and to second-phase reinforcement in the nD composites. The Orowan effect has been assumed to be inoperative and the substitutional solute atoms arising from milling media contamination proved have a negligible strengthening effect in both composite types.

4.4 References

[1] C. Suryanarayana, Prog. Mater. Sci. 46 (2001) 1–184.

[2] J. Weissmuller, J. Markmann, Adv. Eng. Mater. 7 (2005) 203–207.

[3] A. Undisz, U. Zeigmeister, M. Rettenmayr, M. Oechsle, J. Alloys Comp. 438 (2007) 178–183.

[4] N.S. Xu, J. Chen, S.Z. Deng, Diamond Relat. Mater. 11 (2002) 249–256.

[5] M. Singleton, P. Nash, J. Phase Equilib. 10 (1989) 121–126.

[6] Z. Qiao, J. Li, N. Zhao, C. Shi, P. Nash, Scripta Mater. 54 (2006) 225–229.

[7] V.L. Kuznetsov, Y.V. Butenko, Synthesis, Properties and Applications of Ultrananocrystalline Diamond NATO Science Series 192 (2005) 199–216.

[8] B. Bokhonov, M. Korchagin, J. Alloys Compd. 333 (2002) 308–320.
[9] R. Anton, Carbon 46 (2008) 656–662.
[10] O.P. Krivoruchko, VI. Zaikovskii, Mendeleev Commun 8 (1998) 97–100.
[11] T.D. Shen, W.Q. Ge, K.Y. Wang, M.X. Quan, J.T. Wang, W.D. Wei, C.C. Koch, Nanostructured Mater. 7 (1996) 393–399.
[12] A.C. Ferrari, J. Robertson, Phil. Trans. R. Soc. Lond. A 362 (2004) 2477–2512.
[13] R. Pfeiffer, H. Kuzmany, P. Knoll, S. Bokova, N. Salk, B. Gunther, Diamond Relat. Mater. 12 (2003) 268–271.
[14] H. Kuzmany, R. Pfeiffer, N. Salk, B. Günther, Carbon 42 (2004) 911–917.
[15] D. Zhang, R.Q. Zhang, J. Phys. Chem. B 109 (2005) 9006–9013.
[16] I. Gouzman, O. Fuchs, Y. Lifshitz, Sh. Michaelson, A. Hoffman, Diamond Relat. Mater. 16 (2007) 762–766.
[17] J. Qian, C. Pantea, J. Huang, T.W. Zerda, Y. Zhao, Carbon 42 (2004) 2691–2697.
[18] M. Yoshikawa, Y. Mori, H. Obata, M. Maegawa, G. Katagiri, H. Ishida, A. Ishitani, Appl. Phys. Lett. 67 (1995) 694–696.
[19] Q. Zou, Y.G. Li, B. Lv, M.Z. Wang, L.H. Zou, Y.C. Zhao, Inorganic. Mater. 46 (2010) 127–131.
[20] J.B. Correia, V. Livramento, N. Shohoji, E. Tresso, K. Yamamoto, T. Taguchi, K. Hanada, E. Ōsawa, Mater. Sci. Forum 587 (2008) 443–447.
[21] M.T.Marques, J.B. Correia, J.M. Criado, M.J. Diánez, P.Matteazzi, Key Eng. Mater. 230–232 (2002) 652–655.
[22] J.B. Correia, M.T. Marques, P.A. Carvalho, R. Vilar, J. Alloys Compd. 434–435 (2007) 301–303.
[23] M. Zhao, J.C. Li, Q. Jiang, J. Alloys Compd. 361 (2003) 160–164.
[24] J. Kaspar, P. Fornasiero, G. Balducci, R. Di Monte, N. Hickey, V. Sergo, Inorg. Chim. Acta 349 (2003) 217–226.
[25] B. Ghosh, H. Dutta, S.K. Pradhan, J. Alloys Compd. 479 (2009) 193–199.
[26] T. Tanaka, K.N. Ishihara, P.H. Shingu, Metall. Trans. A 23A (1992) 2431–2435.
[27] B.D. Cullity, Elements of X Ray Diffraction, 2nd edition, Addison-Wesley Publishing Company, 1978.
[28] A.B. Ziya, K. Ohshima, J. Alloys Compd. 425 (2006) 123–128.
[29] H. Li, F. Ebrahimi, Mater. Sci. Eng. A347 (2003) 93–101.
[30] T.Y. Chan, S.T. Lin, J. Mater. Sci. 32 (1997) 1963–1967.

[31] L. Zwell, E.J. Fasiska, Y. Nakada, A.S. Keh, Trans. Metall. Soc. AlME. 242 (1968) 765–766.

[32] E. Orowan, Symposium on Internal Stresses in Metals and Alloys, Institute of Metals, London; 1948, p. 451.

[33] X.L. Wu, Y.T., Zhu Appl. Phys. Lett. 89 (2006) 031922-1/3.

[34] J. Moon, S. Kim, J. Jang, J. Lee, C. Lee, Mater. Sci. Eng. A 487 (2008) 552–557.

[35] H. Sumiya, T. Irifune, Diamond Relat. Mater. 13 (2004) 1771–1776.

[36] A.R. Ranjbartoreh, B.Wang, X. Shen, G.Wang, J. Appl. Phys. 109 (2011) 014306/1-6.

[37] T. Oku, A. Kurumada, Y. Imamura, M. Ishihara, J. Nuclear Mater. 381 (2008) 92–97.

[38] Q. Zou, Y.G. Li, B. Lv, M.Z. Wang, L.H. Zou, Y.C. Zhao, Inorganic. Mater. 46 (2010) 127–131.

[39] A.C. Ferrari, J. Robertson, Phys. Rev. B 61 (2000) 14 095/107.

[40] A.E. Ghazi, S.E. Hajji, L. Giraud, S. Gratton, J. Comp. Appl. Math. 219 (2008) 398 – 407.

[41] M.X. Chen, X.H. Song, Z.Y. Gan, S. Liu, Nanotech. 22 (2011) 345704-1/6.

Chapter 5

Chapter 5 – Tungsten-nanodiamond composites

Nanodiamond and graphite have been milled with tungsten to produce, respectively, W–nD and W-G composite powders, while pure tungsten has been used as control. The major challenge in the tungsten-carbon composites lies in the dispersion of carbon particles in the metallic matrix while keeping the carbide reaction at a minimum. Processing windows for carbide minimization have been established by a systematic variation of the carbon phase fraction, milling energy and milling time, moreover the influence of the carbon allotrope on the formation of W carbides has been studied. Differential thermal analysis has been used to evaluate the composites thermal stability. As-milled W-40nD material has been consolidated by spark plasma sintering. Structural changes and carbide formation induced by milling and annealing have been investigated by X-ray diffraction and by scanning and transmission electron microscopy. The tungsten matrix of the W–20nD composite has been chemically dissolved to allow for a detailed analysis of the milled carbon phase. The strength level has been evaluated through microhardness tests.

5.2 Results and discussion

W–10nD, W-20nD, W–10G and W-20G composites were prepared by ball milling at a rotation speed of 200 rpm for milling times of 2 and 4 h. A higher nD fraction (40 at.% C) has been selected to evaluate the effect of milling energy on carbide formation using rotation speeds of 200, 300 and 400 rpm and milling times of 2 and 4 h. Pure W, milled at a rotation speed of 200 rpm for 4 h, has been used as control.

DTA measurements for the W-20nD material milled have been carried out. The W-40nD material milled at 200 rpm for 4 h has been consolidated by spark plasma sintering at a temperature of 1073 K and under a load of 400 MPa for 3 min.

X-Ray Diffraction

The study of the influence of carbon fraction on carbide formation milling experiments has been carried out using a rotation speed of 200 rpm and 4 h of milling time for mixtures of W with 10, 20 and 40 at.% nD, and a mixture of W with 20 at.% G. Pure W was used as control. Figure 5.1 presents diffractograms of the milled materials, where the intense tungsten peaks and the corresponding background level obscured the carbon phases. WC could be detected in all materials, while W_2C was present only in the nanocomposites (Figure 1 (b) to (f)). Since the carbide formation sequence is W➔W_2C➔WC [1], the WC in the composite materials is expected to originate essentially from milling media wear [2], as attested by the residual presence of this carbide in the milled pure W (Figure 5.1 (a)). The WC contamination increases with the carbon fraction and is higher for nD than for G, which is an indication of the hardness level attained during milling. The slightly higher presence of W_2C detected in the W-20G material as compared with that of W–20nD (Figure 5.1 (c) *vs* (e)) demonstrates a higher dissolution rate and lower milling stability for the softer allotrope, in agreement with the results obtained for the Cu and Ni matrices.

The effect of milling energy on carbide formation has been investigated using W–nD mixtures with 40 at.% C to better evidence the possible presence of W_2C and/or WC formed by reaction milling. Figure 5.2 shows diffractograms for materials processed at 200 rpm (for 2 and 4 h), 300 rpm (for 2 h) and 400 rpm (for 2 h). Modest amounts of WC were present in the materials milled at 200 rpm, with a slight increase for higher milling time; whereas W_2C could only be detected after 4 h of milling at 200 rpm (Figure 5.2 (a) and (b)). Higher milling energy resulted in extensive carbide formation consistent with the W➔W_2C➔WC sequence [1], with a major presence of W_2C at 300 rpm and a conspicuous conversion to WC at 400 rpm (compare Figure 5.2 (c) and (d)). The present results show that there is an energy threshold below which carbide presence is incipient, i.e., rotations of 200 rpm are capable of producing W–nD composites by preventing extensive W carbide conversion while minimizing WC contamination from milling media.

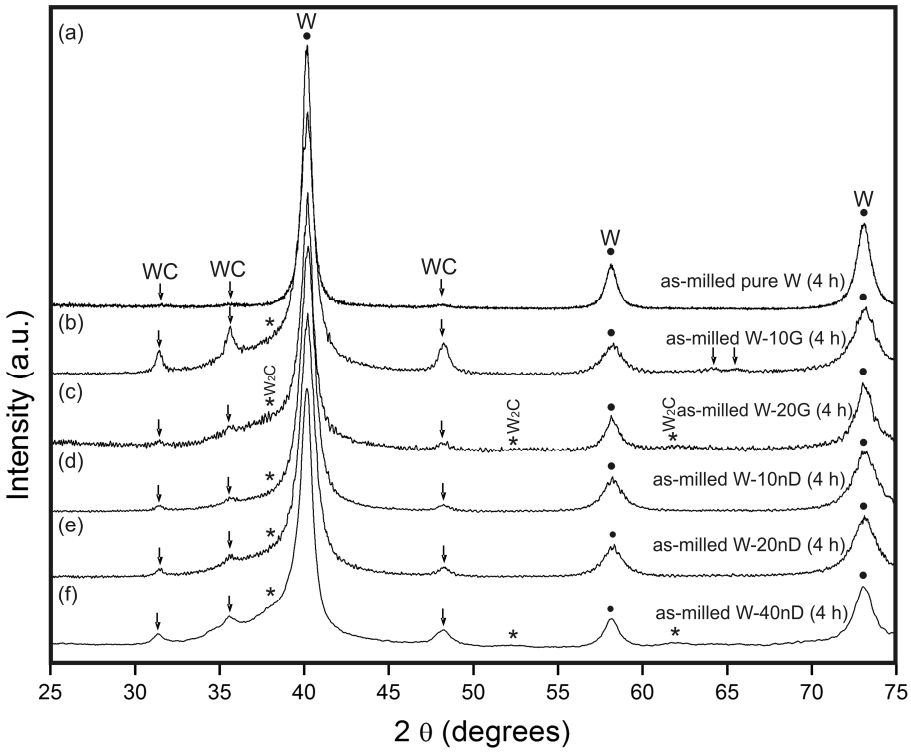

Figure 5.1. Experimental X-ray diffractograms of pure W (a), W–G (10 and 20 at.%) (respectively, (b) and (c)), and W–nD (10, 20 and 40 at.%) (respectively, (d), (e) and (f)) after milling at 200 rpm for 4 h.

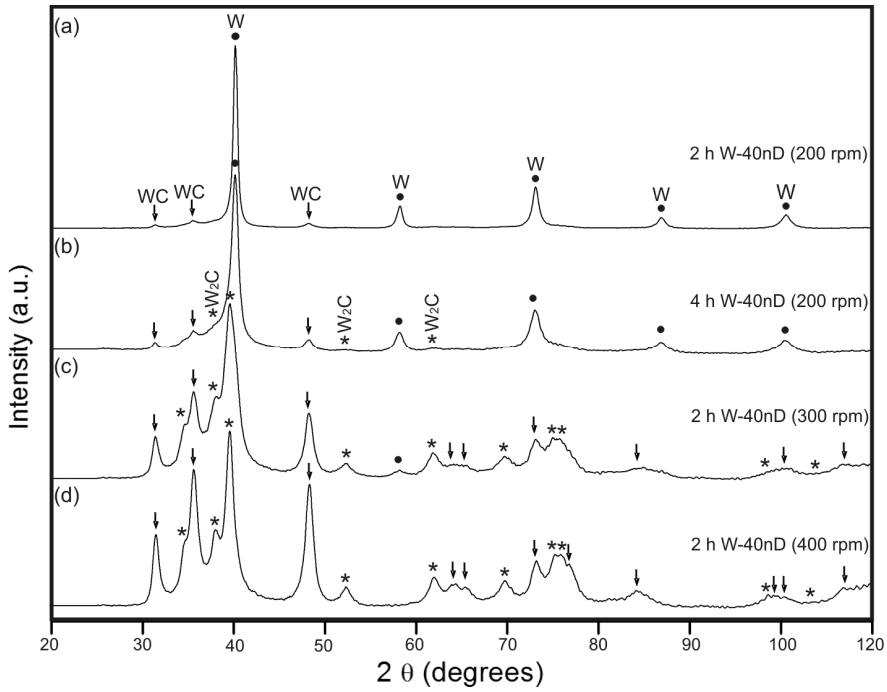

Figure 5.2. Experimental X-ray diffractograms of W-40nD milled for 2 h at 200 rpm (a), 4 h at 200 rpm (b), 2 h at 300 rpm (c) and 2 h at 400 rpm (d).

Microstructural observations

Heterogeneous structures resulting from insufficient milling have been observed for milling times of 2 h at 200 rpm, while longer milling resulted in soundly welded composite powders (Figure 5.3 (a) *vs* (b)). Sub-micrometer sized carbide inclusions with a slightly darker contrast could be detected in materials milled at 200 rpm (see arrows in Figure 5.3 (b)). Residual traces of cobalt originating from milling media wear have been found by EDS in all milled materials, attesting for an essentially exogenous source of the WC detected in Figure 5.1 (a) to (f) and Figures 2 (a) and (b). Milling at 200 rpm for 4 h has been established as the best trade-off between homogeneity maximization and carbide minimization. Soundly welded composite powders have also been observed in the W-20G material milled at 200 rpm for 4 h, however evident carbide inclusions have not been inferred from SEM results supporting the lower hardness level attained during milling for the W-20G material resulting in lower milling media contamination (Figure 5.3 (c)).

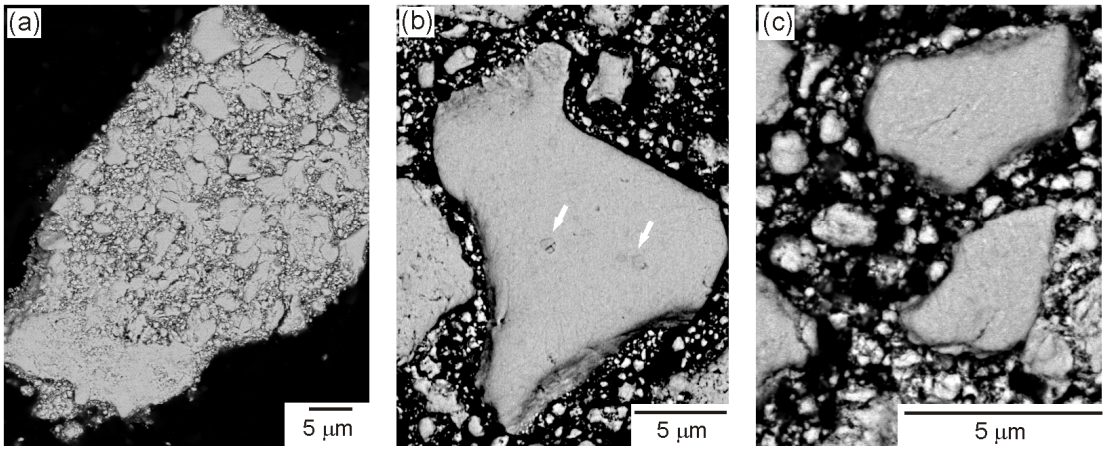

Figure 5.3. BSE SEM images of the W-20nD milled at 200 rpm for (a) 2 h or (b) 4 h. W-20G milled at 200 rpm for 4 h (c). The arrows indicate the W carbide inclusions.

TEM observation of composite powders milled at 200 rpm for 4 h showed nanometric grains with mottled contrast and ill-defined boundaries, characteristic of high-energy non-equilibrium states induced by intense deformation (Figure 5.4 (a)). Carbon nanoparticles, readily identifiable due to their low atomic number contrast (see arrows in Figure 5.4 (a)), presented sizes in the 5-10 nm range and were homogeneously dispersed in the metallic matrix. Due to their low volume fraction carbide particles could not be

detected in TEM micrographs or electron diffraction patterns of the composite materials (Figure 5.4 (b)).

The intense scattering by the metallic matrix hindered a detailed investigation on the embedded carbon particles, which could only be further scrutinized after W etching. TEM observation of the extracted material showed a high proportion of 5-20 nm particles presenting the diamond structure (Figure 5.4 (c) and (d)), as well as individual W_2C particles, with diameters in the 20-50 nm range (Figures 5.4 (e) and (f)). The W_2C particles resulting from the carbide reaction have thus much smaller size than the carbide inclusions originating from milling media contamination (see Figure 5.3 (b)).

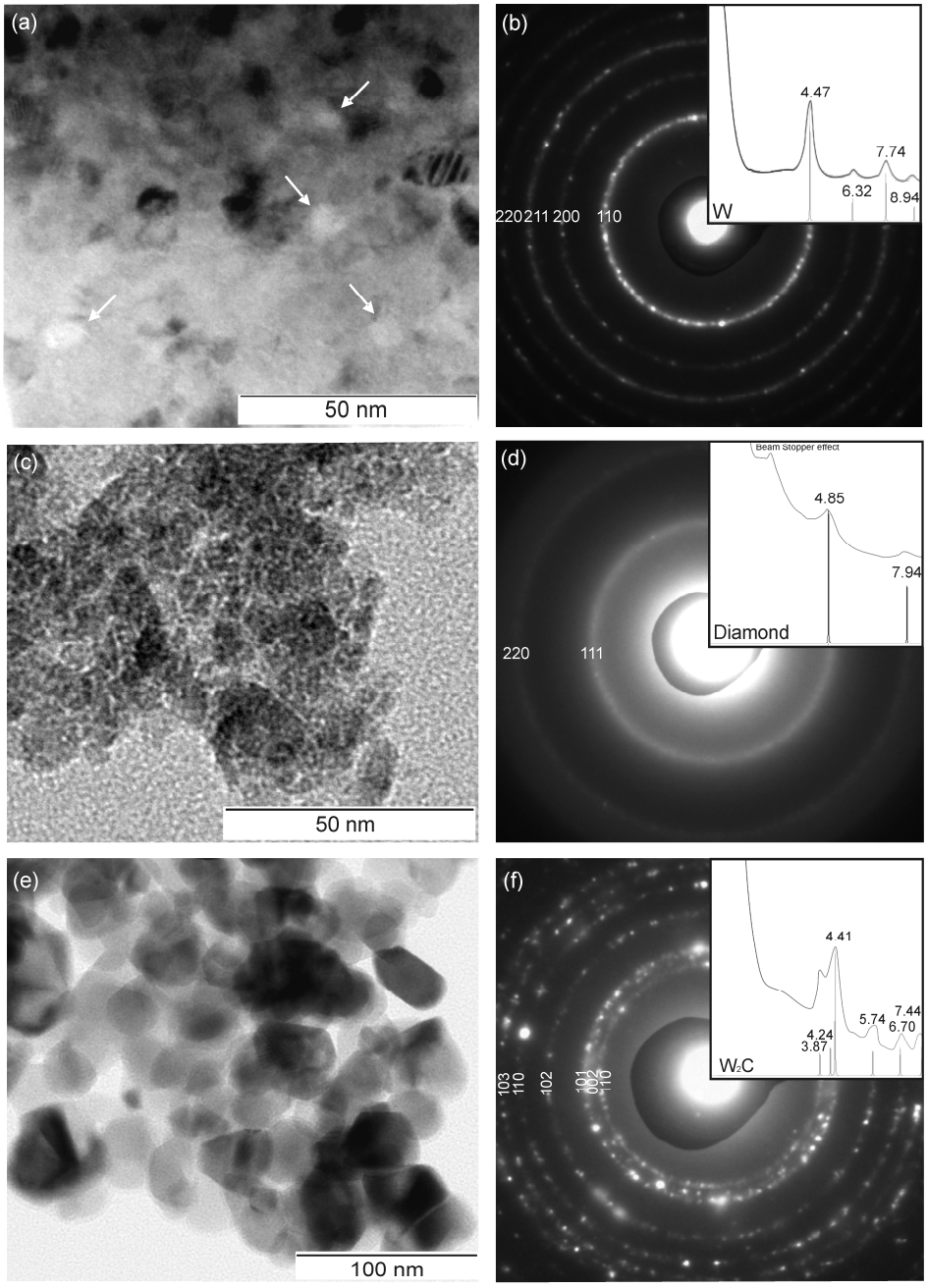

Figure 5.4. (a) Bright-field TEM image of the W–20nD material milled for 4 h at 200 rpm. (b) Diffraction pattern obtained from a large area similar to (a) with integrated radial profile (W simulation included with legend in nm^{-1}). The arrows indicate low–atomic number regions. Bright-field TEM images of the particles extracted from the milled W–20nD composite showing both nD (c) and W_2C particles (e). (d) Ring diffraction pattern obtained from a large area similar to (c) with integrated radial profile (diamond simulation included with legend in nm^{-1}). (f) Ring diffraction pattern obtained from a large area similar to (e) with integrated radial profile (W_2C simulation included with legend in nm^{-1}).

Consolidated material

Figure 5.5 shows a representative microstructure of the W–40nD composite consolidated by spark plasma sintering. In contrast to the Cu-0.1Cr-10nD material consolidated under identical SPS conditions (1073 K under a load of 400 MPa), the W-40nD is highly porous with no evidence for prior powder boundaries responsible for bonding the Cu-0.1Cr-10nD powder.

An analogous study with tungsten and microdiamond demonstrated that SPS at 1423 K results in higher density although this temperature favors carbide formation [3]. Indeed, tungsten carbide is usually synthesized by direct reaction of tungsten and carbon at similar temperatures (1673-1873 K [1]). Consequently, in order to minimize carbide formation while maximizing densification, spark plasma sintering below 1200 K followed by hammer forging has been suggested [3-5]. This approach is valid for consolidation of W-nD composites such as the ones produced in the present study and is meant for future work.

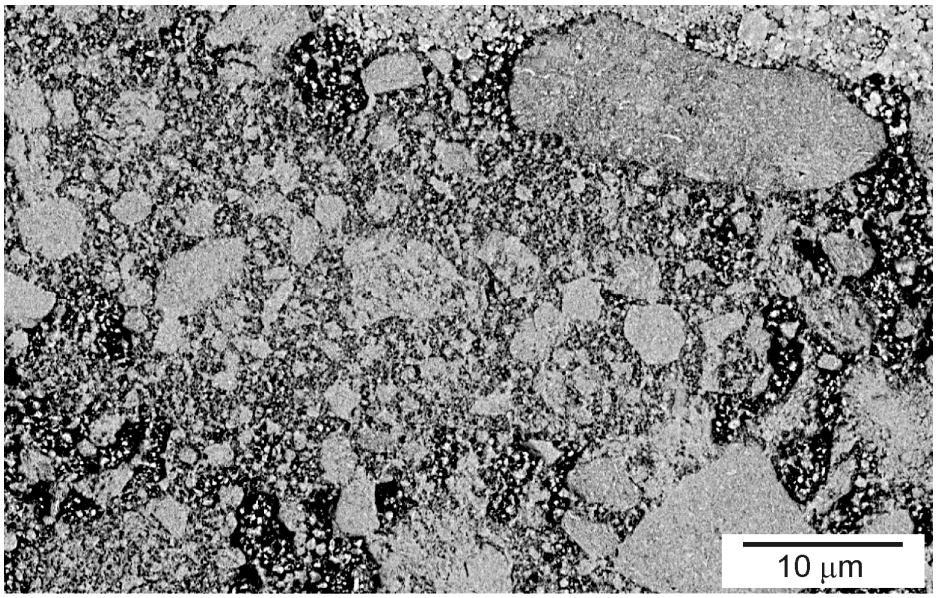

Figure 5.5. BSE SEM image of the W-40nD material milled at 200 rpm for 4 h and subsequently consolidated by spark plasma sintering.

Strength and thermal stability

Table 1 lists the microhardness values for pure W, W–G (20 at.% C) and W–nD (10, 20 and 40 at.% C) materials after milling at 200 rpm for 4 h. Microhardness values obtained after continuous heating up to 873 K at 20 $K.min^{-1}$ are also presented for pure W, W–20nD and W–20G. Due to the lack of homogeneity the strength of the consolidated material has not been investigated.

Dispersion of nD was expected to induce reinforcement of the metallic matrix due to the potential load bearing ability of diamond, while significant reinforcement was not anticipated for the graphite dispersion due to the soft nature of this phase. Yet all nanocomposites showed significant hardness increase over milled pure W: ~33 % for W–nD (10, 20 and 40 at.% C) and 17 % for W–G (20 at.% C). The hardening effect in the W–20G composite may be partially justified by the presence of carbides as well as by metastable C solubility. Nevertheless, it should also be noticed that graphite tends to amorphize during milling [6] and amorphous carbon with a high fraction of sp^2 bonds can attain hardness values as high as 20 GPa [7–9]. The similar hardness level attained by the 10, 20 and 40 at.% W–nD composites indicates that strength saturates for an nD fraction of about 10 at.% nD.

The heat exposed materials showed hardness levels comparable to the as-milled composites attesting for high thermal stability up to 873 K, while the DTA curves evidenced a stable chemistry up to about 1200 K (see Figure 5.6).

Table 5.1. Microhardness values of pure W and W–G and W–nD materials milled at 200 rpm. Pure W, W–20nD and W–20G exposed to continuous heating up to 873 K at 20 $K.min^{-1}$ are also presented.

Conditions	Vickers Microhardness (GPa)
as-milled Pure W (4 h)	16.1 ± 0.8
as-milled W–20G (4 h)	18.9 ± 0.6
as-milled W–10nD (4 h)	21.1 ± 1.1
as-milled W–20nD (4 h)	21.4 ± 1.1
as-milled W–40nD (4 h)	21.6 ± 1.3
4 h as-milled pure W and heated up to 873 K	15.8 ± 1.1
4 h as-milled W–20G and heated up to 873 K	20.1 ± 1.1
4 h as-milled W–20nD and heated up to 873 K	21.7 ± 1.2

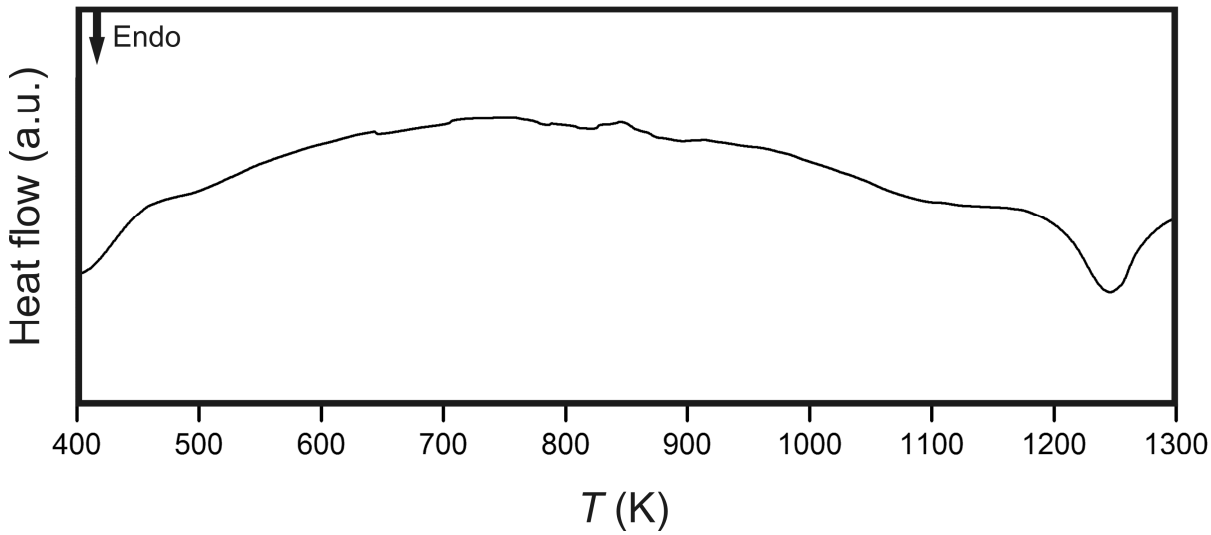

Figure 5.6. DTA heating curve of the W–20nD material milled at 200 rpm for 4 h.

5.3 Summary

W–nD and W–G composites can be processed by mild-energy milling at 200 rpm with 4 h of milling time. These conditions allow producing nanostructured metallic matrices with well-dispersed carbon particles, while keeping at a minimum both carbide formation and contamination by milling media. The materials produced present a remarkable strength increase over that of pure tungsten and are thermally stable under the conditions studied. Ensuing consolidation involving techniques such as spark plasma sintering is expected to preserve the nanostructured nature of the materials, however a compromise between carbide formation and full densification must be established in order to achieve tailored W consolidated composites.

5.4 References

[1] G. Wang, S.J. Campbell, A. Calka, W.A. Kaczmarek, J. Mater. Sci. 32 (1997) 1461–1467.

[2] C. Suryanarayana, Prog. Mater. Sci. 46 (2001) 1–184.

[3] V. Livramento, D. Nunes, J.B. Correia, P.A. Carvalho, U. Mardolcar, R. Mateus, K. Hanada, N. Shohoji, H. Fernandes, C. Silva, E. Alves, J. Nuclear Mater. 416 (2011) 45–48.

[4] D. Nunes, V. Livramento, J.B. Correia, R. Mateus, P.A. Carvalho, N. Shohoji, H. Fernandes, C. Silva, E. Alves, K. Hanada, E.Osawa, Proceedings of MRS Symposium R on Materials for Future Fusion and Fisson Technologies, MRS Symposium Proceedings Series, Materials Research Society 1125 (2009) 59–64.

[5] V. Livramento, J.B. Correia, D. Nunes, P.A. Carvalho, H. Fernandes, AIP Conference Proceedings 996 (2008) 166–171.

[6] T.D. Shen, W.Q. Ge, K.Y. Wang, M.X. Quan, J.T. Wang, W.D. Wei, C.C. Koch, Nanostructured Mater. 7 (1996) 393–399.

[7] F.C. Marques, R.G. Lacerda, Brazilian J. Phys. 30 (2000) 527–532.

[8] V. Kulikovsky, V. Vorlícek, P. Bohác, A. Kurdyumov, A. Deyneka, L. Jastrabík, Diamond Relat. Mater. 12 (2003) 1378–1384.

[9] D.L. Baptista, F.C. Zawislak, Diamond Relat. Mater. 13 (2004) 1791–1801.

Chapter 6

Chapter 6 – Transformation of nanodiamond into onion-like carbon

6.1 Introduction

Ball milling of nanodiamond in the presence of metals influences the subsequent transformation of this allotrope into onion-like carbon at high temperatures. The effect of 20 at.% copper, nickel or tungsten on the subsequent transformation of milled nanodiamond has been scrutinized up to 1773 K through differential thermal analysis. Structural changes induced both by milling and heating have been investigated by X–ray diffraction, transmission electron microscopy and Raman spectroscopy. Carbide conversion and milling media contamination have been evaluated. In a parallel study, the in situ transformation of nanodiamond into onion-like carbon within a Ni-10nD composite has been investigated through extraction of the carbon phase after exposure of the whole material to high temperature.

6.2 Results and discussion

Nanodiamond powder has been milled with 20 at.% of Cu, Ni or W at a rotation speed of 200 rpm during 4 h as these milling parameters typically represent the best trade-off between structural homogenization, milling media contamination and carbide prevention. The materials produced are designated, respectively, by nD(Cu), nD(Ni) and nD(W). Exposure to high temperature has been carried out through DTA by heating at 20 $K.min^{-1}$ up to temperatures varying from 1323 to 1773 K. The transition of pristine (non-milled) nD to onion like carbon has also been investigated for control. XRD measurements have been used to assess the presence of oxides and carbides in the milled and subsequently heat-exposed materials. This data assisted the identification of the transitions observed in DTA curves. Direct evidence for onion-like structures has been obtained by TEM observation. The OLC fingerprint obtained by Raman spectroscopy has been used to confirm the transition temperatures.

Nanodiamond to OLC transition

The transformation of nD particles into OLC involves: (i) formation of graphite sheets at peripheral regions, (ii) connection and curvature of these sheets at the edges of diamond $\{111\}$ planes with ensuing closure and (iii) inward progression of the transformation (see OLC formation scheme in Figure 1.1, Chapter 1) [1]. Diamond nanoparticles have dangling sp^3 bonds at the surface, thus their elimination and enclosure by graphite sheets with their in plane sp^2-hybridized bonds results in a decrease of the surface energy, which has been hypothesized as the driving force to continuously form graphite shells [2]. This transformation requires heating the nD particles at temperatures above 1400 K due to the high energy required to keep on breaking C–C bonds in inner diamond [2].

The heat flow curves and their time derivatives, which help to identify subtle transitions, are presented in Figure 6.1 (gray and dark lines, respectively). The XRD data is shown in Figure 6.2. TEM micrographs and electron diffraction patterns of as-milled and heat-exposed materials are exhibited in Figures 6.3 and 6.4, respectively. The Raman spectra with subsequent heat treatments for pristine nD and for milled materials are presented in Figure 6.5. Contamination due to milling media wear has been assessed through the amount of Fe present as determined by EDS point analyses shown in Table 6.1.

Table 6.1. Milling media contamination for 4h of milling time and 200 rpm (average of 10 EDS point analyses).

Material	Fe (at.%)
nD(Cu)	0.2
nD(Ni)	0.1
nD(W)	0.9

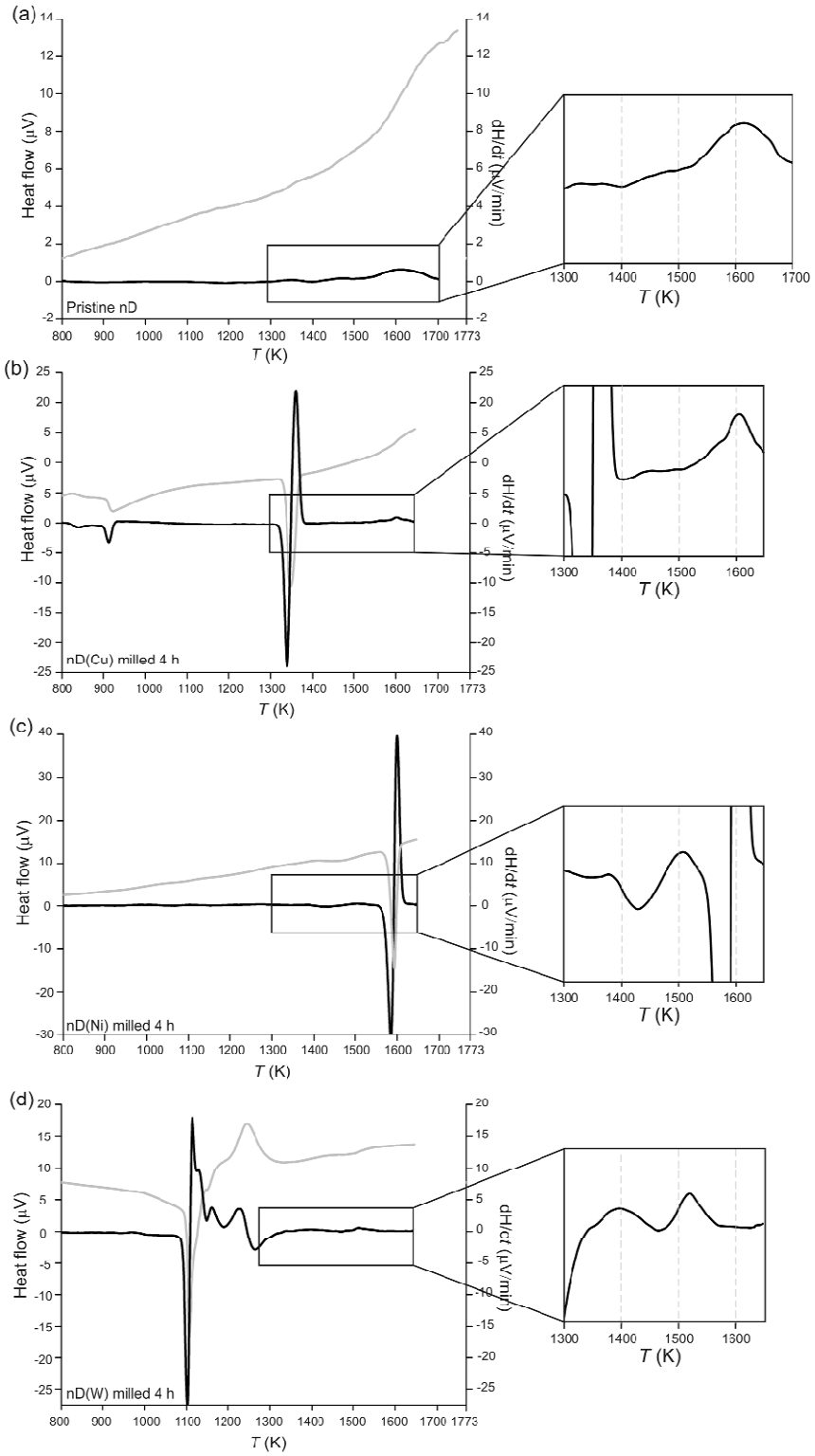

Figure 6.1. DTA measurements of the materials milled at 200 rpm for 4 h and pristine nD used as control. (a) Pristine nD, (b) nD(Cu), (c) nD(Ni) and (d) nD(W) materials. DTA curves appear as gray lines and the derivative curves as dark lines. Insets are included for identification of the carbon phase transitions.

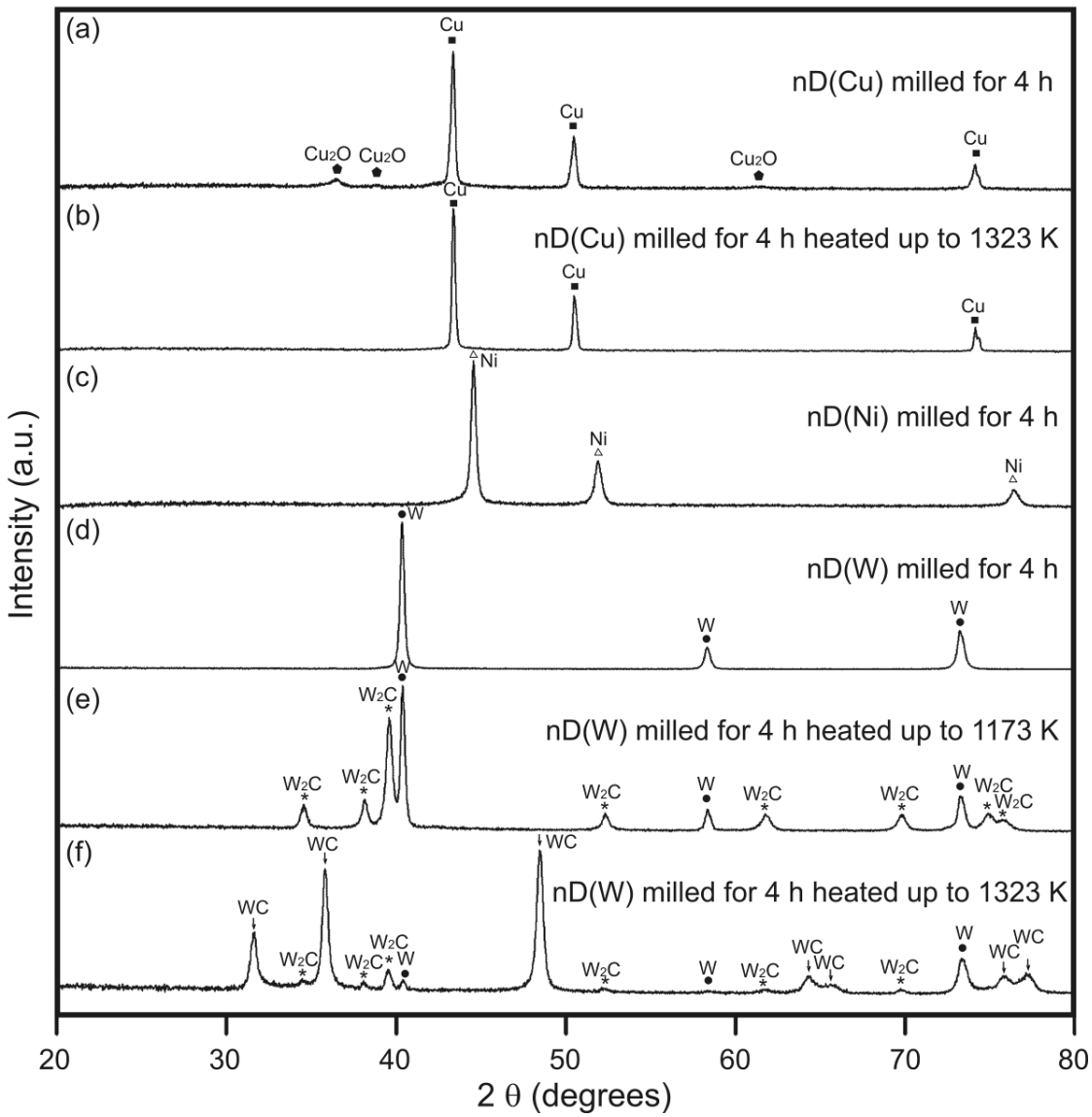

Figure 6.2. Experimental X-ray diffractograms of the materials milled at 200 rpm for 4 h and subsequently heated: (a) nD(Cu), (b) nD(Cu) after DTA up to 1323 K, (c) nD(Ni), (d) nD(W), and (e) nD(W) heated up to 1173 K and (f) at 1323 K. The intense matrix reflections, and the corresponding background level, obscured the carbon phase peaks.

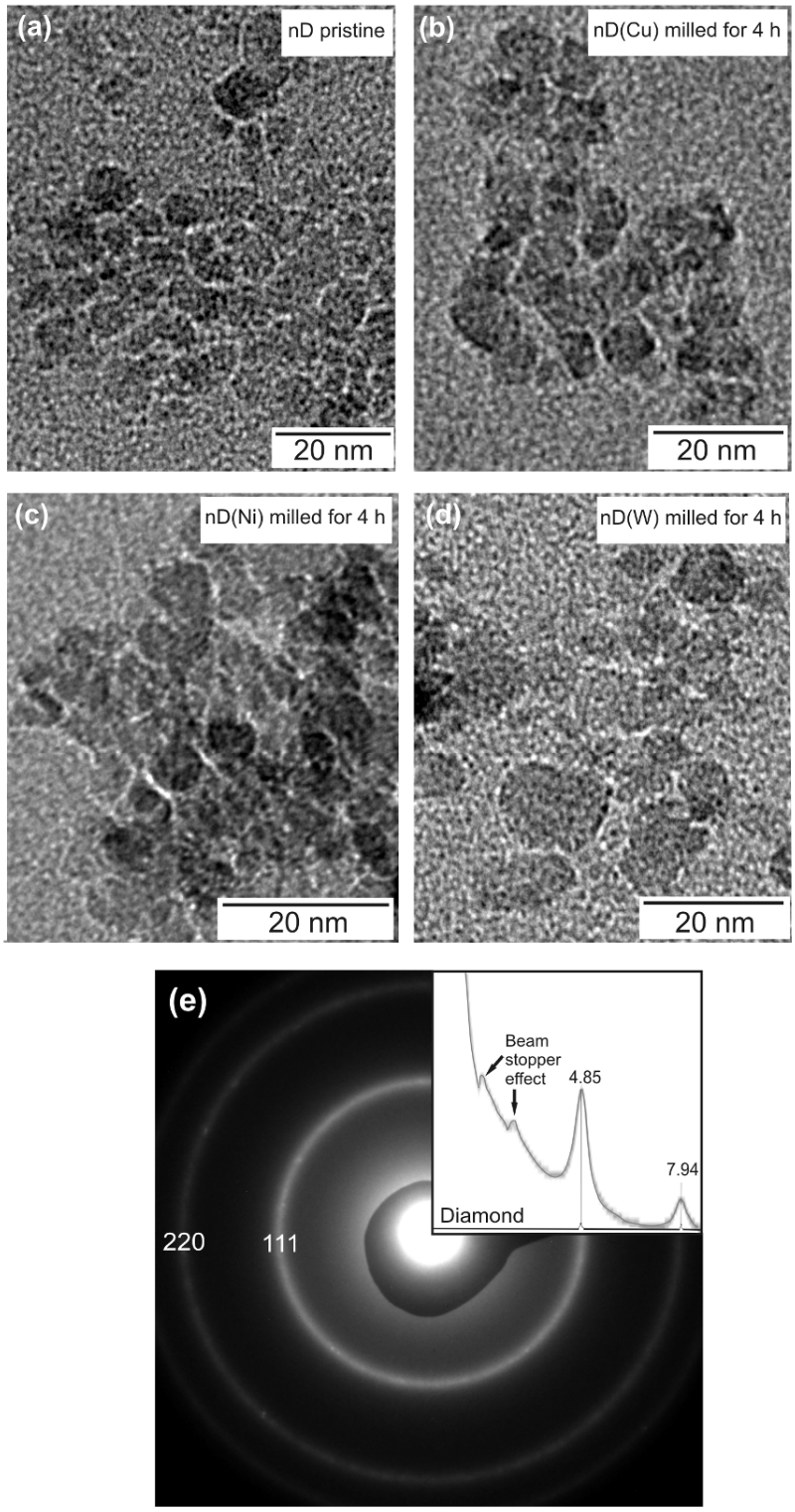

Figure 6.3. Bright-field TEM images of the carbon phases. (a) Pristine nD and as-milled (b) nD(Cu), (c) nD(Ni) and (d) nD(W) (d) showing particles with sizes in the 5-20 nm range. (d) Typical diffraction pattern of the nD particles with an integrated radial profile (diamond simulation included with legend in nm^{-1}).

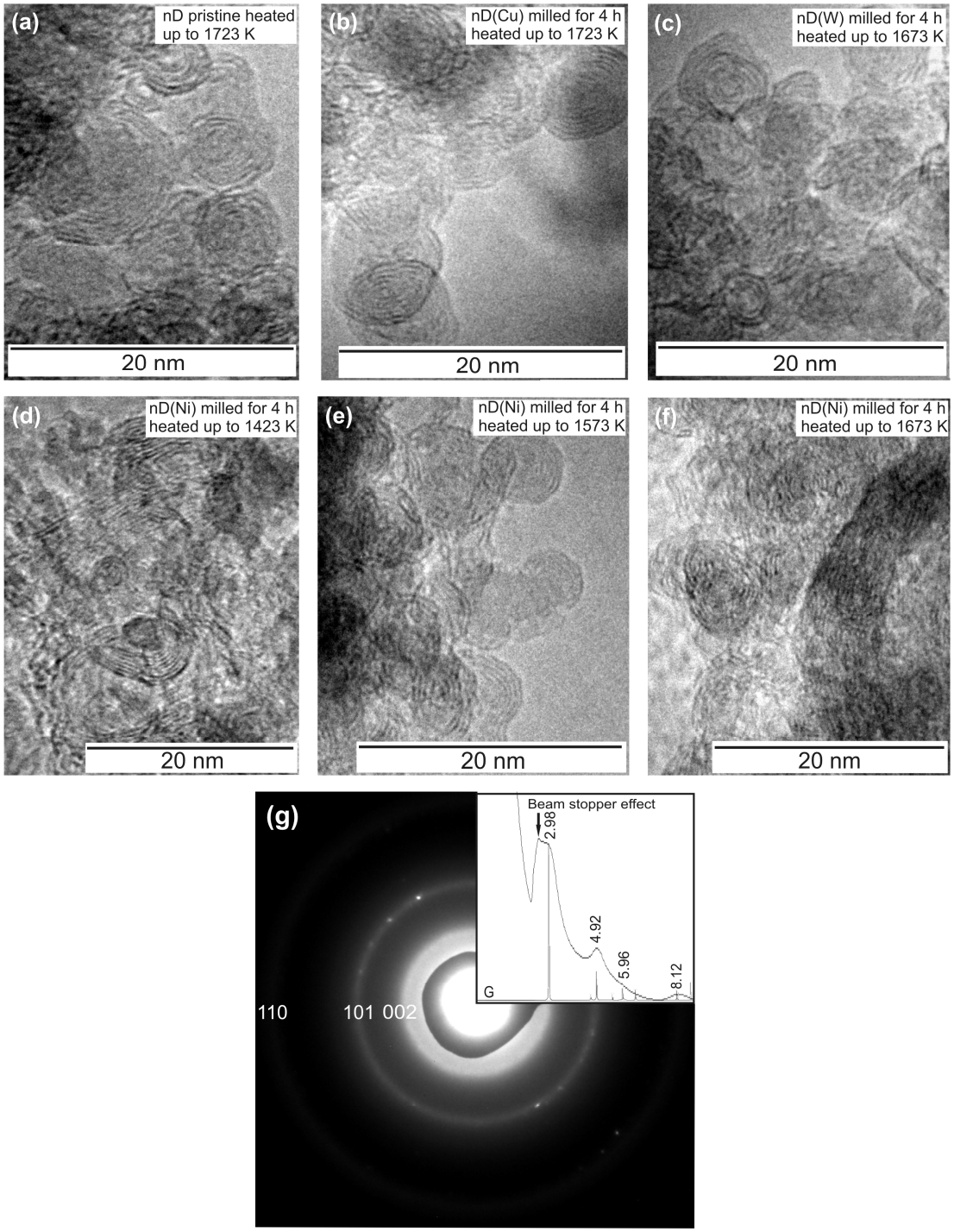

Figure 6.4. Bright-field TEM images of the heated-exposed materials. (a) Pristine nD powder heated up to 1723 K, (b) nD(Cu) up to 1723 K, (c) nD(W) up to 1673 K, (d) nD(Ni) up to 1423 K, (e) nD(Ni) up to 1573 K, (f) nD(Ni) up to 1673 K, and (g) characteristic diffraction pattern of the OLC particles with an integrated radial profile (graphite simulation included with legend in nm^{-1}).

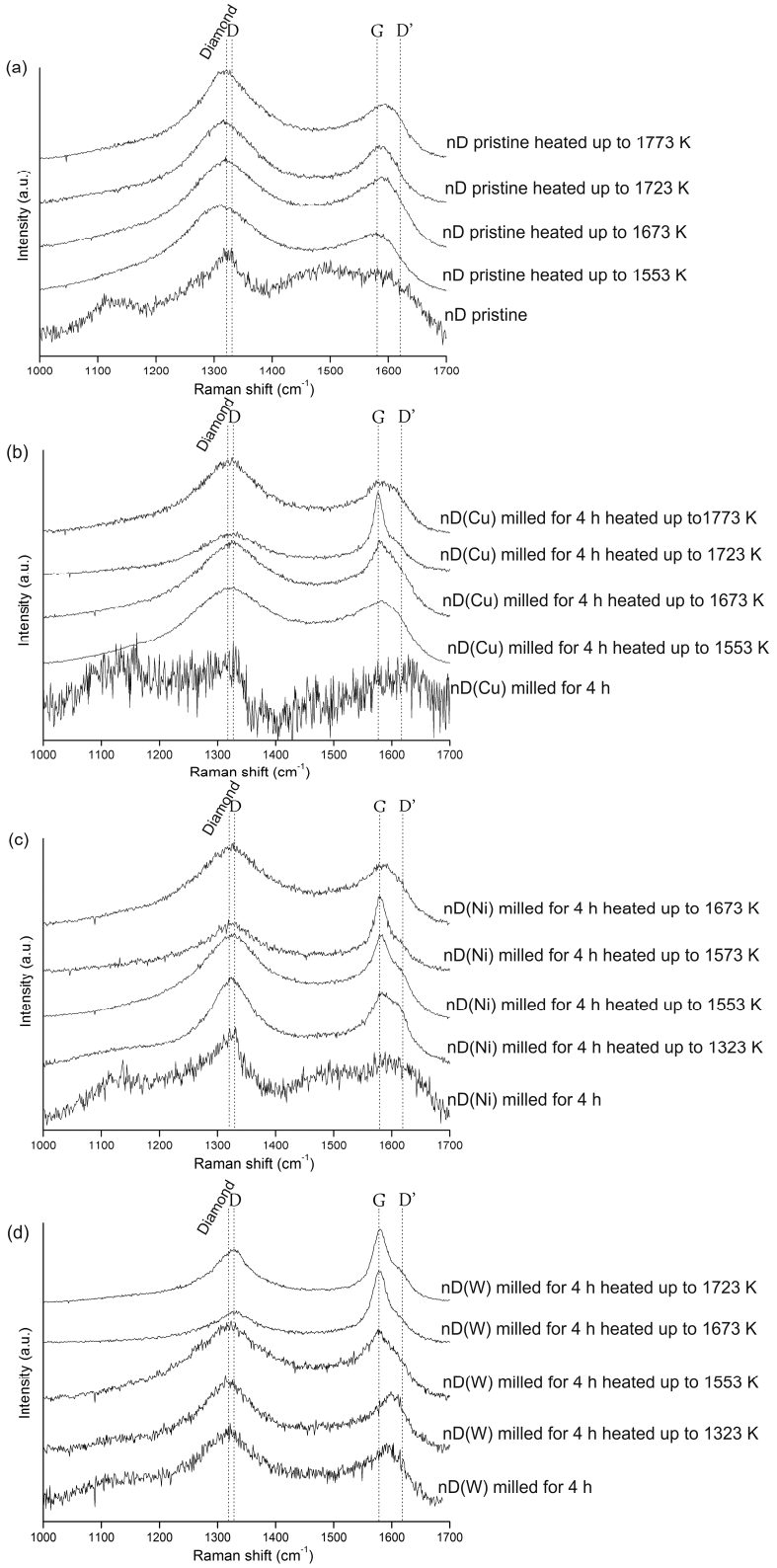

Figure 6.5. Raman spectra evolution with heat exposure for the (a) pristine nD, (b) nD(Cu), (c) nD(Ni) and (d) nD(W) materials.

The results presented in Figures 6.1 to 6.5 will be simultaneouly discussed below:

- The changes in heat flow observed for pristine nD (Figure 6.1 (a)) point to an apparently exothermic phase transformation into OLC (see Figure 6.4 (a)).
- The heat flow curve obtained for the milled nD(Cu) material clearly evidenced two endothermic transitions (Figure 6.1 (b)). The transition in the 800-1000 K range is associated with the reduction of Cu_2O (Figure 6.2 (a)), which probably originated from the partially oxidized Cu powder used in the mill charge. During heating this oxide is reduced by carbon into metallic Cu, as shown by the XRD data obtained after heating up to 1323 K where Cu_2O peaks are absent (Figure 6.2 (b)). The reduction of Cu_2O by carbon was investigated by Lee *et al*. [3], who showed that under vacuum metallic Cu starts to form at 673 K. The strong endothermic peak in the 1350-1400 K range corresponds to Cu melting (1358 K [4]). The derivative curve (see the inset in Figure 6.1 (b)) evidences also a subtle exothermic transition corresponding to the transformation of nD into OLC which is similar to the one observed for pristine nD (see magnified insets of Figures 6.1 (a) and (b)). These results show that milling nD in the presence of Cu does not dramatically affect the transition temperature.
- The heat flow curve obtained for the milled nD(Ni) material presented a strong endothermic peak in the 1550–1620 K range, which is likely to correspond to melting of a binary or ternary eutectic mixture (according to the Ni-C equilibrium phase diagram the Ni + C eutectic melts at 1600 K [5] and contaminants may lower the transformation temperature). The XRD data showed no evidence of NiO or Ni_3C (Figure 6.2 (c)). In any case, the Ni_3C carbide is unstable and decomposes at temperatures within 523-673 K [6], which is a range of temperatures substantially lower than the ones required to transform pure nanodiamond into onion-like carbon [1,2]. The derivative curve (see the inset in Figure 6.1 (c)) evidences a subtle endothermic transition corresponding to OLC formation as attested by the TEM observations after heating up to 1573 K (Figure 6.4 (e)). Comparison with Figure 6.1 (a) and (b) shows that milling with Ni tends to lower the OLC transformation by about 100 K. Furthermore, the transformation appears to have acquired an endothermic character.

- The heat flow curve obtained with the milled nD(W) material exhibits two strong peaks (Figure 6.1 (d)). XRD analysis could not detect WO_2, WO_3, WC or W_2C in the as-milled material (see Figure 6.2 (d)), however heat exposure resulted in extensive carbide formation: heating up to 1173 K induced the formation of W_2C with a still significant presence of metallic W (Figure 6.2 (e)); heating up to 1323 K resulted in intense WC peaks, although minor W_2C and W peaks were still detected (Figures 6.2 (f)). Thus, the endothermic peak in the 1090–1140 K range is consistent with W_2C formation, while the exothermic peak in the 1210–1290 K range is related to WC formation according to a $W \rightarrow W_2C \rightarrow WC$ sequence [7]. The derivative curve shows that the endothermic transformation associated with OLC formation is similar to the one observed for the nD(Ni) system (compare the insets in Figure 6.1 (c) and (d)).
- Significant contamination originating from milling media wear was expected to occur owing to the high hardness of the carbon allotrope used in the mixtures. Nevertheless, the fraction of Fe (Table 6.1) attested for a fairly low contamination and these results demonstrate that, at the nanoscale, diamond produces minimal wear due to a self-lubrication mechanism [8]. The higher iron content detected for nD(W) may be justified by the hardness difference between the DIN 1.4034 stainless steel and residual milling products such as hardened tungsten and tungsten carbide.
- TEM observations demonstrated that the nanodiamond structure was preserved during the milling operation for all metal dopants (see Figure 6.3). Depending on the maximum temperature imposed, all materials transformed into spherical OLC particles with diameters of about 5 nm. The OLC particles exhibited fringes with the typical (002) interplanar spacing of graphite (0.34 nm) and produced electron diffraction patterns compatible with the graphite structure (see Figure 6.4 (g)). The successive stages of the transformation are shown in Figure 6.4 for the Ni dopant: the graphite sheets formed initially do not always present a perfect onion-like structure (d), subsequently nearly perfect OLC particles can be found throughout the material (e) and eventually, at even higher temperatures, these structures are destroyed and tend to form entangled graphite sheets (f).

- The Raman spectra of the milled materials (bottom lines in Figures 6.5 (b-d)) are similar to that of pristine nD (Figure 6.5 (a)) showing that the materials remain stable during milling, in agreement with the TEM observations. The typical nanodiamond Raman spectrum displays a band at 1050-1200 cm^{-1} that is likely to correspond to *Trans*-polyacetylene, exhibiting Raman peaks at 1125 cm^{-1} and 1480 cm^{-1} [9]. The peak at ~1320 cm^{-1} corresponds to structural sp^3 vibrations and the observed downshift (~10 cm^{-1}) is related to the phonon confinement effect in nanoscale particles [10,11]. The broad band at 1400-1700 cm^{-1} is probably a convolution of the 1480 cm^{-1} *Trans*-polyacetylene peak and a sp^2 Raman peak originating from the outer graphite-like layers that envelope the diamond cores of nD powder [12,13]. Nevertheless, the milled nD(W) material become a mixture of diamond and sp^2 carbon phases (evidenced by the band at 1600 cm^{-1}). The sp^2 carbon peak is also associated with the presence of tungsten carbides formed during ball milling [14] (previously observed in W-20nD composite, Chapter 5). The excessive noise observed in Figure 6.5 (b) is attributed to the influence of oxides present in the milled nD(Cu) material (see Figure 6.2 (a)).
- The Raman results revealed that heat exposure eliminated *Trans*-polyacetylene from the pristine nD and milled materials. This conclusion has been corroborated by the DTA derivative curve insets presented in Figures 6.1 (a) and (b) that show minor broad bands from 1300-1500 K, which are expected to be related to the *Trans*-polyacetylene evaporation. During annealing treatment of pristine nD at 1073 K, the band associated to the *Trans*-polyacetylene was clearly present (see Chapter 4, Figure 4.6 (a)), however after heating up at 1553 K (Figure 6.5 (a)), no evidence of *Trans*-polyacetylene could be inferred. The increase of temperature caused a peak emerging from the 1530-1650 cm^{-1} band in the milled materials, which evolved towards the synthetic graphite Raman fingerprint. The phenomenon was previously demonstrated by Kuznetsov and Butenko [1] and by Obraztsova *et al.* [15] to represent the transition of nD particles into graphitic sheets that tend to close into OLC. The process for pristine nD culminates at 1800 K [1,15]. Nevertheless, higher temperatures tend to revert the transformation, and

the OLC particles transform into polygonized particles with hollow centers or graphite-like ribbons with parallel graphitic planes [1].

- The OLC fingerprint could not be clearly detected for the pristine nD heated up up at 1773 K. However, OLC particles have been observed at 1723 K (see Figure 6.4 (a)), in agreement with a transition onset at 1500 K (see Figure 6.1 (a)) and finish below 1773 K. The OLC fingerprint has been detected after heating the milled materials up to 1573, 1673 and 1723 K for, respectively, nD(Ni), nD(W) and nD(Cu). These results imply that the transition temperature is lowered by milling nD with metals, possibly due to the structural defects induced by milling associated to a catalytic effect of the metals, especially in the case of Ni. The presence of tungsten carbides and milling media contamination (see Table 6.1) may also have contributed to lower the OLC transition temperature.
- After heating at higher temperatures the Raman spectra display configurations equivalent to those observed for pristine nD heated up to 1773 K (Figure 6.5 (a)) suggesting that the OLC particles receded into sp^2 carbon structures (see Figure 6.4 (f)). Nevertheless, this behavior has not been detected for the heated nD(W) material which indicates that the OLC transformation reversion requires higher temperature ranges than the nD(Cu) and nD(Ni) milled materials or that this behavior is also influenced by the presence of tungsten carbides that are stable above 1573 K [16].

In situ OLC formation

A parallel study investigated the *in situ* OLC transition occurred within a Ni-10nD composite (milled for 4 h at 200 rpm) due to heat exposure of the material up to 1673 K. The carbon phase was chemically extracted from the Ni matrix following the procedure described in Chapter 2 in the Ni-carbon composites section.

Similarly to the heat-exposed nD(Ni) material, the carbon phase in the Ni-10nD composite exhibited approximately spherical OLC particles (Figure 6.6 (a)) together with sp^2 sheets and graphitic particles with hollow centers (Figure 6.6 (b)). Ring diffraction

patterns obtained from the extracted carbon phase (Figure 6.6 (c)), are analogous to the ones obtained for the milled materials (Figure 6.4 (g)).

OLC shows interesting electronic [17,18] and self-lubricating [19,20] properties that may be interestingly combined with the ones presented by metals. The processing route described can be employed to disperse OLC in metallic matrices. Direct milling with metals to form composites is expected to destroy the OLC in a similar way to what has been described for nanotubes [21]. Severe grain growth can be expected for the metal as a result of the heat-treatment required for the nD to OLC transition. Nevertheless subsequent cold deformation processes may be used to refine the matrix. The present results evidence the potential of the method to produce metal-OLC composite materials, and to the author's best knowledge no literature reports can be found on such composites.

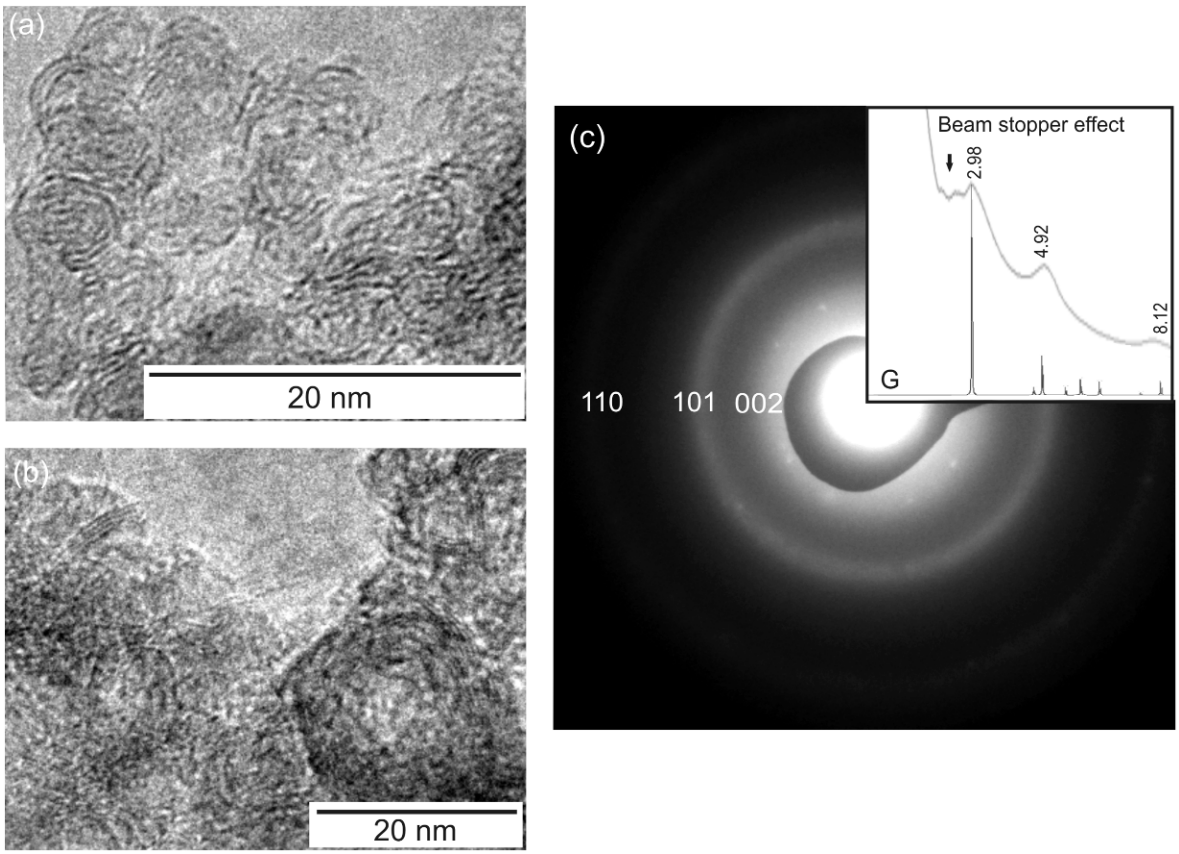

Figure 6.6. (a) and (b) Bright-field TEM images of the extracted Ni-10nD composite milled heated at 1673 K. (c) Ring diffraction pattern with integrated radial profile (graphite simulation included with legend in nm^{-1}).

6.3 Summary

Raman spectra demonstrated that nanodiamond particles remained largely unaffected by ball milling in the presence of metals, as observed for the composites. Heat exposure induced the transformation of nD particles into approximately spherical onion-like carbon particles. However, milling in the presence of metals influenced the subsequent transition and DTA measurements have been used to determine the onset of the OLC transition. Overall milling nD in the presence of metals lowers the OLC transition temperature according to following sequence: nD(Ni)<nD(W)<nD(Cu)<nD. The effect may be justified by the introduction of structural and a possible catalytic effect of the metals. The *in situ* OLC phase transition in the Ni-10nD nanocomposite has been demonstrated and the potential of the method for the development of a metal-OLC composite has been suggested.

6.4 References

[1] V.L. Kuznetsov, Y.V. Butenko, Synthesis, Properties and Applications of Ultrananocrystalline Diamond NATO Science Series 192 (2005) 199–216.

[2] Z. Qiao, J. Li, N. Zhao, C. Shi, P. Nash, Scripta Mater. 54 (2006) 225–229.

[3] S.Y. Lee, N. Mettlach, N. Nguyen, Y.M. Sun, J.M. White, Appl. Surf. Sci. 206 (2003) 102–109.

[4] Y.N. Wu, L.P. Wang, Y.S. Huang, D.M. Wang, Chem. Phys. Lett. 515 (2011) 217–220.

[5] M. Singleton, P. Nash, J. Phase Equilib. 10 (1989) 121–126.

[6] B. Bokhonov, M. Korchagin J. Alloys Compd. 333 (2002) 308–320.

[7] G. Wang, S.J. Campbell, A. Calka, W.A. Kaczmarek, J. Mater. Sci. 32 (1997) 1461–1467.

[8] A.V. Gubarevich, S. Usuba, Y. Kakudate, A. Tanaka, O. Odawara, Diamond Relat. Mater. 14 (2005) 1549–1555.

[9] A.C. Ferrari, J. Robertson, Phil. Trans. R. Soc. Lond. A 362 (2004) 2477–2512.

[10] J. Qian, C. Pantea, J. Huang, T.W. Zerda, Y. Zhao, Carbon 42 (2004) 2691–2697.

[11] M. Yoshikawa, Y. Mori, H. Obata, M. Maegawa, G. Katagiri, H. Ishida, A. Ishitani, Appl. Phys. Lett. 67 (1995) 694–696.

[12] Q. Zou, Y.G. Li, B. Lv, M.Z. Wang, L.H. Zou, Y.C. Zhao, Inorganic. Mater. 46 (2010) 127–131.

[13] J.B. Correia, V. Livramento, N. Shohoji, E. Tresso, K. Yamamoto, T. Taguchi, K. Hanada, E. Ōsawa, Mater. Sci. Forum 587 (2008) 443–447.

[14] Y.P. Ma, F.H. Sun, H.G. Xue, Z.M. Zhang, M. Chen, Diamond Relat. Mater. 16 (2007) 481–485.

[15] E.D. Obraztsova, M. Fujii, S. Hayashi, V.L. Kuznetsov, Y.V. Butenko, A.L. Chuvilin, Carbon 36 (1998) 821–826.

[16] A.S. Kurlov, A.I. Gusev, Doklady Phys. 52 (2007) 656–662.

[17] R. Langlet, Ph. Lambin, A. Mayer, P.P. Kuzhir, S.A. Maksimenko, Nanotech. 19 (2008) 115706-1/8.

[18] D.S. Bychanok, S.I. Moseenkov, V.L. Kuznetsov, P.P. Kuzhir, S.A. Maksimenko, K.G. Batrakov, O.V. Ruhavets, A.V. Gusinski, O. Shenderova, Ph. Lambin, J. Nanoelectron. Optoelectron. 4 (2009) 257–260.

[19] Y. Yao, X. Wang, J. Guo, X. Yang, B. Xu, Mater. Lett. 62 (2008) 2524–2527.

[20] Y. Liu, R.L. Vander Wal, V.N. Khabashesku, Chem. Mater. 19 (2007) 778–786.

[21] Y.B. Li, B.Q. Wei, J. Liang, Q. Yu, D.H. Wu, Carbon 37 (1999) 493–497.

Chapter 7

Chapter 7 – Concluding remarks

The present work focused on the production of metal-carbon composites with nanostructured matrices covering the whole range of carbon affinity: copper that shows extremely reduced affinity towards carbon phases, and nickel and tungsten that are mild and strong carbide formers, respectively, displaying thus intermediate and strong carbon affinities. The processing requirements for each nanocomposite type have been established by systematic variation of the milling parameters. Contamination arising from the milling media has been quantified and shown to be minor for all the composites studied.

High-energy milling was employed in copper materials resulting in apparent bonding at the Cu/carbon interfaces, while for nickel- and tungsten-based materials, mild-energy milling demonstrated to be effective in preventing carbide formation and in originating soundly welded composite powders. The materials produced with 4 h of milling time have been thoroughly investigated for all the composites, as this condition represented the best trade-off between homogeneity maximization, particle dispersion, limited milling media contamination, and carbide minimization.

The effect of milling time and heat treatment temperature on copper and nickel grain size evolutions has been quantitatively assessed. However for tungsten due to a significant presence of tungsten carbides formed during milling (whose X-ray diffraction peaks overlap with pure tungsten ones), the grain size evolution could not be determined.

The as-milled microstructures displayed nanometric grains with mottled contrast and ill-defined boundaries, characteristic of high-energy non-equilibrium states induced by intense deformation. Carbon phases were readily identifiable due to their low atomic number contrast and were homogeneously dispersed in the metallic matrices. The nD particles presented sizes in the 5–20 nm range while graphite particles were typically around 20 nm in size. Higher aspect ratios have been observed for the graphite particles as a resulted of the intense localized deformation imposed on the relatively soft carbon phase. The nanocomposites exhibited an apparent interfacial bonding between matrices and carbon phases.

The chemical dissolution of the metallic matrices allowed for a detailed analysis of the structural changes induced in the carbon phases. As demonstrated by XRD, TEM, and Raman spectroscopy the diamond structure was preserved in nD after milling whereas graphite tended to amorphize. For the W-20nD composite, chemical extraction also revealed the presence of individual W_2C particles, with diameters in the 20–50 nm range, formed during milling. Nevertheless, these particles were present in a minor proportion.

Graphitization of the nD particles occurred *in situ* during annealing of the composites at 973 and 1073 K. This transformation was assisted by structural defects induced by milling and the possible metal doping, as attested by the higher temperatures required for graphitization of pristine nD. The amorphous carbon present in the as-milled Ni-10G composite converted into graphite sheets during annealing at 973 and 1073 K, which indicates that graphitization has also been assisted by the prior milling in the presence of Ni since full graphitization of the amorphous material requires temperatures above 2273 K.

The Cu-10nD composite achieved higher Cu matrix refinement than the Cu-10G one, which has been proposed to result from an additional milling mechanism between the milling media balls and the nD particles. The Ni-based composites showed the opposite behavior, since Ni–10G presented a stronger grain size decrease with milling time than Ni–10nD, which was attributed to the solid solution effect on peak broadening of the former matrix.

Remarkable microhardness enhancement has been achieved for the Cu- and Ni-based nanostructured composites over that of pure metals of comparable grain sizes: ~50 % for Cu–10nD, ~ 20% for Cu–10G and ~70% for Ni-10nD and Ni-10G. Since no significant strengthening could be detected for an as-milled Cu–0.1Cr–10nD composite in relation to Cu-10nD, it has been inferred that interfacial bonding was not significantly improved with Cr dissolution in the matrix. A linear additive model has been used to fit the contribution of several strengthening mechanisms to the experimental hardness values of the Cu- and Ni-based composites. Grain refinement proved to be the major contribution, although second-phase reinforcement, Orowan strengthening and solid solution hardening had important roles on the composites strength.

A rather high thermal stability has been achieved by the Cu-based composites. Indeed after annealing for 1 h at 773 K, which corresponds to a homologous temperature of 0.57 for pure Cu, the Cu–10nD composite remained significantly harder (~ 40 %) than pure nanostructured copper, while the Cu–10G composite presented the hardness level of pure nanostructured Cu. The results obtained suggest that a solute drag effect maybe responsible for this behavior due to the extremely reduced solid solubility of carbon in the copper matrix. The Ni-based composites showed a poor thermal stability after heat treatments at homologous temperatures similar to those applied to Cu-based composites.

Consolidation of Cu-10nD and Cu-0.1Cr-10nD milled materials by hot extrusion and spark plasma sintering (SPS) showed that high densification is attainable with these powder metallurgy routes. However, microstructural heterogeneity has been observed for SPS, where the presence of pure Cu layers at the prior powder boundaries demonstrated that melting at the powder particles surface assisted the sintering process. Both consolidated materials underwent moderate Cu grain grown, and the microhardness values remained at the level of pure nanostructured copper.

Nanodiamond particles remain largely unaffected by ball milling in the presence of Cu, Ni or W (20 at.% proportion). When heated at temperatures ranging from 1573 to 1773 K the milled nD particles transform into spherical onion-like carbon (OLC) particles. The transition temperature follows the nD(Ni) <nD(W)<nD(Cu)<nD(pristine) sequence. The OLC transition is thus assisted by structural defects induced by milling associated with a possible catalytic effect of metallic dopants. The OLC phase transformation has been demonstrated to occur *in situ* during annealing of a Ni-10nD nanocomposite, resulting in a metal-OLC composite.